STUDIES OF CHARGE TRANSFER IN THE $N_2^+ - N_2$ SYSTEM

by

Alphonsa Smith

Dissertation submitted to the Graduate Faculty of the
Virginia Polytechnic Institute and State University
in partial fulfillment of the requirements for the degree of
DOCTOR OF PHILOSOPHY
in
Materials Engineering Science

APPROVED:

George Sanzone
G. Sanzone, Chairman

J. P. Wightman

J. A. Jacobs

John G. Mason
J. G. Mason

J. C. Schug

J. W. Viers
J. W. Viers

May, 1977
Blacksburg, Virginia

ACKNOWLEDGMENTS

The author gratefully acknowledges the assistance of Dr. George Sanzone who served as chairman of my advisory committee and under his guidance this research was performed. A similar note of appreciation must also be extended to other committee members: Drs. James P. Wightman, James A. Jacobs, John C. Schug, John C. Mason and Jimmy W. Viers, for their willingness to take time from their busy schedules to listen and discuss the direction of my research on several occasions.

At NASA Langley the author wishes to express thanks for support of management in the Instrument Research Division, General Research Instrumentation Branch, their patience and consideration over the past 3 years this research has been in progress was of utmost importance for the completion of this work. Special thanks is extended to Mr. Ronald F. Hoyt who was of great assistance in his support of maintaining the vacuum apparatus in operational condition and getting several parts machined as required in the development phases of the system. In addition, notes of gratitude are extended to Mr. Theodore E. Larson who was very helpful in repairing damaged filaments for the ion source, Mr. Lamar Williams for doing the computer programing for the retarding potential curves, Mr. Richard E. Stell for doing porous plug conductance measurements to compare with my own and Mrs. Miriam A. Hall who typed this manuscript.

The discussions of charge-transfer experiments and theoretical techniques with Dr. Grayson H. Rayborn of the University of Southern Mississippi, and Dr. Juliette Ioup of Xavier University of Louisiana were very instructive and helpful during their visits here and are greatly appreciated.

Finally, the author would like to thank his dear wife, Ruby, for her understanding and unusual ability in keeping the family in order during the many hours of my absence, and my children, Cavanaugh, Reginald, and Faith, for their support, encouragement and whose understanding far surpasses their years. It is to them that this thesis is dedicated.

LM/MRT 6/6/77

TABLE OF CONTENTS

LIST OF TABLES

LIST OF FIGURES

I: INTRODUCTION

I.A: APPLICATIONS OF CHARGE EXCHANGE TO AEROSPACE RESEARCH

In recent years, a number of experimental and theoretical investigations have involved the study of reactions of charged and neutral atmospheric species.[1-18] Nevertheless, a detailed understanding of many atmospheric phenomena is not known, due to a lack of precise experimental information concerning the discrete atomic and molecular processes involved.

Many satellite and reentry probe experiments have encountered serious measurement problems with atomic and molecular atmospheric gases.[19-22] One technique for studying and solving such problems is to examine the reactions of energetic molecular beams which impinge on surfaces. In order to do this, techniques must be developed for the generation of neutral atomic and molecular beams with velocities equivalent to those of spaceborne satellites.

A primary concern in aerospace research is the development of methods for accurately calibrating mass spectrometers and ion gages that are flown on spaceborne vehicles. In order to do this, high molecular speeds are required to simulate the high velocity of test instruments through a rarefied atmosphere.

The achievements in the field of upper atmosphere and interplanetary flight have reemphasized the need for a comprehensive analysis of the nature of surface reactions that occur with atmospheric gases. Because of the high chemical reactivity of many atmospheric

species, the possibility for strong interaction with instrument and chamber walls exists. Some molecular and atomic species become permanently adsorbed on surfaces or recombine to form other species. This type of interaction can result in spurious measurements of molecular concentrations.

Perhaps the most immediate interest in gas-gas and gas-surface collisions derives from the growing need for transport-property data. This data is required at temperatures much above those at which viscosity, thermal conductivity, diffusivity, and mobilities can be directly measured. Space flight experiments at Mach numbers above 8 correspond to interaction energies (between the vehicle and atmospheric gases) of more than 1 eV. Satellite and missile velocities correspond to interaction energies in the vicinity of 10 eV for nitrogen molecules. The activation energy for many common chemical reactions lie between 1 and 4 eV. Chemical bond strengths are on the order of 8 eV. Collision processes offer a means for investigating these bond strengths. The adsorption of gases on surfaces plays an important role in modern vacuum technology, where typically the first adsorbed monolayer may be bound by 1 to 4 eV. Additionally, considerable basic scientific interest derives from the use of gas-gas collision experiments for the inference of intermolecular potentials because accurate calibrations for intermolecular potentials are difficult or impossible to obtain. Collision experiments play an important role in providing information on systems not amenable to theoretical investigation and on checking the approximations involved in the calculations that are available.

The research described below was initiated to provide fundamental data on the charge-transfer method of generating high-velocity, low density neutral gas beams, and to report on important parameters which characterize charge-transfer interactions in gases.

I.B: CHOICE OF SYSTEM

The reactions chosen for study are symmetric charge transfer between N_2^+ and N_2. Nitrogen was chosen partly because of its prevalence in atmospheric experiments and can readily be used as a calibration system. The following reactions are considered in this work:

$$N_2^+(X^2\Sigma_g^+,\ v_o') + N_2(X^1\Sigma_g^+,\ v_o'') \longrightarrow$$

$$N_2^+(X^2\Sigma_g^+,\ v') + N_2(X^1\Sigma_g^+,\ v'')$$

$$N_2^+(A^2\pi_u,\ v_o') + N_2(X^1\Sigma_g^+,\ v_o'') \longrightarrow$$

$$N_2^+(A^2\pi_u,\ v') + N_2(X^1\Sigma_g^+,\ v'')$$

$$N_2^+(B^2\Sigma_u^+,\ v_o') + N_2(X^1\Sigma_g^+,\ v_o'') \longrightarrow$$

$$N_2^+(B^2\Sigma_u^+,\ v') + N_2(X^1\Sigma_g^+,\ v'')$$

The studies were carried out for relative translational energies in the range from 9 to 441 eV. Since the target gas possesses only thermal energies, the relative energy is effectively that of the ion beam. Exact control of the primary-ion states is not possible with the normal electron impact ionization ion source. However, some control in specific state population is possible by selecting the

electron ionization energy to correspond to the threshold of a specific electronic state. Three particular states of N_2^+ were of interest; $X^2\Sigma_g^+$, $A^2\pi_u$, and $B^2\Sigma_u^+$, have formation thresholds which occur at electron energies of 15.63, 17.0, and 18.94 eV, respectively.[23]

A search of the literature shows some experimental and theoretical data available on charge exchange cross section for nitrogen ions in their parent gas.[1-18] Comparison can then be made to give a figure of merit to the accuracy of our results.

Since the experimental apparatus had to be assembled, considerable thought was given to the charge-exchange experiment so that errors could be avoided. This requires that the gases chosen for study be noncorrosive, chemically stable, and nonreactive to background gases and system materials. The ions in these experiments are produced in an electron-bombardment ion source. The filament in this source is operated at temperatures in excess of 2000 K; this makes chemical stability and inertness highly desired properties of the gases to be studied. In our system, the ionization chamber is held at about 525 K to assure source cleanliness. Again, at these temperatures, highly reactive gases can create many problems which could make accurate, reliable measurements almost impossible. Nitrogen is known to be well-behaved in this type of environment.

I.C: IMPORTANT EXPERIMENTAL PARAMETERS

Most measurements in charge exchange experiments at low energies have been made on beams of positive ions passing through a neutral, thermal target gas. Charge-transfer cross sections are obtained from measured currents of slow ions formed in the passage of a fast ion beam through a target gas of known density. In this research, charge transfer cross sections are deduced from measurements of three separate currents: I_{CTC}, the current to the Charge-Transfer-Cell; I_{CTCS}, the current to the Charge-Transfer-Cell-Screen; I_{BF2}, the current to Beam-Flag Two. See Figure 1. From these current measurements and the known reaction pathlength, cell pressure, and cell temperature, charge-transfer cross sections are readily obtained.

The object of this work was, in part, to assess our technique in studies of the ion-energy dependence of observed cross sections in the range from 9 to 441 eV. Additional efforts were directed to determine the effect of the internal state of the primary ion beam on the charge-transfer process. Although exact state selection in the primary ion beam was not possible with our ion source, some control of specific-state population was possible by the selection of ionization electron energies. Data was collected for four different pressures to check for any apparent dependence of charge-transfer cross sections on charge-transfer cell pressure.

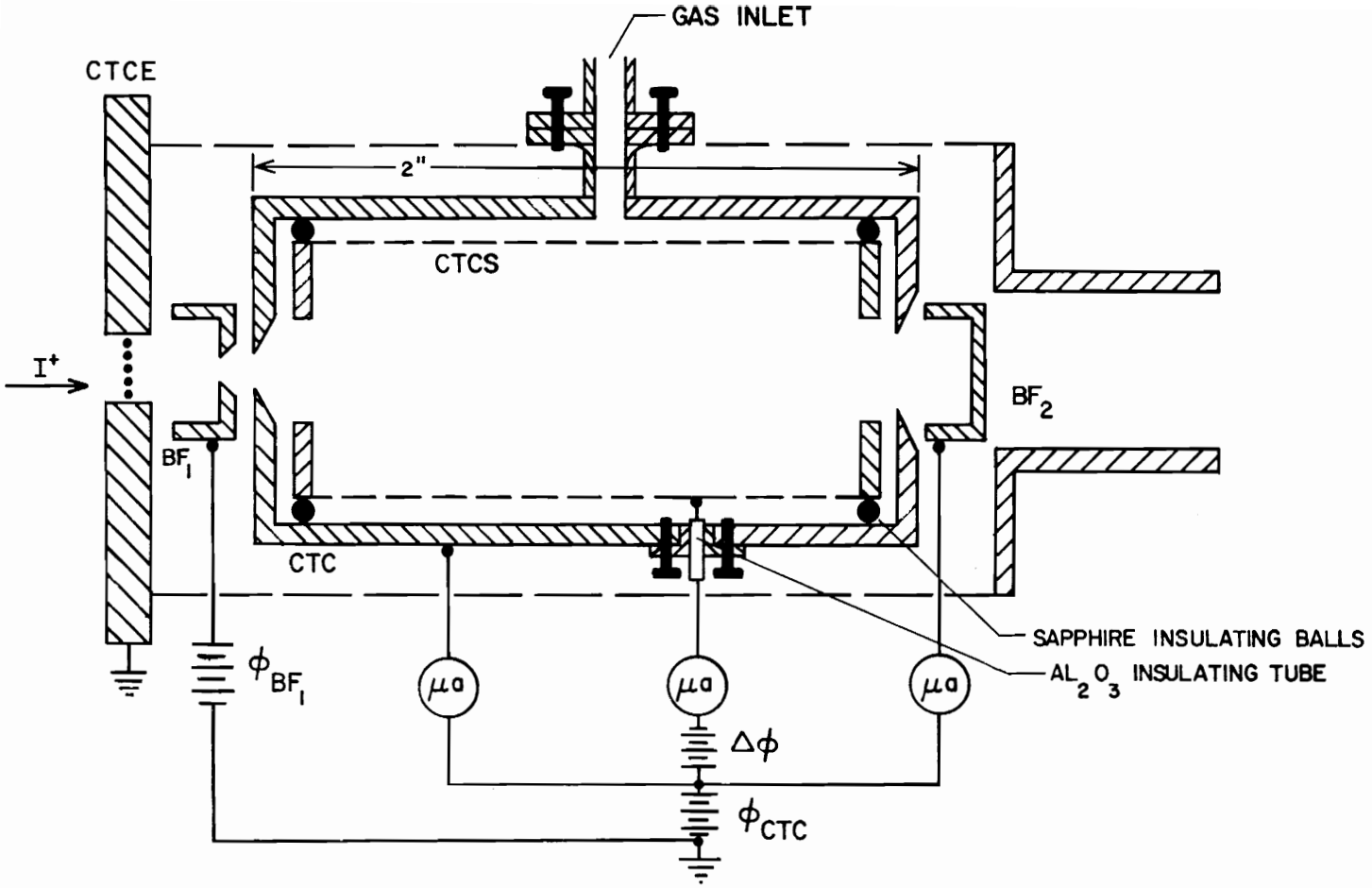

Figure 1.- The Ion Detection and Collection System.

II: HISTORICAL REVIEW

II.A: LANGEVIN, HASSÉ, AND COOK ION-MOLECULE STUDIES

Studies in inelastic collisions at low energies (<500 eV) between charged particles and neutral atoms and molecules began in the early 1900's. The first theoretical work of importance was reported by Langevin[24,25] for ionic mobility data. Langevin considered the clustering of molecules about gaseous ions and orbiting collisions between ions and molecules. He considered the ions and molecules to be solid elastic spheres, the ions differing from the molecule only by possession of an electric charge. Only repulsive forces acting at instant of impact were taken into account. The ion density was taken to be low in order that ion-ion interaction could be ignored. Langevin theory applied to the "low-field" region[24] and took into account the elastic scattering of ions by the inverse fifth power attractive forces between ions and molecules as well as by rigid sphere repulsion. An ion attracts neutral molecules by polarization forces in the case of nonpolar gases and, in addition, by direct attraction of the permanent dipoles if the gas is polar. The interaction potential[24] for nonpolar molecules is given as

$$\Phi(r) = - \frac{\alpha e^2}{2r^4} \qquad (1)$$

where α = gas polarizability

e = ionic charge

r = distance between center of ion and molecule

This potential term describes the interaction between an ion and the dipole which it induces in the electronic cloud of the molecule. The equation is valid when r is large compared with the charge separation of the dipole. The work of Langevin was unnoticed for several years until Hassé [26] published a paper referring to it in 1926. Other investigators became aware of the fact that the attraction of ions by molecules must be considered. Two distinctly different theories [27] involving the concept of polarization attraction were advanced during the period from 1905 to 1926. One proposal was that neutral molecules are attracted to and permanently bound by the ion because of its charge and that the increased size and mass of the ion which result from this attachment are responsible for the low observed value of mobility. Opposed to the cluster-ion theory was the small ion theory, in which the assumption was made that the size of the ion is relatively unimportant since the ions are retarded in their motion, principally by momentum transfer which is due to the action of the attractive forces. In 1926 Hassé [26] discovered Langevin's paper and pointed out that the small-ion equations were approximate forms of a special case of the 1905 Langevin equation. Some years later, in 1931, Hassé and Cook [28] used the Chapman-Enskog theory for a low field calculation in which the ion molecule reaction was described in terms of the inverse fourth power attractive polarization

potential and an inverse eighth power repulsive potential. The Hassé-Cook calculation did not appear to provide any great improvement over the Langevin theory. In many instances the mobility measurements are dominated by the polarization forces to the extent that Langevin polarization limit is essentially correct.

The Langevin[29] cross section for orbiting collisions has been shown to be

$$\sigma_L(v_o) = \frac{2\pi}{v_o}\left(\frac{e^2\alpha}{\mu_r}\right)^{1/2} \qquad (2)$$

where v_o = relative velocity of approach of the two interacting particles

μ_r = reduced mass of interacting particles

e = ionic charge

α = gas polarizability

Although Langevin's model of the polarization potential for ion-molecule reactions provided the first basis for experimental studies of cross sections, difficulties arise if the assumptions in this model are taken to be literally true.

II.B: EMPIRICAL EXPRESSIONS FOR INTERMOLECULAR POTENTIALS

The interaction potential[30] between an ion and molecule is usually expressed in modern work as

$$\Phi(r) = A\varepsilon^{-\beta r} + \sum_{n=4} B_n r^{-n} \qquad (3)$$

where A, B_n, and β are constants. The exponential term represents the short range repulsion due to electron cloud interpenetration and other quantum mechanical effects; the series term represents the long-range interaction. One almost never knows the true interaction potential and instead must be satisfied with mathematical models that one hopes mimic the true potential in a reasonable way. Such models are ordinarily concocted to reproduce various known asymptotic forms of the true potential and behave in a qualitatively correct way in intermediate regions. Interaction potentials are calculable in principle with Schrodinger equations and fundamental constants. These calculations soon become bogged down in computational difficulties and approximations are almost always necessary. It is usually convenient to divide intermolecular forces into long-range, short-range, and intermediate-range forces. The most important long-range component of the interaction between an ion and neutral molecule is the polarization or induction potential. There are terms in the polarization energy however, other than the spherically symmetric r^{-4}. If the molecule is not spherically symmetric there will be an angle dependent

term in the potential due to the anisotropy of the molecular polarizability. The ions induce not only a dipole moment in the molecule but also quadrupole and higher moments which interact with the ionic charge. The complete expression for the polarization energy is thus an infinite series containing angle-dependent terms. For a molecule with spherical symmetry the first few terms are [31]

$$\Phi(r) = - \frac{e^2 \bar{\alpha}}{2r^4} \left(1 + K(3 \cos \theta - 1)\right) - \frac{e^2 \alpha_q}{2r^6} + \cdots \qquad (4)$$

where $\bar{\alpha}$ = average dipole polarizability

K = anisotropy

α_q = quadrupole polarizability

The r^{-4} term results from the induced dipole and r^{-6} term from the induced quadrupole. The average dipole polarizability $\bar{\alpha}$ and anisotropy K are defined [32] in terms of the dipole polarizabilities parallel and perpendicular to the molecular axis as

$$\bar{\alpha} = 1/3 \, (\alpha_{\parallel} + 2\alpha_{\perp}) \qquad (5)$$

$$K = \frac{\alpha_{\parallel} - \alpha_{\perp}}{\alpha_{\parallel} + 2\alpha_{\perp}} \qquad (6)$$

The molecular axis makes an angle θ with the line drawn from the charge to the center of the molecule. Quantum mechanics has been used to calculate $\bar{\alpha}$, K, and α_q; such calculations are often the best source for α_q, but the best values of $\bar{\alpha}$, K usually come from

experiments or from a judicious combination of theory and experiment. Summaries of numerical values of $\bar{\alpha}$, K, and α_q for some common gases of interest has been published.[33,34] In Table I, several physical constants are tabulated for a few of the common gases.

TABLE I. PHYSICAL CONSTANTS FOR INTERMOLECULAR POTENTIALS

	Average Dipole Polarizability $\bar{\alpha}$ $(10^{-8}$ cm$)^3$	Anisotropy K	Quadrupole Polarizability α_q $(10^{-8}$ cm$)^5$	Parallel Polarizability $\alpha_{\|\|}$ $(10^{-8}$ cm$)^3$	Perpendicular Polarizability $\alpha_{\perp}$ $(10^{-8}$ cm$)^3$
N_2	1.76 [33] a 2.46 [32] b	0.176 [33] 0.472 [32]	-	2.38 [33] 4.67 [32]	1.45 [33] 1.27 [32]
CO	1.95 [33] a 2.44 [32] b	0.167 [33] 0.373 [32]	-	2.60 [33] 4.32 [32]	1.625 [33] 1.55 [32]
O_2	1.60 [33] a -	0.238 [33] 0.229 [36] b	-	2.35 [33] -	1.21 [33] -
CO_2	2.65 [33] a 2.59 [35] a	0.264 [33] -	-	4.01-4.1 [33] -	1.97-1.93 [33] -

a - experimental

b - theoretical

II.C: CAPTURE COLLISIONS BETWEEN IONS AND POLAR MOLECULES

The early development of Langevin concerning mobility of ions in gases and charge transfer appears to have been continued by Tyndall,[37] Massey[38] and in later years by Hasted.[39]

An integrated cross section for collision of an ion with a polarizable molecule in an ion source of a mass spectrometer has been described by Gioumousis and Stevenson[40] in terms of point particles. Their development indicated that the experimentally observed cross section $\bar{\sigma}_E$ is inversely proportional to the square root of the repeller field strength. There appears to be a theoretical[41] basis for the belief that many of the simple ion-molecule reactions should have an experimental cross section $\bar{\sigma}_E$ that varies as $(E_r)^{-1/2}$ where E_r is the repeller field strength.

The microscopic cross section for an ion-molecule reaction is usually written as

$$\sigma(v_o) = P\ \sigma_L(v_o) \qquad (7)$$

where $\sigma_L(v_o)$ is the classical Langevin cross section for orbiting collision, between primary ions and molecules approaching one another with relative velocity v_o, and P is the probability that the reaction will result if orbiting occurs. The rate of a reaction (R_x) at a point is expressed in terms of the velocity distributions f_1 and f_2 of the two reactants and of the microscopic cross section $\sigma(v_o)$ as

$$R_x = \int_o^\infty \int_o^\infty f_1(v_1)\ f_2(v_2)\ \sigma(v_o)\ v_o\ d^3v_1 d^3v_2 \qquad (8)$$

Gioumousis and Stevenson[40] carried over Langevin's study of ion trajectories to calculated reaction cross sections. The interaction potential assumed was equation (1) but a critical reaction radius r_c was proposed for ion-molecule pairs. In reference 40 it is shown that ions which start toward the molecule at an impact parameter less than a critical impact parameter b_c will be captured. These captured ions will spiral inward until the ion and molecule react inside a critical radius r_c. The critical impact parameter for the Langevin case is

$$b_c = \left(\frac{4e^2\alpha}{\mu_r\ v_o^2}\right)^{1/4} \qquad (9)$$

and is dependent on the relative velocity v_o. In the case of orbits where the impact parameter b is less than b_c, this leads to ion trajectories that pass through the origin while orbits for which b is greater than b_c come no closer than $2^{-1/2}b_c$. Langevin proposed that so long as r_c is between zero and $2^{-1/2}b_c$, all collisions for which $b < b_c$ lead to reaction and the reaction cross section is given by equation (2). The Langevin theory has been proven inadequate for predicting the captive cross section for collisions between an ion and a molecule with a permanent dipole moment. An additional ion-molecule term accounting for the permanent dipole interaction[42,43]

$$\Phi_p(r, \theta) = - \frac{\mu e \cos \theta}{r^2} \qquad (10)$$

where μ is the dipole moment and θ is the angle between the negative side of the dipole and the r vector.

Threard and Hamill [42] included the Φ_p term with cos θ = 1, for simplicity, and derived the following maximum ion-permanent dipole cross section contribution

$$\sigma_D = \frac{\pi \mu e}{E} \qquad (11)$$

where E is the relative reaction energy at infinite separation, and μ is the permanent dipole moment. Threard and Hamill explained the large cross section observed for certain ion-polar molecule collisions in terms of total cross section σ_T(= σ_D + σ_L) which is taken to be the maximum upper limit cross section for ion-polar molecule collision independent of molecular geometry. This is precisely the expression used in references 42 and 43 to fit experimental ion-molecule data. It says that regardless of the ion trajectory the dipole can always orient favorably for capture. This is a type of adiabatic approximation where it is assumed that the Hamiltonian changes slowly. This rate of change must be sufficiently slow so that the dynamical system can act to minimize the energy. These experimental results were extended by Moran and Hamill. [43] Their experiments demonstrated that the ion-dipole term does make a large contribution to the observed

cross section. The choice of equation (11) for the ion dipole term presumes the dipole can always adjust to a maximum orientation in the ion field. This, however, is not generally the case. The ion transit time and rotational period would be expected to be important considerations.

Su and Bowers[44,45] introduced the average-dipole-orientation (ADO) theory and demonstrated the effects of permanent dipole moment on the reaction cross sections. The theory is formulated in terms of an r-dependent average orientation angle between the dipole and the line of centers of collision. This technique allows quantitative determination of the capture cross section as a function of ion polar molecule relative velocity. It was emphasized in references 44 and 45 that the theory presented was intended to be primarily useful in calculating phenomenological capture rate constants and cross sections. The model was not intended to describe phenomena that occur in the impact parameter range of 8-15 x 10^{-8} cm. Also this treatment does not apply to microscopic phenomena.

III: THEORETICAL AND MEASUREMENT CONCEPTS

III.A: THE CHARGE TRANSFER COLLISION CROSS SECTION

The probability of any collision process may be conveniently expressed in terms of a cross section (σ) for the process. For the charge-transfer interaction, if we consider one collision, we can assign an area, σ, to each target particle such that, if the center of a bombarding particle strikes inside σ, there is exchange and a product ion is produced. When the center of the bombarding particle misses σ, no interaction occurs. The quantity σ is called a cross section and gives a measure of the reaction probability per target particle. This cross section need not be the same as the geometric cross section of the target particle.

We can also describe the charge-transfer probability as $-\Delta I/I(o)$, where $I(o)$ represents the incident beam current (particles per unit time) and $-\Delta I$ represents the depletion of this incident beam by charge transfer in a target thickness Δx. The ratio $-\Delta I/I(o)$ depends upon target-gas density, whereas σ is associated with an individual target particle. The probability that any one bombarding particle has a "hit" is equal to $-\Delta I/I(o)$ but is also equal to the total cross section of all target particles lying within the incident beam area A, as projected in the beam direction, divided by the beam area A. If there are n target particles per unit volume in the target region, then $nA\Delta x$ particles are within reach of any bombarding

particle in the incident beam. Each target particle has an associated cross section σ; therefore:

$$\frac{-\Delta I}{I(o)} = \frac{nA\Delta x\sigma}{A} = n\sigma\Delta x$$

Making use of the ideal gas law we then obtain

$$\sigma = - \frac{kT}{p\Delta x} \cdot \frac{\Delta I}{I(o)} \tag{12}$$

Equation (12) assumes that the target is sufficiently thin that none of the target particles are shadowed by others, and that no appreciable depletion of the beam takes place. Equation (12) shows how cross sections can be determined in terms of measurable quantities, and is sufficiently accurate for many experiments. If the target particles are too dense for this assumption to be valid, equation (12) must be modified. If we consider the exchange in a differential length dx, then $\Delta I \rightarrow dI$ and we then have

$$\sigma = - \frac{kT}{pdx} \frac{dI}{I} \tag{13}$$

Rearrangement and integration then yields:

$$\ell n \frac{I(x)}{I(o)} = - \frac{\sigma p}{kT} \int_{o}^{\Delta x} dx$$

If x is the total length of the charge transfer cell then

$$\sigma = - \frac{kT}{px} \ln\left(\frac{I(x)}{I(o)}\right) \tag{14}$$

In equation (14), I(o) is the beam current at the entrance to the charge transfer cell. The quantity $I = I(o) - I(x)$ is the depletion of the incident beam current and is just that part which has undergone charge transfer. Substituting $I = I(o) - I(x)$ into equation (14) and using the MacLaurin expansion for the logarithm we obtain

$$\sigma = \frac{kT}{px} \cdot \frac{I}{I(o)} \left[1 + \frac{1}{2} \frac{I}{I(o)} + \frac{1}{3} \frac{I}{I(o)}^{2} + \cdots\right] \tag{15}$$

It can be seen that for small values of I/I(o), equation (15) gives the same results as equation (12). Both equations (12) and (14) give the prescription for measuring cross sections. The quantities which must be measured are the length x of the target region, the pressure p, and absolute temperature T within that region, the incident beam current I(o), and the transmitted current I(x).

III.B: EXPERIMENTAL LAW AND MEASUREMENT TECHNIQUES

A beam of ions traversing a gaseous target will be attenuated by collisional scattering processes. Some collisions will cause a change in the internal energy of either or both of the collision partners; such collisions are said to be "inelastic." A collision cross section is a microscopic property of the collision system which is related to the probability that a particular collision event will occur under specified conditions. Values of cross sections depend on the nature and state of the reacting particles, their relative velocity, and the impact parameter. Measurements are meaningful only under the experimental conditions for which the cross section is operationally defined. Accuracy of a cross section measurement is directly related to the accuracy or level of confidence with which the experimental parameters are defined.

Charge-transfer between an ion and a neutral species involves a class of inelastic collision whose probability can predominate over other reactions. If either of the collision partners are molecular, these other processes can include rotational and vibrational excitation and dissociation.

The transfer of charge between an ion and neutral atom results in the formation of very slow ions (thermal energy) and neutrals having an energy practically equal to the initial energy of the projectile ion. Ions that have traveled a single charge transfer free path become

neutrals but retain their velocity. The atoms that give up electrons and become ions continue to move at essentially thermal velocities.

Charge-transfer reactions are often classified as being either symmetric or asymmetric. Symmetric charge transfer is the process of charge transfer between an ion and its neutral parent. Resonant charge transfer is charge transfer in which the energy defect (see Appendix A1) is zero, that is, there is no change in the internal energy of the target-projectile system. In discussions of charge transfer, the term "accidental resonance" is sometimes used; this term refers to cases in which the energy defect is small or zero, not because of a symmetry, but by chance. The structure of resonant and nonresonant charge transfer cross section curves (cross section versus ion impact energy) are usually different. Most of the structural difference has often been attributed to symmetry,[46] but this idea is not universally accepted.[46] For endothermic systems (positive energy defect) structural curves show an energy threshold. Exothermic charge transfer (negative energy defect) processes show no such threshold. However, the cross section curves for both exothermic and endothermic processes frequently have similar appearances; they rise from an apparent onset to reach a maximum and then slowly decrease with increasing ion impact energy. The theoretical treatment of charge transfer reaction is sometimes confused because of poor correlations between reported results. Some researchers make no mention of sign in discussion of energy defect. Theoretical treatments[47-49] make no attempt to note the sign of the energy defect. Experimental results

have shown that cross sections for symmetric resonant transfer usually are larger than cross sections for nonresonant transfer. Because of this, ion beam neutralization by charge transfer usually are done in the parent gas to obtain a neutral atomic and molecular beam of high translational energy. The variation of symmetric resonant charge transfer cross section ($\sigma_{10/01}$) with ion impact energy (E) has been approximately represented by an expression of the following form [50-54]

$$\sigma^{1/2} = a - b \ln E \qquad (16)$$

where a and b are constants. No such functional relation for nonresonant charge transfer cross section has been universally accepted.

Experiments have been done to define the operational definition of a collision cross section in terms of such macroscopic observables as beam flux, beam current, and target density. This definition then necessarily relates observed parameters to the experimental apparatus used for the measurement. Two basic geometrical arrangements have been used. The most frequently used method involves a projectile-beam incident on a static gas target. A second technique involves the intersection or crossing of a projectile beam with a target beam. The first technique is sometimes referred to as the condenser method; it was developed many years ago by Goldman [55] and Rostagni, [56] and has been employed successfully. [57-63] It is the first technique which is used in this research.

If I(o) represents the ion current for a beam composed of a single type of ion which is incident on a charge-transfer cell of length x, then if the charge transfer cell is filled with a target gas to make a number density n, the transmitted current will decrease.

$$dI = - I\, n\, \sigma\, dx \tag{17}$$

Integration yields a Beer-Lambert expression:[64,65]

$$I(x) = I(o)\, \exp(-n\sigma x) \tag{18}$$

where σ represents the total macroscopic scattering cross section for all processes by which an ion can be lost. I(x) represents the current for the unscattered beam component as measured at the exit of the charge transfer cell. Under so-called "thin target" conditions, where $n\sigma x << 1$, the following approximation is often made:[66]

$$\exp(-n\sigma x) = 1 - n\sigma x$$

With this approximation,

$$\Delta I(x) \equiv I(o) - I(x)$$

$$\Delta I(x) = I(o) n\sigma x \tag{19}$$

At the pressures used in these studies, the target gas is ideal, so that

$$p = nkT \tag{20}$$

where p, n, and T are the pressure, number density, and absolute temperature of the gas in the charge-transfer cell; k is the Boltzmann constant. With the thin-target approximation:

$$\sigma = \frac{kT}{px} \cdot \frac{\Delta I(x)}{I(o)} \tag{21}$$

Notice that equation (21) predicts that the cross section σ can be obtained from the slope of a graph of $\Delta I(x)$ versus charge-transfer cell pressure. But variation of pressure within a given experimental run is too cumbersome because it requires time for the system to equilibrate after each pressure change. Pressure variation can also present problems if it becomes necessary to increase to a range where the vacuum pumping system cannot maintain a low background pressure outside of the charge transfer cell. It is more efficient to change other parameters such as electrical potentials and to monitor changes in currents associated with the charge-transfer process. This latter approach was taken in this research.

Care must be exercised in applying equation (21). It is not always clear that the thin-target approximation is valid. For this reason, the thin-target condition was not assumed in this research. From equations (18) and (20), we obtain:

$$\sigma = - \frac{kT}{px} \ln \frac{I(x)}{I(o)} \tag{22}$$

If we focus on the charge-transfer contribution to the scattering, then we should consider only that part of the transmitted beam which did not

charge-transfer:

$$I(x) = I(o) - I_{CT} \tag{23}$$

The quantity I_{CT} represents that portion of the incident current related to the charge transfer process; it is a current associated with the slow ions formed in charge-transfer collisions. From equations (22) and (23), we find

$$\sigma = - \frac{kT}{px} \ln\left(1 - \frac{I_{CT}}{I(o)}\right) \tag{24}$$

To apply this result to the measurement of charge-transfer cross sections, a detection and collection scheme had to be developed which separates the slow ions produced by charge transfer from the more energetic incident and otherwise scattered ions. The detection and collection scheme used in this research is shown in Figure 1.

Charge-transferred ions (I_{CT}) are collected on the charge-transfer-cell screen (CTCS) by maintaining a potential difference $-\Delta\phi$ between CTCS and CTC (charge-transfer-cell). A small fraction of the primary beam will also be collected on CTCS because the screen wire is not completely transparent to those few primary ions scattered through a large enough angle along the beam path. The screen wire has a 92 percent transparency rating for particles approaching normal to its surface. For particles approaching from something less than normal, the transparency rating decreases. It is suspected that most of the primary ions collected on CTCS are collected at the back

ring used to support the screen wire. Under ideal focusing conditions, all of the primary beam that does not undergo charge transfer would pass through CTC and be collected at beam flag two, BF2. Due to imperfection in focusing and apparatus alignment, this condition was never obtained. At $\Delta\phi$ equal to zero, one could never expect the current ratio $I_{CTCS}/I(o)$ to be zero because the slow ions will now be collected on either CTCS or CTC, which have essentially the same electrical potential. The slow ions will find themselves in a field free region inside or outside the CTCS and therefore some of these ions will be collected on CTC. This factor alone will always account for the current ratio $I_{CTCS}/I(o)$ not being zero when $\Delta\phi$ is zero. When $\Delta\phi$ is not zero, the slow ions may oscillate through the screen wire but will respond to the local electric field outside the charge-transfer-cell screen. We now see that the current ratio $I_{CTCS}/I(o)$ may not be zero when $\Delta\phi$ is zero because of the following factors: Imperfections in focusing, apparatus misalignment, and slow-ion collection on CTC.

A correction is seen to be necessary to account for those ions collected on CTCS which are not produced by charge exchange. If this correction is not made, cross sections determined by equation (24) will be larger than true values.

III.C: EFFECT OF ION BEAM EXCITATION ON CHARGE TRANSFER

Many measurements of charge transfer cross sections involving molecular ions have been described in the literature.[67-69] In these measurements, it is expected that some of the ions will be in long-lived excited states. In general it can be stated that charge transfer cross sections may be different for the excited state ions. The effect of ion beam excitation not only can influence the reaction channels but could account for the entire cross section in some cases.[69] Anme and Utterback measured charge transfer cross sections for the $N_2^+ - N_2$ system, as a function of ion energy and ion source electron energy.[69] The resonant $N_2^+ - N_2$ system cross section varied as a function of ion energy in the manner generally reported by other investigators. However, the cross section was shown to decrease 15 percent in going from 17 to 23 volts electron ionization energy. This was attributed to metastable ions in the beam, which were believed to transfer in a less efficient way. The usual practice has been to ignore beam excitation effects. Until recently,[67-69] little importance was attached to the mode of formation of ions; it was considered sufficient in most studies to simply use a mass analyzed beam of the correct chemical species. The inadequacy of ion-beam-preparation procedure has been demonstrated in a number of experiments,[67-69] where the collision properties of ions of a given chemical type have been observed to depend upon the nature and mode of operation of the ion source. In the case of electron bombardment ion

sources, for example, the collision properties of the resulting ions have been shown in many cases to be extremely sensitive to the energy of the ionizing electron.[68-71] It is obvious that a full description of an ion-beam experiment requires that not only the type of ion, but also its state, be known for the reactant and products. Unfortunately, few experiments have been designed to identify the states of the parent ion and even fewer to identify the states of the products.

It has been reported[72] that the technique of photoelectron spectroscopy offers an approach to determining fractional populations of the various ionic states resulting from photoionization; there is hope for an extension of this work to the study of the composition of ion beams formed by electron bombardment. For the present, however, there is extreme difficulty in inferring the final distribution of ions in a beam from a knowledge of the initial distribution formed in an electron impact ionization process. The problem remains therefore to study and evaluate directly the ion beam itself by such methods as, for example, controlling the electron ionization energy of the ion source. Such methods do not, in general, yield a complete description of the internal-energy state distribution in the beam. In the case of molecular nitrogen ion beams, these methods could permit studies of N_2^+ in its ground electronic state ($X^2\Sigma_g^+$) and its first two excited static ($A^2\pi_u$ and $B^2\Sigma_u^+$). Since these states are separated approximately by 1.1 and 3.1 electron volts,[73] respectively, with careful calibration of the electron ionization energy one could produce ion beams in the

ground electronic state, in a mixture of ground state and first excited state, and in a mixture of ground state and the first two excited states. (See Figure 2.) However, no such separation or control can be placed on the population of the vibrational and rotational states due to electron bombardment.

Turner, et al.[67] were the first to report on a technique of using attenuation curves to investigate the abundance of excited states in ion beams. This principle is based on the linear attenuation of an ion beam in collision when one particular state is present. When two or more states are present, curvature of the attenuation should be detected. In principle this technique shows promise but in practice the interpretation and evaluation of attenuation curves is much more complicated, because many experimental factors (such as ion source operation, ion beam stability, pressure fluctuations, and time of flight of the ion beam versus excited stated lifetimes) influence the beam composition. One can also see that where more than two states are involved the problem is compounded.

In the measurement of total charge transfer cross sections, consideration should be given to the lifetimes for the existence of the various excited states of N_2^+. The length of the charge transfer cell is approximately 5 centimeters. For an ion with an incident energy of 9 electron volts, or incident speed of 7.87×10^5 cm/sec, the time spent in the CTC region is on the order of 6.45 μsec, an ion of incident energy of 441 electron volts has an incident speed of 5.51×10^6 cm/sec and a residence time of 0.922 μsec inside the CTC.

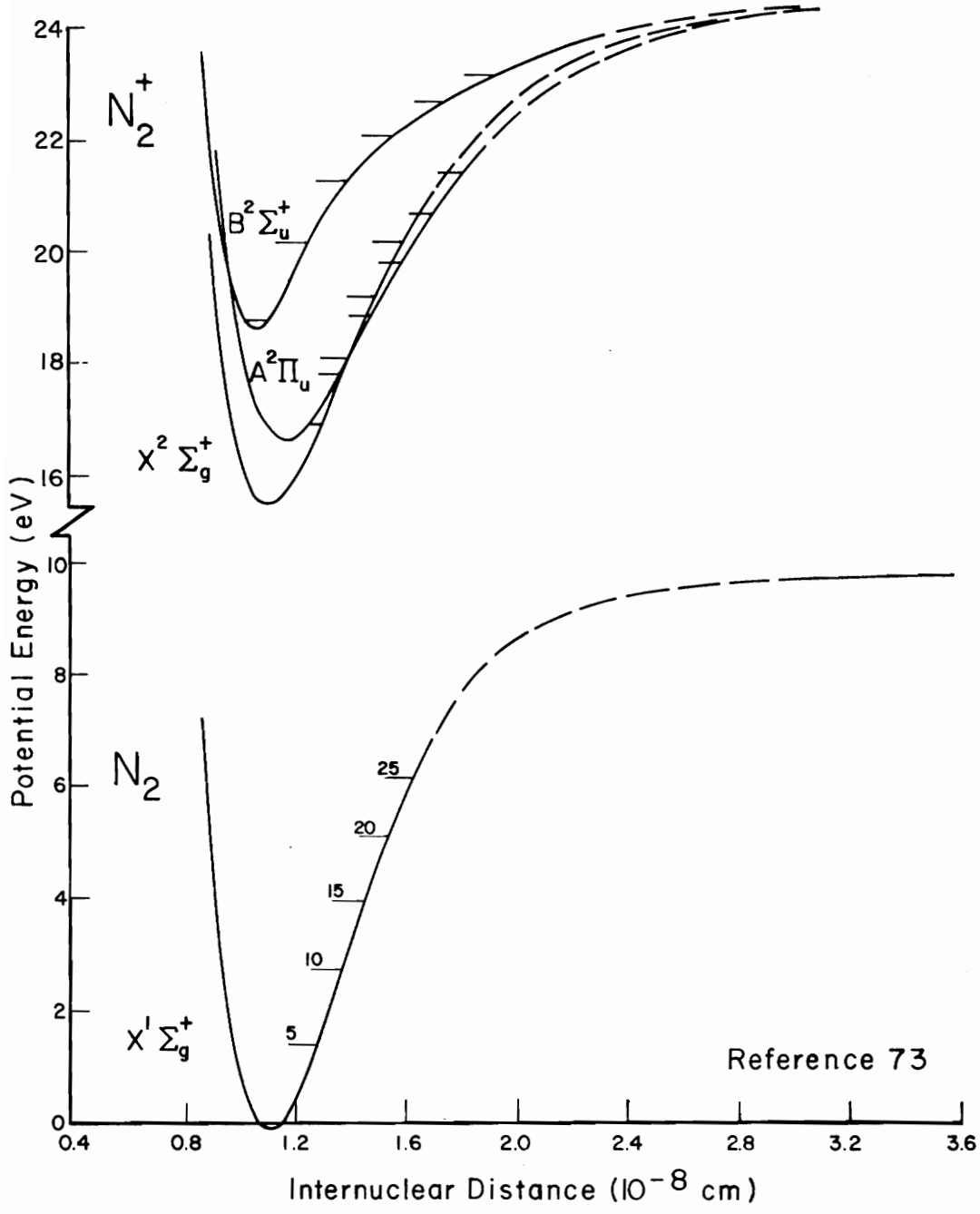

Figure 2.- Potential Energy Curves for N_2^+ and N_2.

The electron energies used to produce the N_2^+ ions were selected to be between 11.6 and 32.1 electron volts in this experiment. Only the ground state $N_2^+(X^2\Sigma_g^+)$ and the first two excited states $N_2^+(A^2\pi_u)$ and $N_2^+(B^2\Sigma_u^+)$ need to be considered, because the lifetimes of any other states are too short. The lifetimes[74-79] of the B→X radiative transitions have been shown to be on the order of 40-70 nanoseconds, so that all the $N_2^+(B^2\Sigma_u^+)$ ions formed in the electron impact ionization, undergo transitions to the ground state $N_2^+(X^2\Sigma_g^+)$ long before they arrive at the CTC region. The lifetimes[80-85] of the A→X transitions, τ, are given in Table II for the first few vibrational levels. For typical collision experiments, the ion transit times are on the order of 10 to 12 microseconds. For these transit times, some undecayed $N_2^+(A^2\pi_u)$ excited states will be present in the ion beam. Flannery, et al.[49] considered the presence of excited states in their experiments where the ions were contained for 9.6-14.2 microseconds in their time-of-flight apparatus. This ion transit time, i.e., the time required to travel from the ion source to the center of reaction region is about the same magnitude (8-9 microseconds) as expected in the apparatus used in this research. Electronic, vibrational, and rotational transitions are important only when such transitions can take place during the time of the collision. The collision times for molecular speeds of $5 \times 10^6 < V < 0.8 \times 10^6$ cm/sec, corresponds to a collision time (i.e., the lifetime of the ion-molecule complex) in the range 4×10^{-14} sec $> \tau_{coll} > 3 \times 10^{-15}$ sec. Therefore, the collision times are much less than the time of rotation, and the collision is

TABLE II. MEASURED LIFETIMES OF SOME $A^2\pi_u \rightarrow X^2\Sigma_g^+$ RADIATIVE TRANSITIONS FOR THE N_2^+ ION

υ'	τ(μsec)[80]	τ(μsec)[81]	τ(μsec)[82]	τ(μsec)[83]	τ(μsec)[84]	τ(μsec)[85]
0	15.5	-	7.6	8.5	-	-
1	13.7	-	7.0	6.8	13.9	-
2	12.2	-	6.5	6.3	11.9	9.4
3	11.0	12.2	6.1	-	10.7	8.0
4	9.9	11.4	5.8	-	9.7	7.8
5	9.1	12.2	5.5	-	9.1	-
6	8.4	-	5.3	-	8.4	-
7	-	-	-	-	7.8	-
8	-	-	-	-	7.3	-

finished before the ion-molecule complex can rotate. However the collision time is the same order of magnitude as the vibrational time.

It has been shown [49] that certain low vibrational levels are most strongly populated by the electron-implant-ionization process. A fraction of the $A^2\pi_u$ state ions entering the analyzer tube will transit the collision region in the same state. The presence of this fraction of undecayed $A^2\pi_u$ state ion can have an effect on observed charge-transfer cross sections. Flannery, et.al. [49] have shown that the population of the $X^2\Sigma_g^+$ and $A^2\pi_u$ ionic states are in the ratio of approximately 90:10 for electron impact energy of 20 electron volts. Ions formed at this electron energy have two possible reaction paths available in the charge transfer process: A channel where secondary ions are formed in the $X^2\Sigma_g^+$ state and a channel where secondary ions are formed in the $A^2\pi_u$ state. From the analysis of Flannery, et.al. [49] it is pointed out that the reaction channel where the secondaries are formed in the $A^2\pi_u$ state is an order of magnitude more favorable than the $X^2\Sigma_g^+$ channel. As a result, the contribution to the total charge transfer cross section due to the $A^2\pi_u$ ions would be smaller than the population of this state in the reactant ion beam. It appears that certain excited state ions can charge transfer less efficiently than ground state ions and may have some influence on the magnitude of cross sections observed. An object of this research has been to probe the relative contributions of excited states in the $N_2^+ + N_2$ reaction.

IV: EXPERIMENTAL APPARATUS

IV.A: GENERAL DESCRIPTION OF THE SYSTEM

The experimental system can be divided, for the purpose of discussion, into three component parts: A mass-spectrometer, an ion-optics, and a charge-transfer section. See Figure 3.

The purpose of the mass spectrometer is to provide a mass-selected primary ion beam with known kinetic energy. The mass spectrometer system contains an electron-bombardment ion source, a gas inlet system, a vacuum pumping station, a pressure monitoring system and electronic controls.

The purpose of the ion-optics section is to direct and guide the transport of the primary ion beam from the mass spectrometer analyzer exit at the ring-drawout (R/D) electrode to the charge-transfer-cell (CTC). This is done by employing conventional ion optic techniques with lens elements that are of three basic geometric configurations: cylindrical, disc, and flat plate type. The electrical potentials on all optical elements are separately controlled by regulated power supplies to obtain a stable ion beam of maximum intensity at the CTC section.

The charge-transfer-cell section consists of three parts: The charge transfer cell, the charge transfer cell screen (CTCS), and beam flag two (BF2). This section is utilized to detect and measure the primary and product ions made in the charge transfer process. Detection of the ion beam is done by absolute current measurement using three

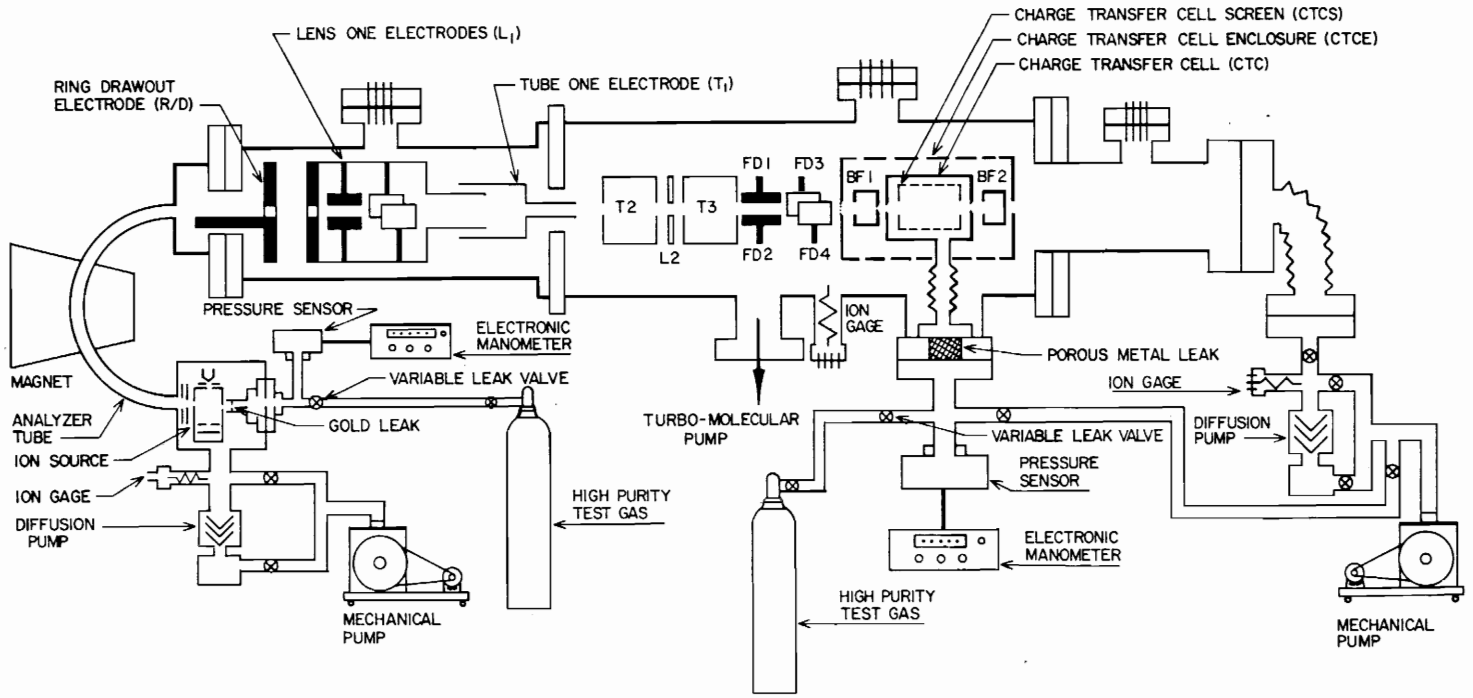

Figure 3.- Schematic Diagram of the Total System.

precision electrometers to measure total currents to CTC, CTCS, and BF2.

It is important that the apparatus be maintained in the 10^{-6} torr pressure range. This is accomplished by three separate pumping stations. The volume enclosing the mass spectrometer, lens one optic section and T_1 is maintained at working pressures of 2-4 x 10^{-6} torr by a 2-inch, 80-liter-per-second oil diffusion pump and mechanical pump arrangement. The volume enclosing T_2 and BF_2 is maintained at working pressures of 5 x 10^{-7} to 5 x 10^{-6} torr using a 400-liter-per second turbo-molecular pump. Another 2-inch, 80-liter-per-second oil-diffusion and mechanical-pumping station was used to help evacuate the volume at the exit of the charge transport cell.

A photograph of the total system is shown in Figure 4.

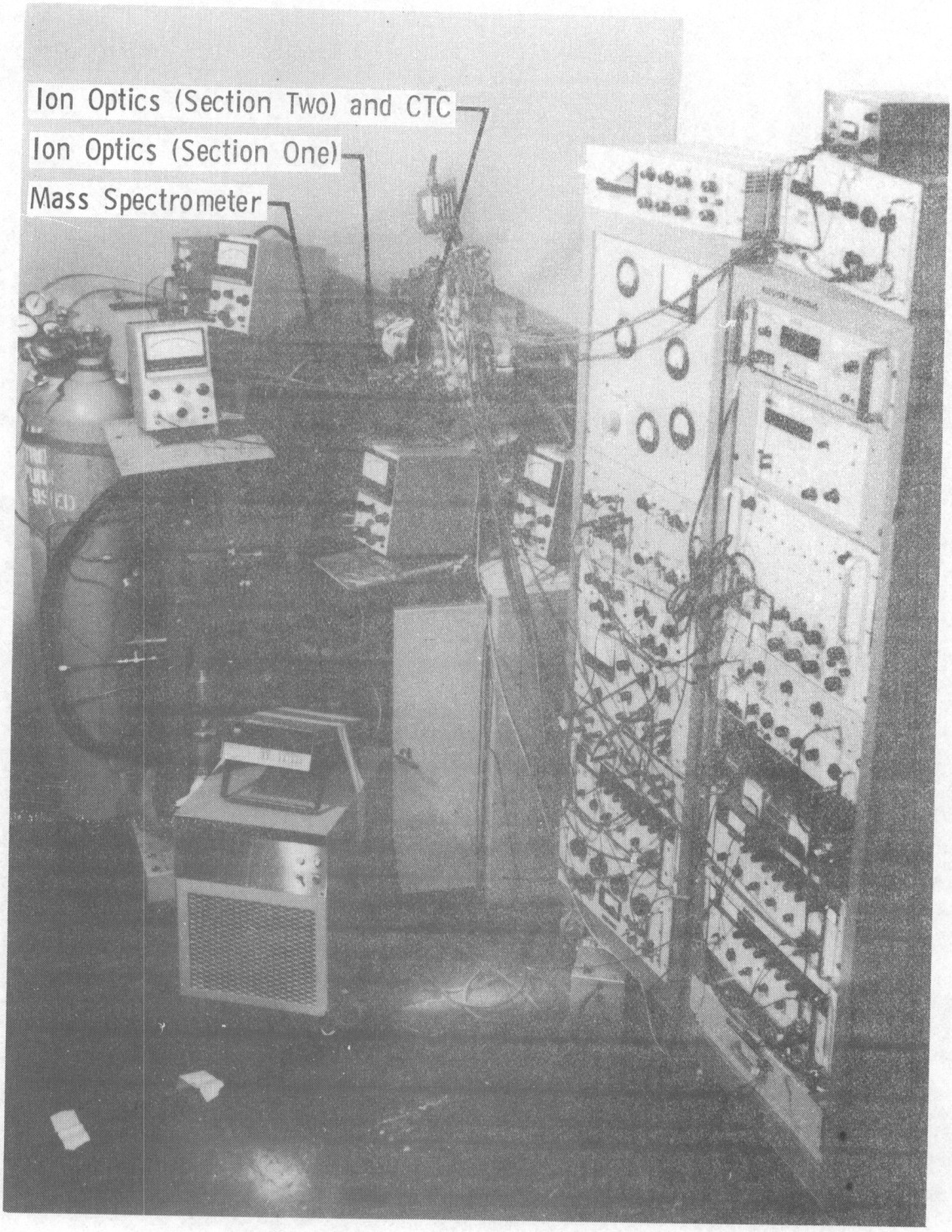

Figure 4.- The Charge Exchange System.

IV.B: DESCRIPTION OF THE MASS SPECTROMETER

The mass spectrometer used for this work is a Consolidated Electrodynamics Corporation model CEC 21-401. It is a 6.35 cm radius, 160° magnetic sector instrument capable of giving accurate mass selection for ions up to a mass-to-charge of 100 (a.m.u.). Figure 5 is a schematic of the mass spectrometer. A diagram of the electron bombardment ion source and its electronic circuitry is shown in Figure 6.

Electrons are emitted from the heated tungsten or rhenium filament F which is well-removed from the ionization chamber (block). Electrons emitted from F are attracted to the grid G by maintaining G at a potential of +30 volts with respect to the filament. The grid and block have small slits, 1.0 mm by 1.5 mm, to allow only a well-collimated electron beam to enter the ionization chamber. The energy of the electrons which enter the block is controlled by a regulated power supply whose output is varied from zero to the desired electron energy potential ϕ_{EE}. Within the ionization region or block, there are only weak electric fields due to the repeller electrodes. The ion source is designed to shield the perturbing forces due to the electrical field of the electron trap (anode); the anode is the electron beam collector.

The total emission current, block current, and anode current are separately monitored with panel-type micrometers. The filament was powered with a 6.3 volt, 6 ampere, 60 hertz transformer. The primary

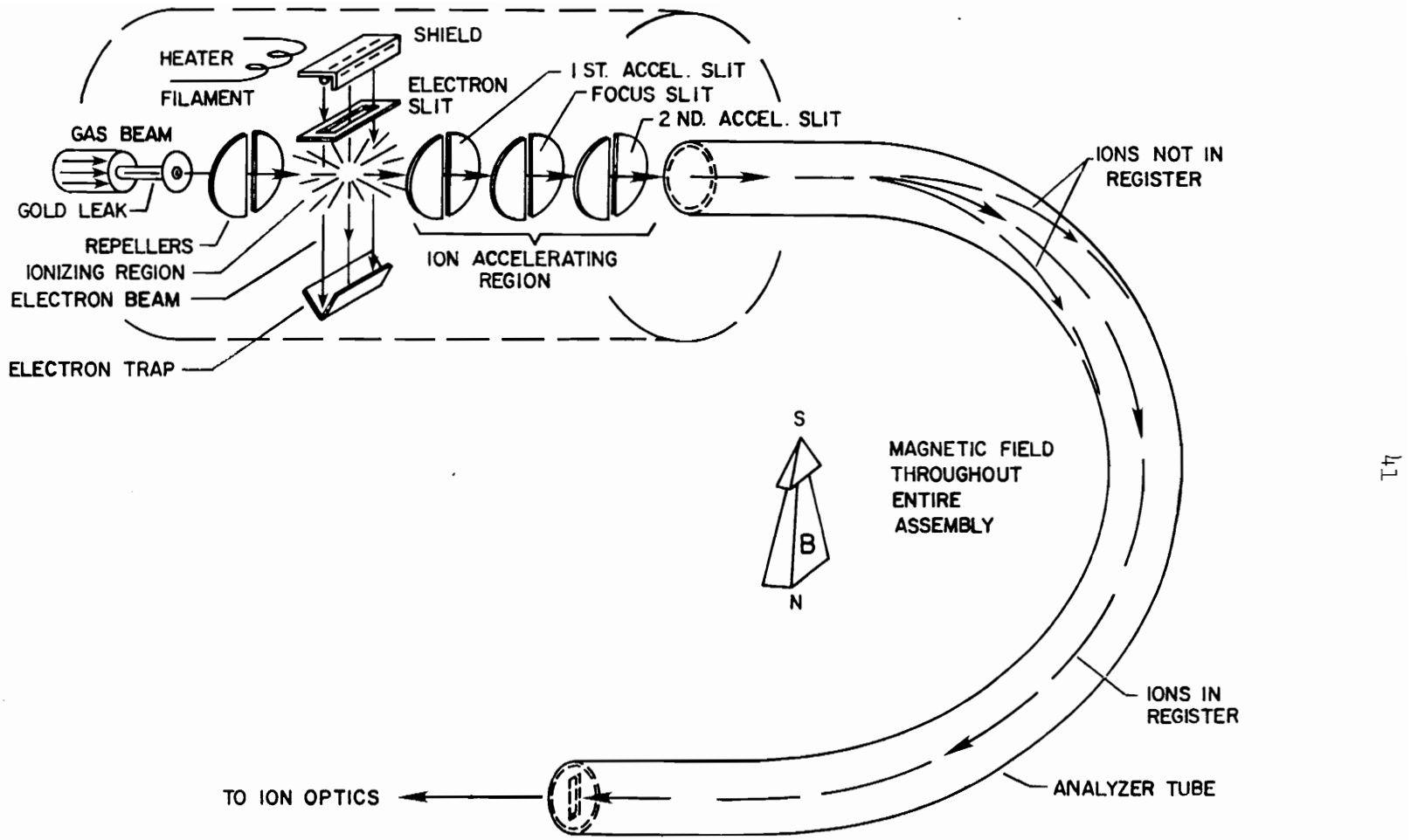

Figure 5.- Mass Spectrometer Schematic.

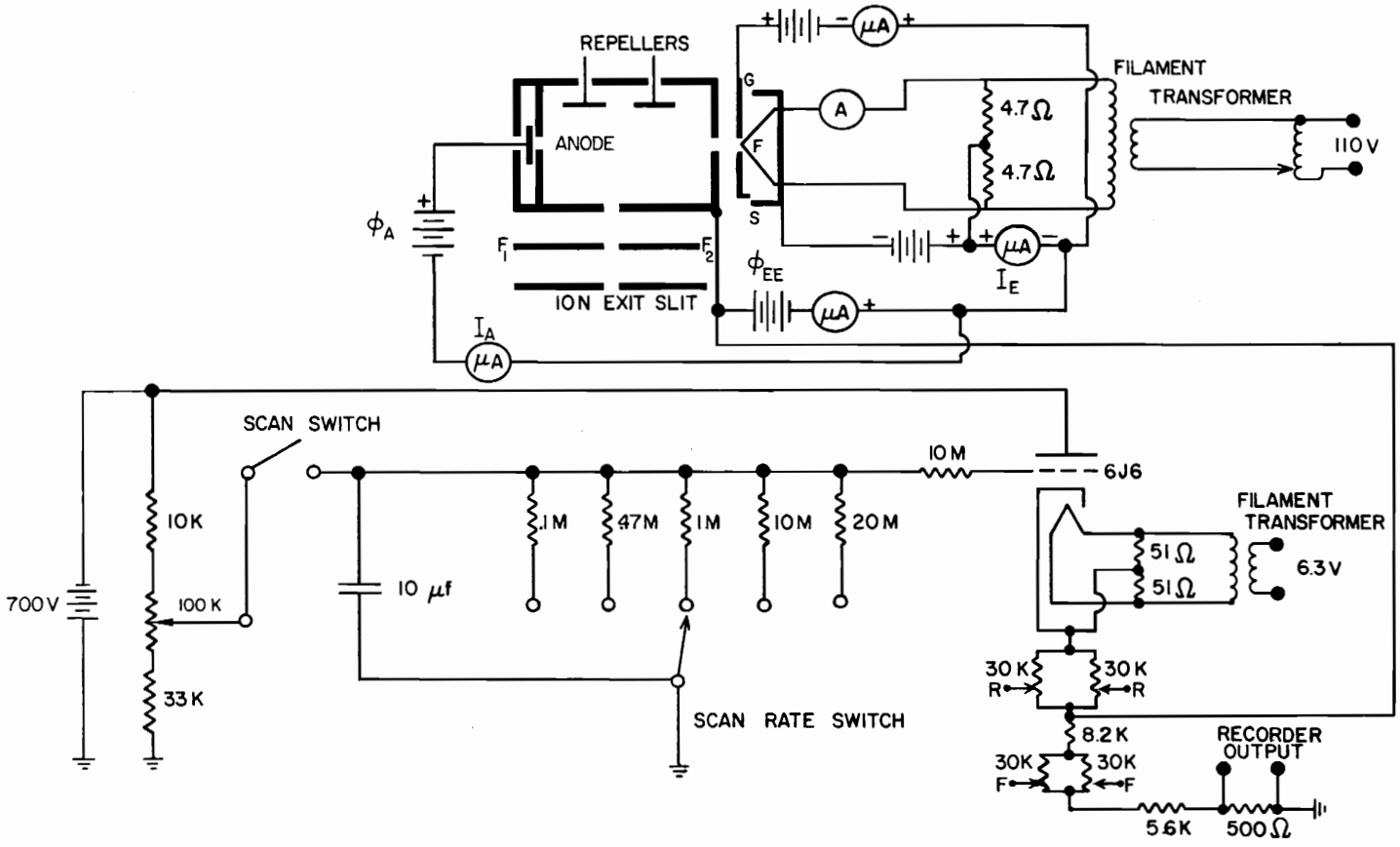

Figure 6.- Ion Source Electronics.

of the filament transformer was powered by a Variac connected to an ac line voltage regulator to help maintain constant emission currents. Typical operating conditions were 4.5 amp and 3.5 amp filament currents for tungsten and rhenium filaments, respectively. A block heater was used to maintain the block at the recommended operation temperature of 525 K. This heater was powered by a regulated dc power supply; normal heater operation required 2 amperes at 6.5 volts. The temperature of the ion source was monitored with a copper-constantan thermocouple connected to the block. An ice point reference was used with the thermocouple to provide absolute temperatures of the ion source as determined with a strip chart recorder. Ion source temperature, as monitored, was held at 525 $\pm$ 1 K.

The potential of the electron trap was maintained 300 volts positive with respect to the filament by a variable and regulated power supply.

The ion source is mounted in the analyzer tube such that the electron beam is collimated by a magnetic field of approximately 300 gauss. The ionization region is bounded by the block entrance slit and the exit slit to the anode. Within the block are two repeller plates that are maintained positive with respect to the block to give the ions an initial momentum in the direction of the block exit slit. The magnitude of the repeller potentials depends upon other source operation conditions, for example, the value of ϕ_{EE}. The repellers direct the ions toward the region of acceleration and provide the maximum stable ion beam from the source. Outside the block are two

focus plates, F1 and F2, which are maintained at a negative potential with respect to the block. The function of the focus plates is to physically and electrostatically concentrate the ion beam into the region of acceleration and to pass the maximum number of ions through the ion exit slit into the analyzer. The potential between the block and ion exit slit is controlled by the ion source electronics and is referred to as the ion acceleration voltage, ϕ_{IAV}. For N_2^+, this voltage was set at 473 volts. When the ions emerge from the ion exit slit, they enter the analyzer with a known kinetic energy. Within the magnetic analyzer, they travel along an arc of a circle of R centimeters in radius, where

$$R = \frac{144(M\ \phi_{IAV})^{1/2}}{B} \qquad (25)$$

In equation (25), B is the magnetic induction in gauss, M is the mass-to-charge of the transmitted ion in amu, and the ion acceleration potential is measured in volts. For N_2^+, a magnetic field of 2610 gauss was typically used. The ion acceleration potential is controlled by a 10-turn potentiometer; the magnetic induction of the permanent magnet field is controlled with adjustable shunts. The shunts are positioned by an electric motor operating through a continuously variable speed transmission.

The electronic control circuit of Figure 6 was designed to provide the proper potentials for the ion source. It is powered by a John Fluke Manufacturing Company, dc voltage standard, model no. 332D.

Energizing the input voltage in the grid circuit by closing the scan switch establishes a method of scanning electrostatically. Scanning times are controlled by the RC time constants in the grid circuit. The circuit design is the cathode follower type where the cathode terminal is common to both the input and output circuits. Thus, an increase of grid-to-ground potential tends to increase the plate current and consequently, to increase the cathode-to-ground voltage. It is this cathode-to-ground voltage divider network that supplies the proper potentials for the ion source, repeller plates, and the focus plates; such that, ions made in the source are accelerated from the source in the direction of the ion exit slit.

IV.C: THE MASS SPECTROMETER INLET SYSTEM

The inlet system provides the means for the continuous introduction of gas into the mass spectrometer ion source at controlled pressures. Pressure attenuation is obtained with a leak valve and a performated gold foil diaphragm. See Figure 3. After attenuation, the pressure in the ion source was below 10^{-4} torr. Typical operation with nitrogen gas requires a pressure of 25-50 x 10^{-3} torr on the back side of gold leak for a corresponding pressure of 3-6 x 10^{-6} torr to be indicated by an ionization gage on the vacuum inlet system. The pressure on the back side of the perforated gold leak is continuously monitored with a Datametrics Corporation, Barocel Pressure Sensor, model number 570A. Digital pressure readouts from the barocel pressure sensor were obtained with an electronic manometer, Datametrics Corporation, model number 1018.

The exhaust vacuum system consists of a mechanical fore pump, a 2-inch oil diffusion pump, and a cryogenic trap. The cryogenic trap was filled with denatured alcohol and maintained at a temperature of approximately -100 degrees Centigrade, using a Neslab Instruments Incorporated model number cc-100f refrigeration unit. This vacuum system is capable of attaining ultimate pressures in the 10^{-8} torr range.

IV.D: ION-SOURCE OPERATIONAL CHARACTERISTICS

This section discusses data taken on the performance parameters needed to characterize the ion source in operation. The ion source is the most important single component of the ion-beam system. Its characteristics determine to a great extent the performance of the entire system. For this reason, a considerable amount of effort was expended on ion-source characterization.

In order to set the proper operating pressures for the ion source inlet system, it was necessary to obtain the conductance of the gold leak used to attenuate the gas-inlet-system pressure to the ion-source pressure. This was done by removing the ion source flange inlet system, with the source and gold leak in place, and adapting it to a leak detector pumping station for calibration. A special vacuum housing adapter was fabricated for mounting the ion source flange and gold leak represented by the porous metal leak, shown in the test apparatus of Figure 7. The apparatus could then be evacuated to the 10^{-6} torr pressure range and leak tested with the leak detector pumping station. The technique used to determine the gold leak conductance was to trap a test gas (nitrogen) at a known pressure and volume and to monitor the pressure over a selected period of time. A Volumetrics Corporation model VM volume controller was used as a reference volume (V_c) of 0.209 liters. To use this technique an unknown volume (V_x), bound by the volume controller (with piston in extreme bottom position), V_1, pressure sensor, and V_3 was needed. The

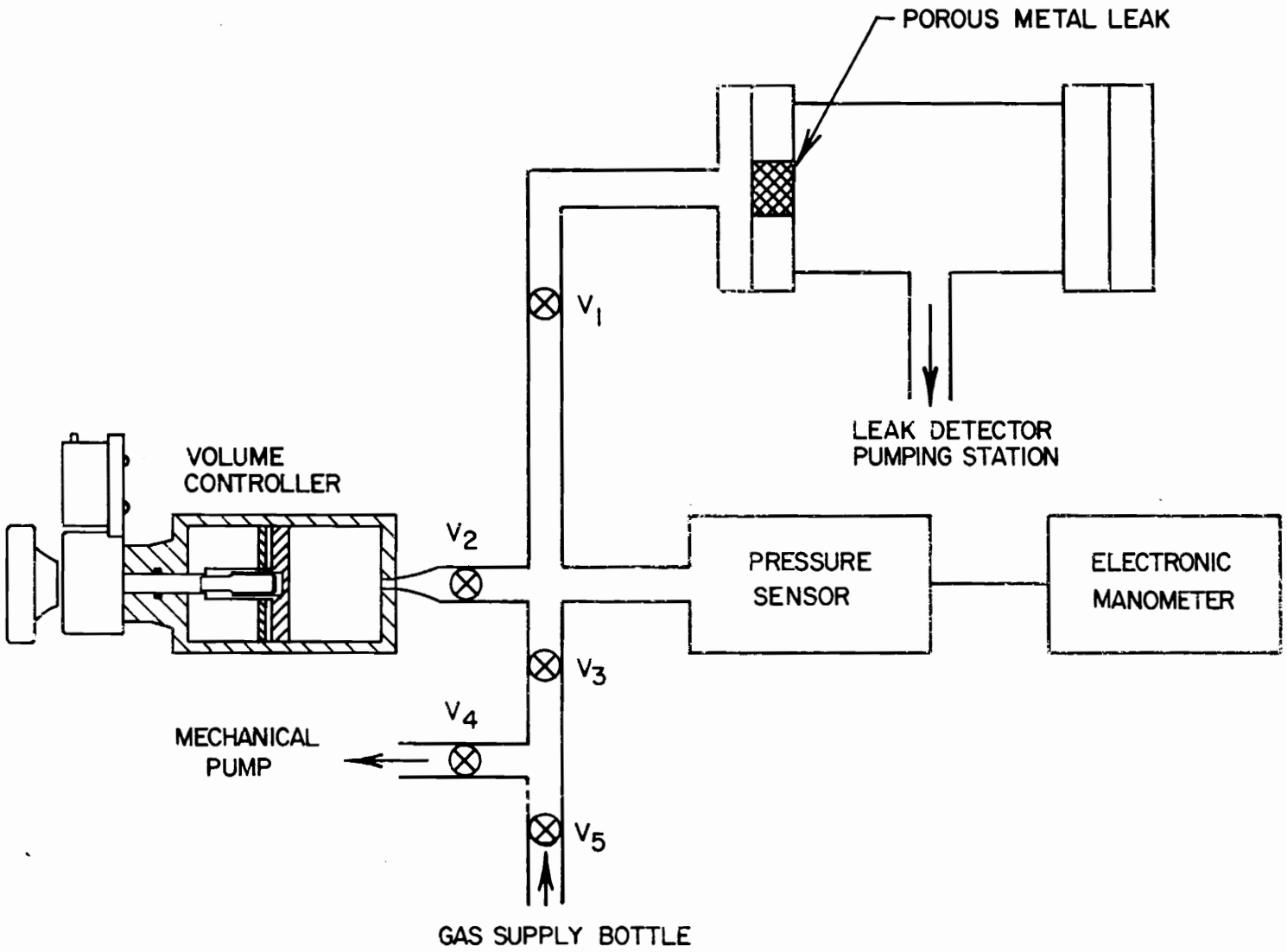

Figure 7.- Vacuum Conductance Measurement System.

volume between V_1 and the porous leak could be neglected. The unknown volume was obtained by closing the volume controller until the piston was at the extreme bottom position and evacuating the enclosed volume with the mechanical pump. V_4 and V_1 were then closed and the system pressurized with test gas through V_5. The initial pressure (P_i) was then recorded as indicated by the pressure sensor and electronic manometer. The volume controller was then opened until the piston was at the extreme top position, as indicated by a counter. A final pressure, P_f, was then recorded and the unknown volume was calculated with Boyle's law:

$$V_x = \frac{P_f V_c}{P_i - P_f} \tag{26}$$

Having determined this unknown volume (V_x) and knowing the controller volume (V_c), the conductance of the gold leak was determined by setting an initial pressure on the back side and monitoring the pressure as it decreases over a reasonably long period of time. The results of this test are shown in Figure 8. The pressure decreases in the trapped volume according to the following expression:

$$\frac{dP}{dt} = - \frac{C \cdot P}{V} \tag{27}$$

where C, P, and V are the porous-leak conductance, trapped gas pressure, and trapped gas volume, respectively. Simple integration yields:

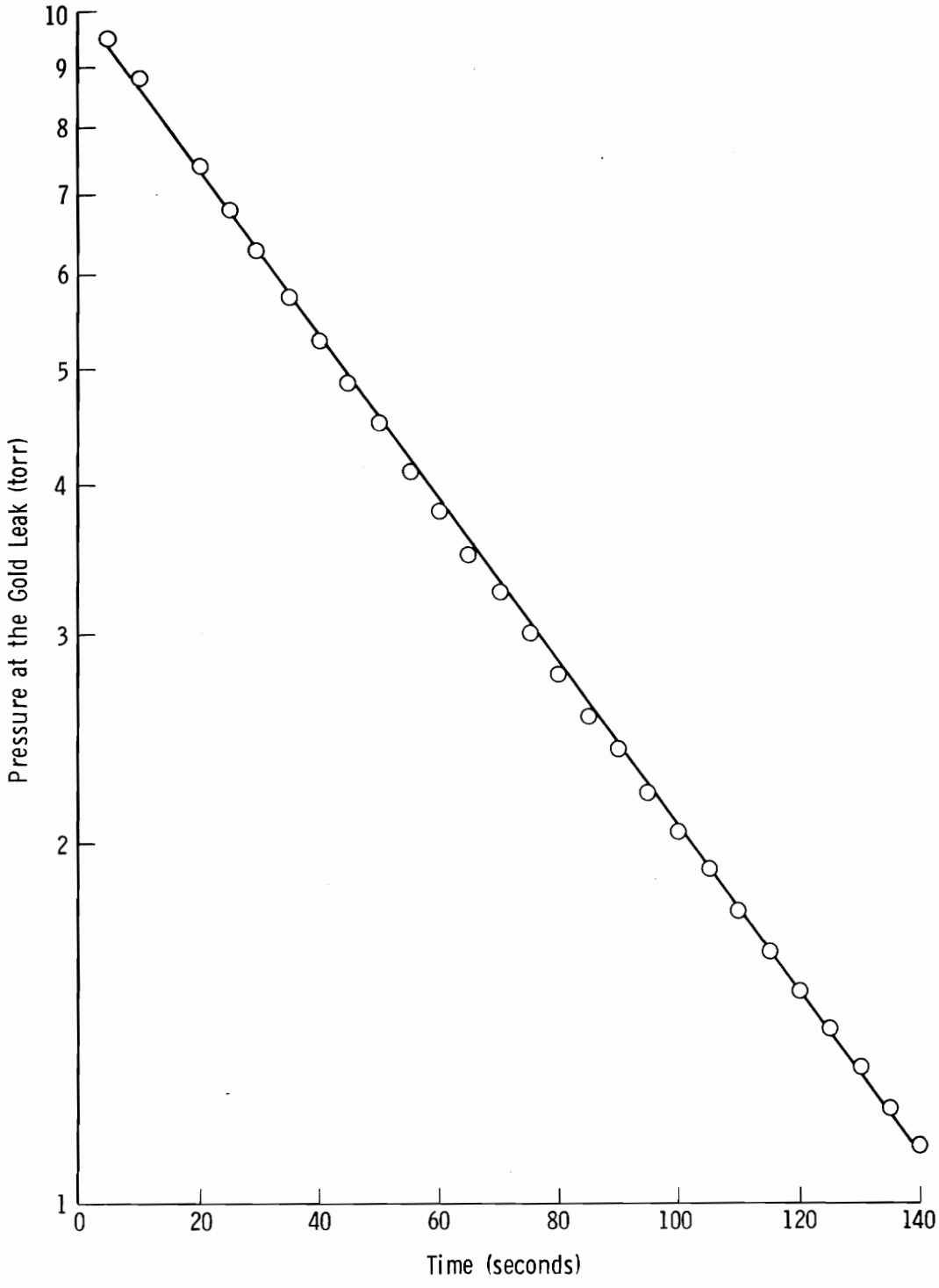

Figure 8.- Pressure-Time Plot for the Gold Leak.

$$C = \frac{V}{t} \ln\left(\frac{P_i}{P_t}\right) \qquad (28)$$

In the last expression P_i is the initial pressure and P_t is the pressure at the time t in the trapped volume. The gold-leak conductance was determined to be 3.7×10^{-3} liters/sec. The linear plot of pressure versus time on semilogarithmic paper indicates free molecular flow through the gold leak. The correlation between the pressure at the gold leak and the mass spectrometer background pressure is shown in Figure 9. This graph illustrates the typical straight-line relation which is expected of such a plot. During operation, reference was repeatedly made to Figure 9 to insure that the ionization gage on the mass spectrometer and the pressure sensor at the gold leak were giving proper readings.

Another important parameter is the strength of the magnetic induction. Since we have no direct indication of magnetic induction, it was necessary to obtain this field strength as a function of shunt gap. Figure 10 shows a plot of the magnetic induction in gauss as a function of the shunt gap. This data was obtained by removing the analyzer assembly and mounting the probe of a gaussmeter in the center of the magnet pole face. Reference to this data allows one to set the proper magnetic field required to focus different ionic species at a chosen ion energy.

At the completion of the above preliminary measurements, it remained to transport the mass-selected ions (arriving at the end of

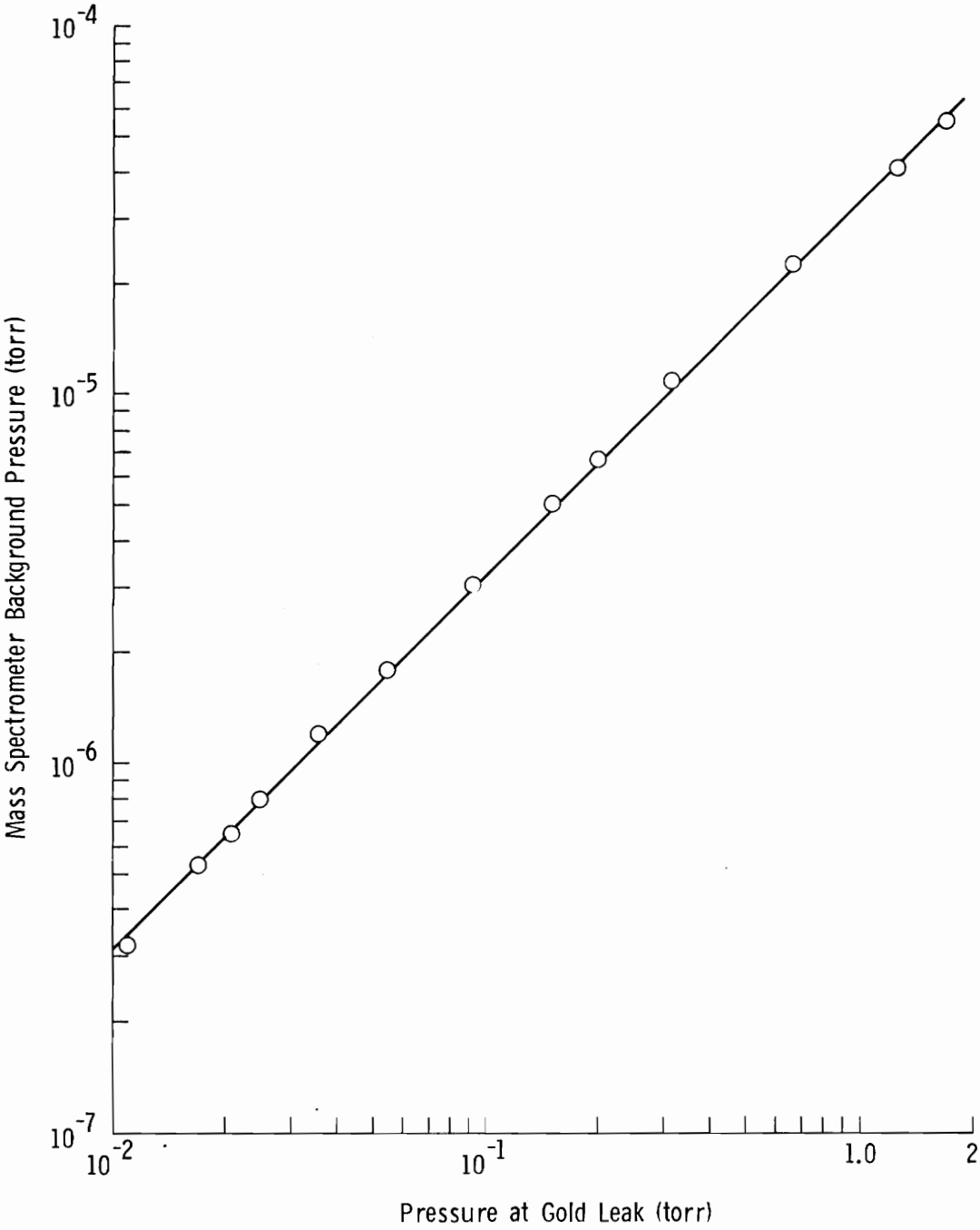

Figure 9.- Mass Spectrometer Background Pressure as a Function of Pressure at the Gold Leak.

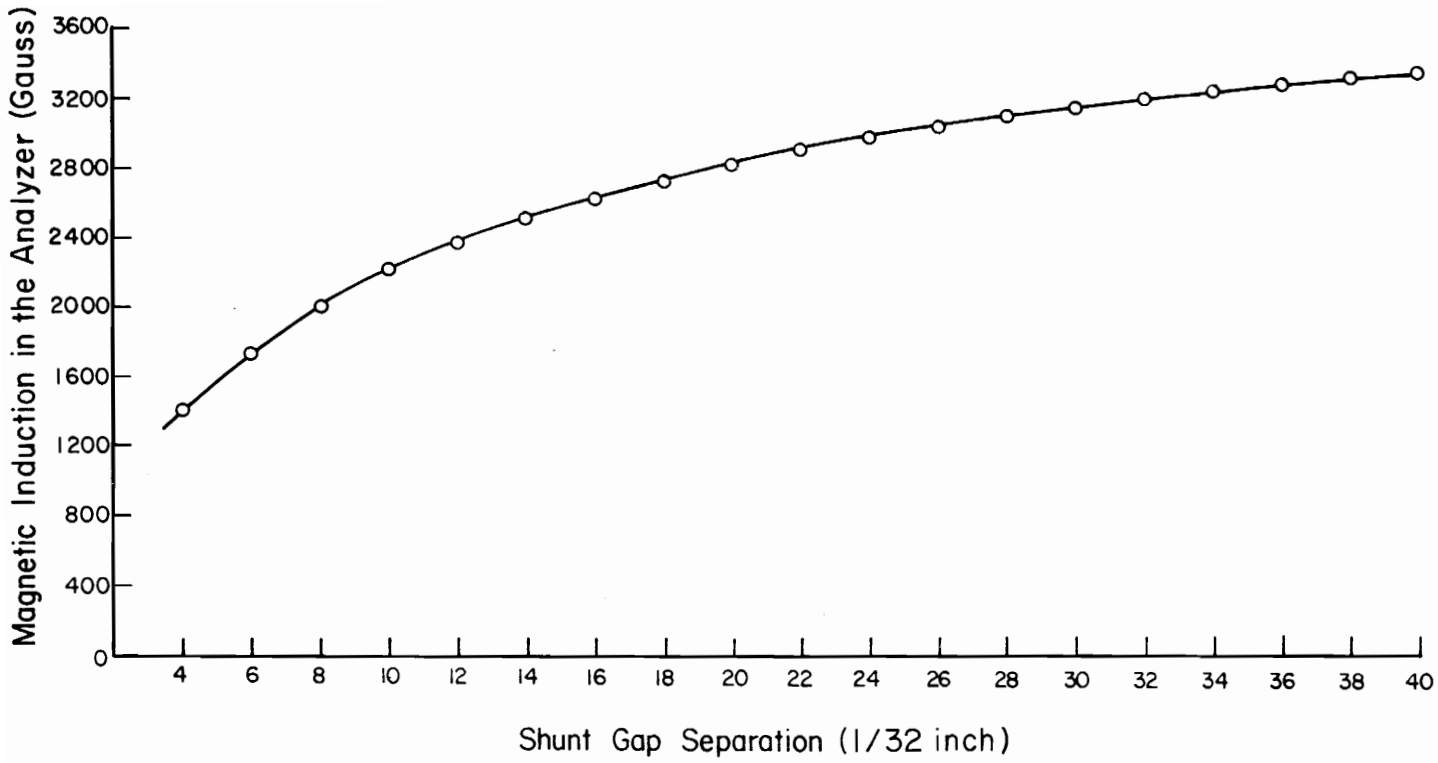

Figure 10.- Magnetic Induction versus Shunt Gap.

the mass analyzer) into the charge-transfer region and to demonstrate that the system performs as a mass spectrometer. This required the development of ion optics elements to guide and focus the transmitted beam to a collector (see Figure 11).

IV.E: ION-OPTICS SECTION 1

For the purpose of discussion and for understanding some preliminary measurements, the ion optics is considered to consist of two sections. The purpose of section 1 is to collimate and focus the ion beam as it exits the CEC 21-401 spectrometer. This section is composed of six elements. See Figure 11. Element 1 is a combined circular grid and deflection plate; it was named the Ring/Drawout electrode, R/D. Electrodes 2, 3, 4, and 5 form a combination lens and deflection plate system, L1. Element 6 is denoted as T1 (or tube 1). In practice, the deflection plate functions of L1 have not been found necessary. The wiring and inter-element dimensions for section 1 are shown in Figure 12. All elements are made of nonmagnetic 316 stainless steel. The aperture diameters of elements 1, 2, 3, and 4 are 0.375 inch. The internal diameter of element 5 is also 0.375 inch. The smaller and larger ID of T1 are 0.375 and 0.750 inch, respectively.

The magnitude and stability of the ion beam current obtained at the exit of element 6 was increased by the addition of a 50 x 50 tungsten grid mesh, 0.001-inch-diameter wire (92% transparency) at the entrance of element 5. Apparently the grid addition improved the focusing characteristics of this section. Constant potentials (ϕ) are maintained on all elements by three regulated power supplies connected as shown in Figure 12.

Optics elements 3 and 4 were made as halves of a split ring. Since the deflection capability was not required, both parts of each

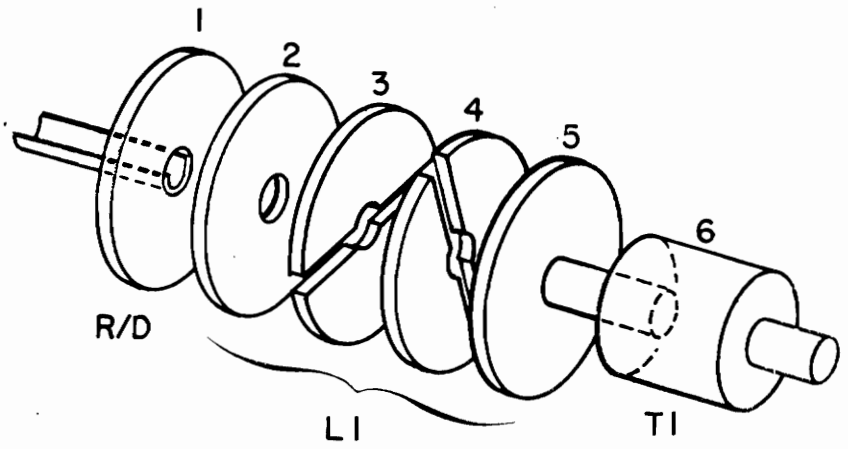

Figure 11.- Ion-Optics Section 1.

split ring were permanently tack welded together with a thin piece of tantalum metal. Similarly, elements 2, 3, 4, and 5 were given permanent electrical interconnections.

Elements 1 through 5 have four equally spaced mounting holes drilled on a 1-inch bolt circle for a slip fit to a 1/8-inch-diameter ceramic (Al_2O_3) rod. Each element is stacked on the ceramic rods in sequence with ceramic spacers over the rods of the dimensions A and B shown in Figure 12. The mating flange at the exit of the mass spectrometer analyzer tube (Figure 12) was drilled with four mating holes, 1/4-inch deep, to accept the four ceramic rods. For additional rigidity and permanent support, element 1 was mounted to the analyzer mating flange on ceramic spacers with four 4-40 nylon screws. The stacked elements are held together with a special designed lock ring that locks over the ceramic rods. This lock ring was manufactured specifically for holding ion optic elements together using the 1/8-inch-diameter rods. Element 6 is supported by a 1/2-inch-wide, cylindrically shaped piece of teflon machined for a tight fit into a 5-inch vacuum tee section with conflat mounting flanges. This vacuum tee section was used to connect the mating flange of the analyzer tube to the vacuum divider wall separating section 1 from section 2 ion optics elements. Copper wires insulated with ceramic beads were used to connect R/D, L1, and T1 to three ceramic-to-metal feedthroughs mounted on a 2.75-inch vacuum flange that mates with the flange of the vacuum tee housing.

Maximum transmission of the ion beam was obtained by an iterated multiknob diddle (MKD) technique. This involved the usual practice of

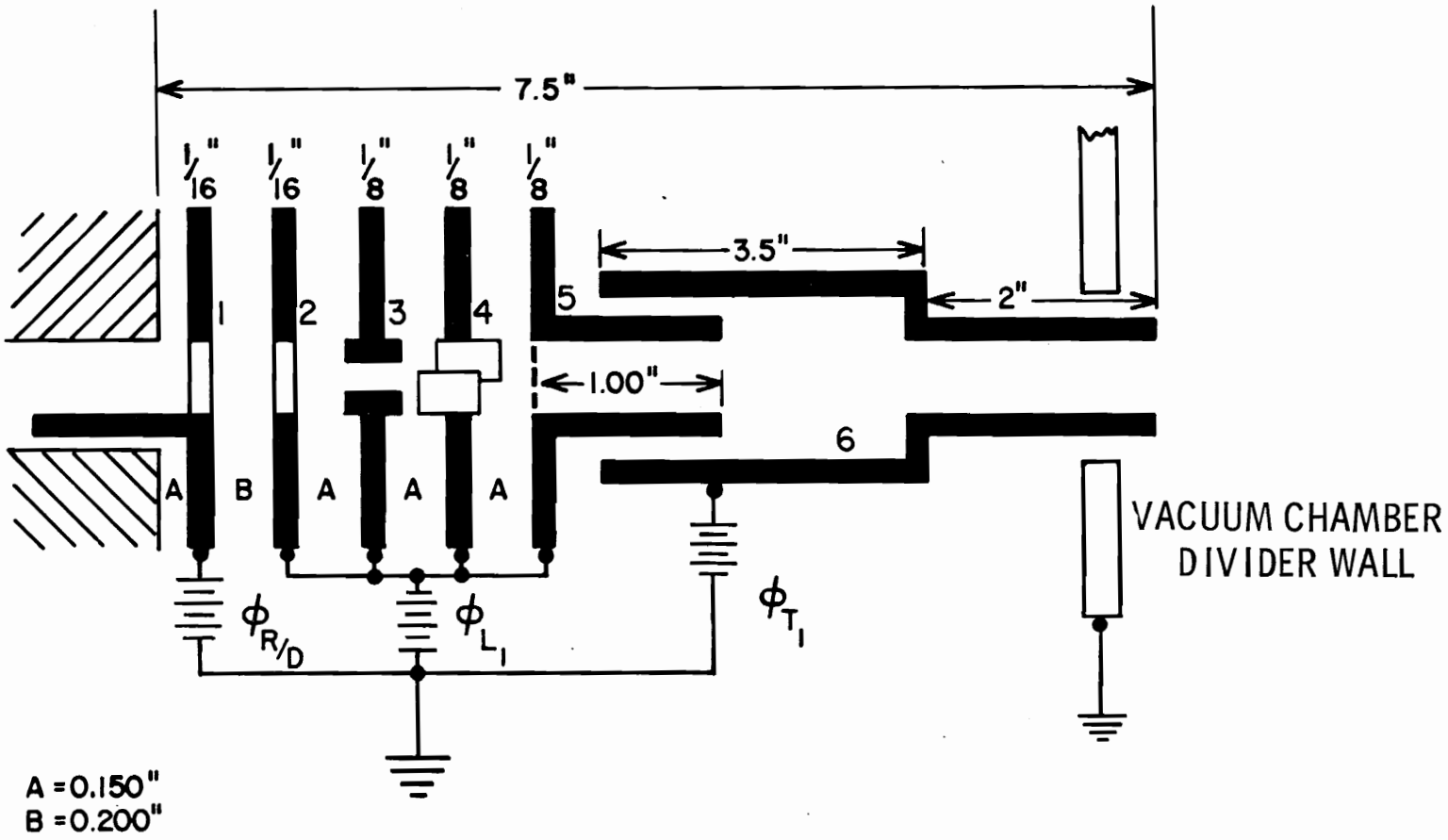

Figure 12.- Wiring of Optics Section 1.

successively varying the potential on all focusing electrodes. Several iterations are required before one is reasonably satisfied that the beam current has truly been maximized.

For a series of experiments on the ion transmission through the section 1 optics, an ion collector was located at the output of T1. See Figure 13. A double screen of tungsten mesh was placed between T1 and the collector and was maintained 2 volts negative with respect to the ion collector. The purpose of the double screen was to suppress secondary-electron emission from the ion collector. At ion acceleration voltages around 500 volts, typical ion beam currents of 5×10^{-9} amp were measured at the collector.

As a first test of ion beam production, the sensitivity of the mass spectrometer was determined for N_2 gas. A graph of ion current to the collector as a function of mass-spectrometer pressure is shown in Figure 14. From the data in this study, the mass spectrometer sensitivity is found to be 1.77×10^{-4} amps/torr N_2; this is within the accepted range for electron-bombardment ion sources.

Using the ion collector system shown in Figure 13, the experiments to characterize the performance of the ion source were completed with the section 1 ion optics tuned for maximum ion transmission. Figure 15 presents graphs of both collected ion-beam and collected mass-spectrometer electron beam currents as functions of the anode potential ϕ_A. It is noted that with the exception of some scatter in the data, the ion current increases linearly with anode current as the anode voltage is increased from 100 to 300 volts. The discontinuity

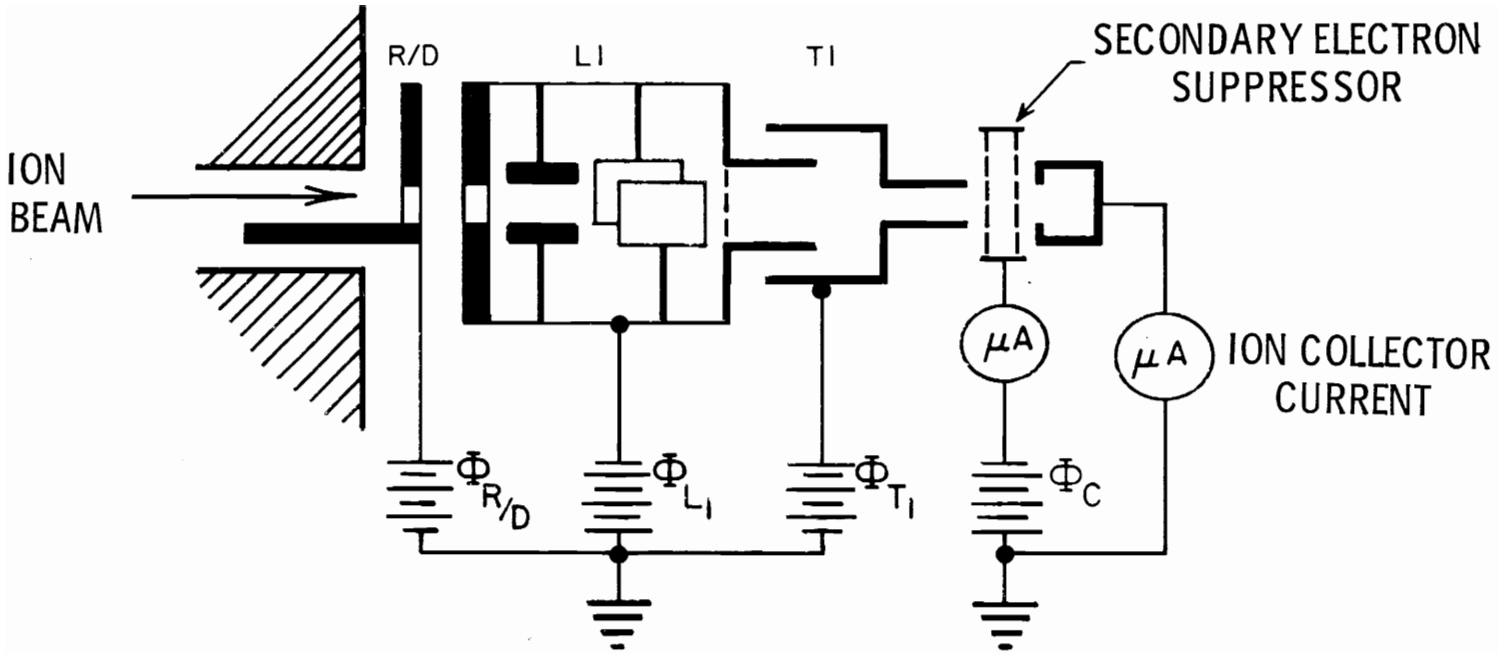

Figure 13.- Beam Transmission Experiment Ion-Optics Section 1.

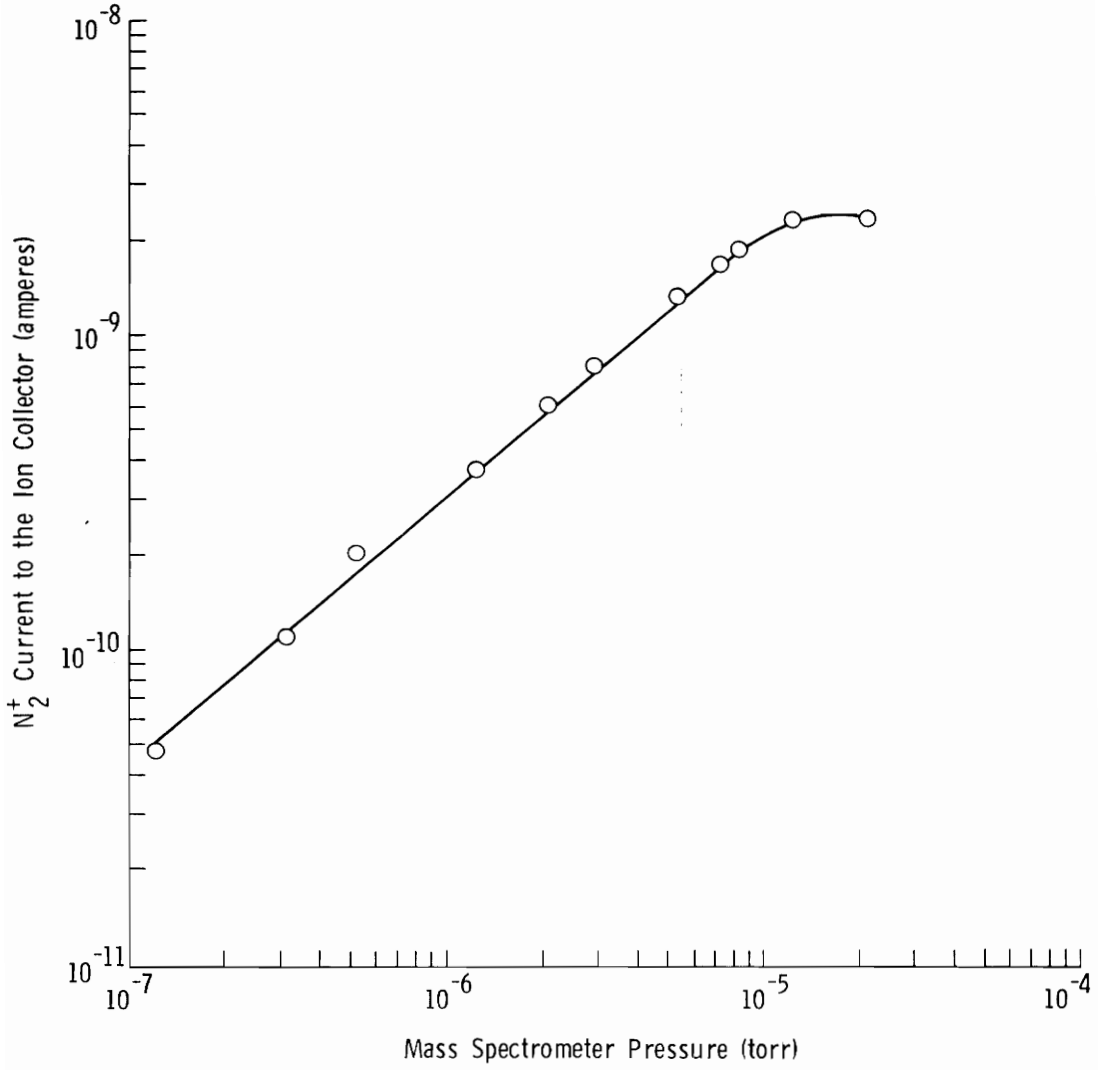

Figure 14.- Ion Beam Current versus Mass Spectrometer Pressure.

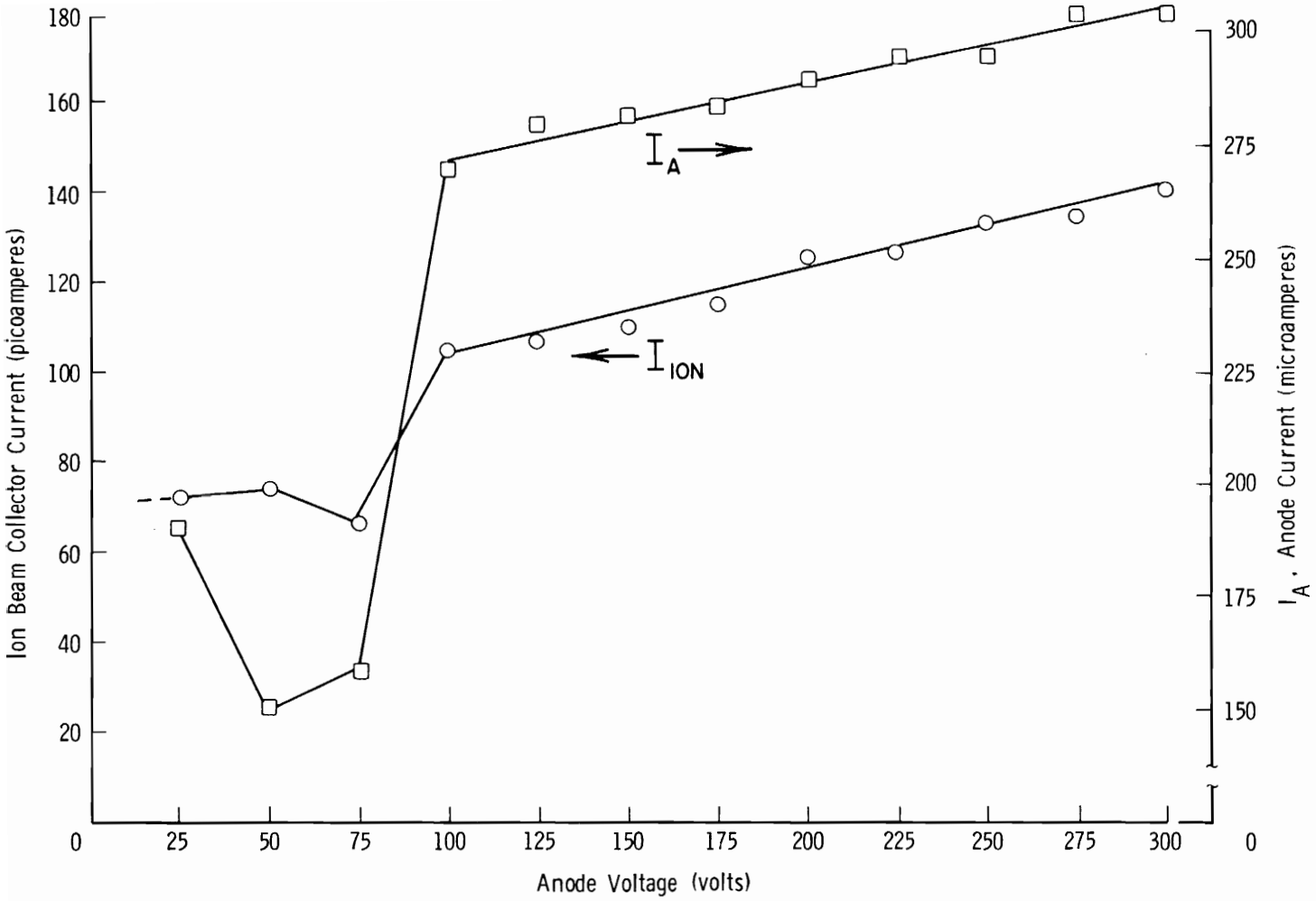

Figure 15.- Ion-Beam Current and Electron-Beam Current versus Anode Voltage.

below a 100-volt anode potential is explained by considering the potentials of the anode and block with respect to the source filament. For this data the block was maintained at 75 volts with respect to the filament. Therefore, if electrons are expected to be collected efficiently, the anode must be operated at a positive potential greater than the filament to block potential. It was decided to operate the anode voltage at a minimum of 100 volts with respect to the filament.

A graph of collected N_2^+ ion-beam current vs. total ion-source filament emission is shown in Figure 16. There are characteristic breaks in the curves which occur at approximately 500 and 650 μa total emission for anode voltages of 200 and 300 volts, respectively. It was noted that below these breaks there is less spread in the total emission data, and the ion current appears to increase linearly with emission current. The breaks in the curve were attributed to a space charge effect associated with the rather large magnitude of total emission current. Other phenomena such as ion-molecule reactions taking place within the ion source have been known to cause spurious effects in ion source operations. For this research it was necessary to keep the magnitude of ion current as large as possible but at the same time operate the source such that stable ion currents are maintained. Stable and repeatable ion currents were obtained operating at an anode potential of 300 volts and total emission current of 600 microamperes. These values were chosen as standard operating conditions.

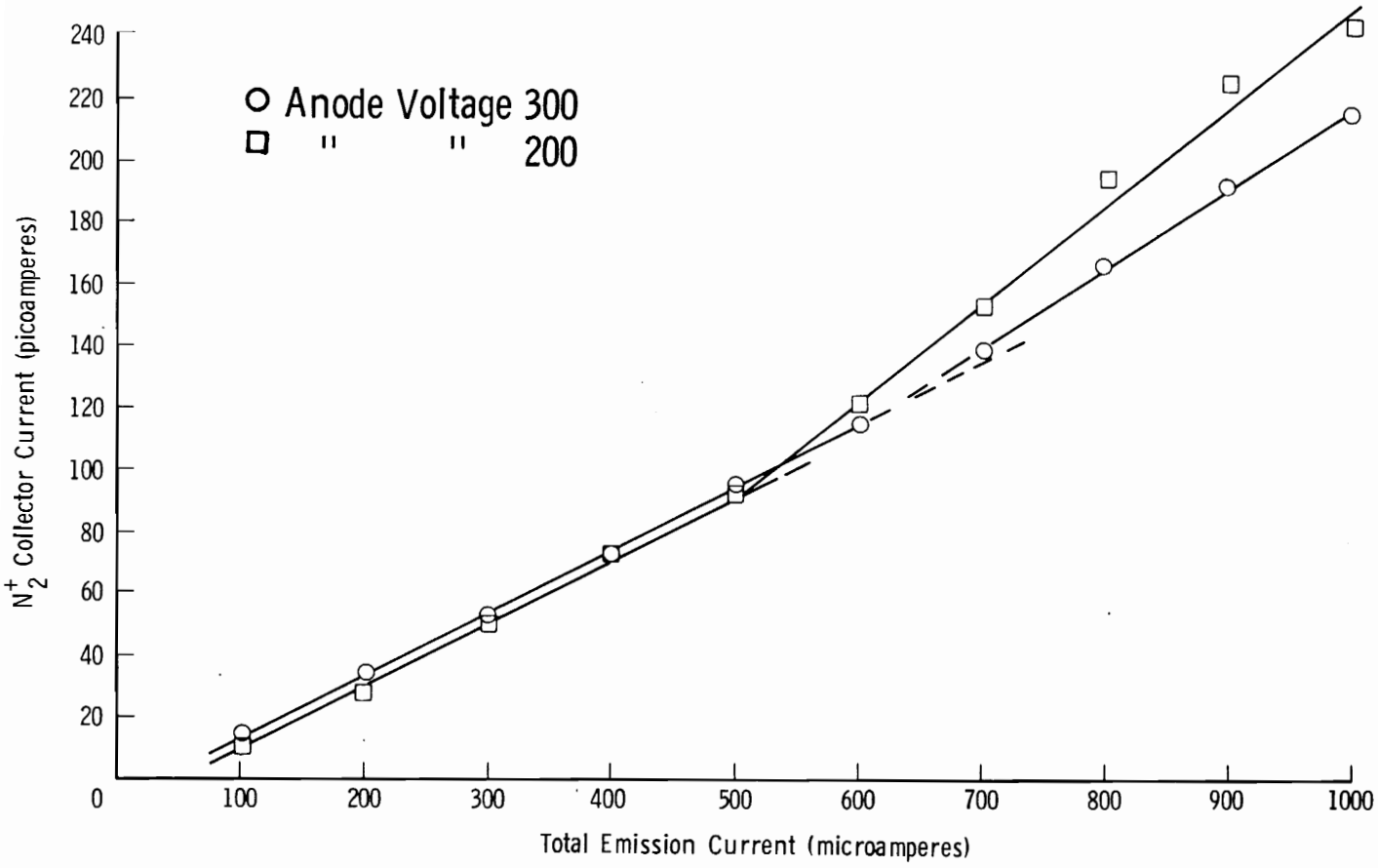

Figure 16.- N_2^+ Ion-Beam Current versus Total Filament Emission Current.

An important experimental parameter is the energy spread of the ion beam, i.e., the width of the energy distribution of the ions transmitted to the charge-transfer cell. This parameter can be of special importance when the ion beam is to be acted on by ion-optics elements. A distribution of ion energy can result from a number of causes such as spatial variation in the potential at points in the source where ions are created. Another source of energy spread can be the thermal energy of the ions, usually related to the temperature of the ion source. Generally, both of these effects contribute to the energy spread. The retarding-potential measurement was applied to obtain the data presented in Figure 17. In this retarding potential experiment, the polarity of ϕ_c was the reverse of that shown in Figure 13.

The kinetic energy distribution of the ion beam was obtained by graphically taking the first derivative ($\Delta I_c/\Delta\phi_c$) of ion abundance versus retarding potential. The absolute values of the reciprocals of the retardation curve slopes versus collector retardation potential are shown in Figure 18. From this data, it was found that the energy spread in the ion beam was approximately 1.5 electron volts, a result typical of electron bombardment sources.[86]

Since the current obtained at the ion collector was always much larger than that expected for secondary emission from stainless steel, it was decided to set ϕ_c to zero (See Figure 13). The effects of ion-optics elements R/D, L1 and T1 on collected beam current were then studied. From these studies, as summarized in Figures 19, 20, and 21,

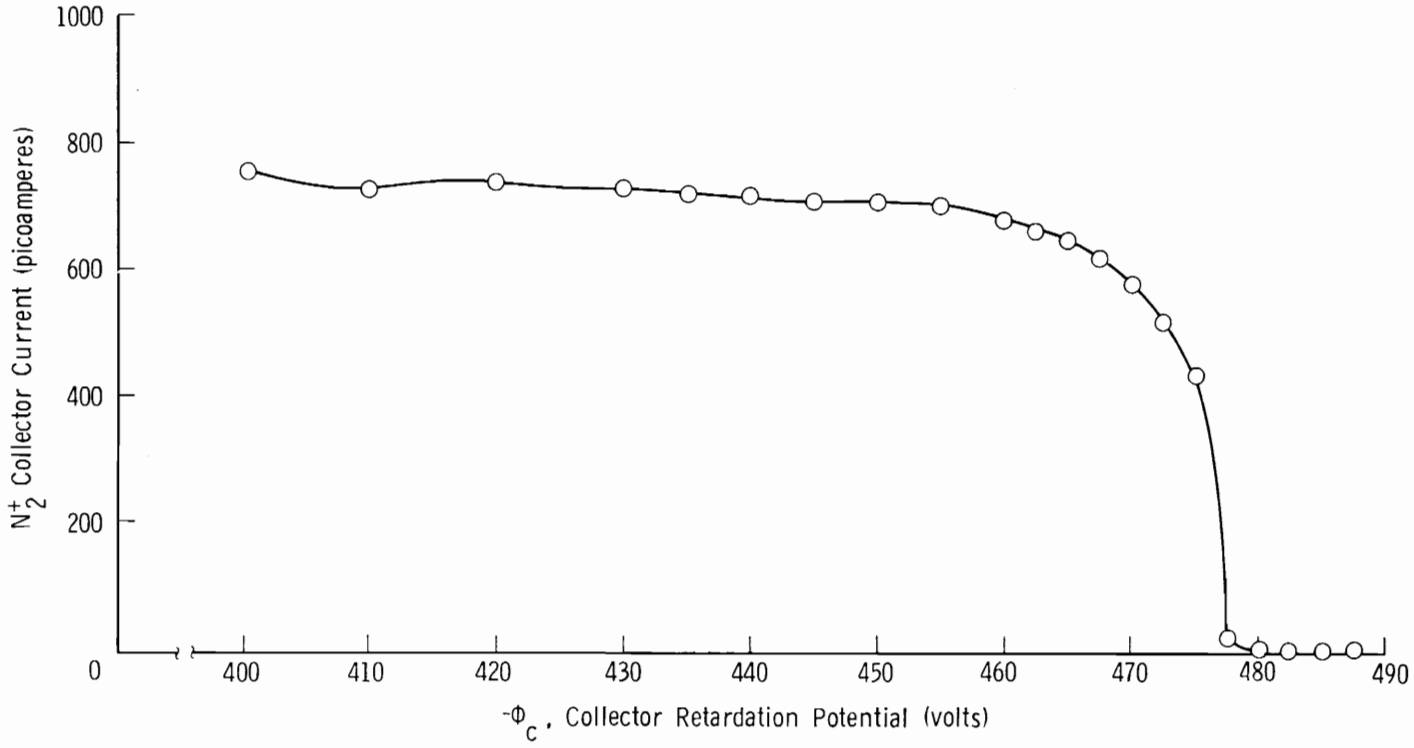

Figure 17.- N_2^+ Ion Beam Current versus Retarding Potential.

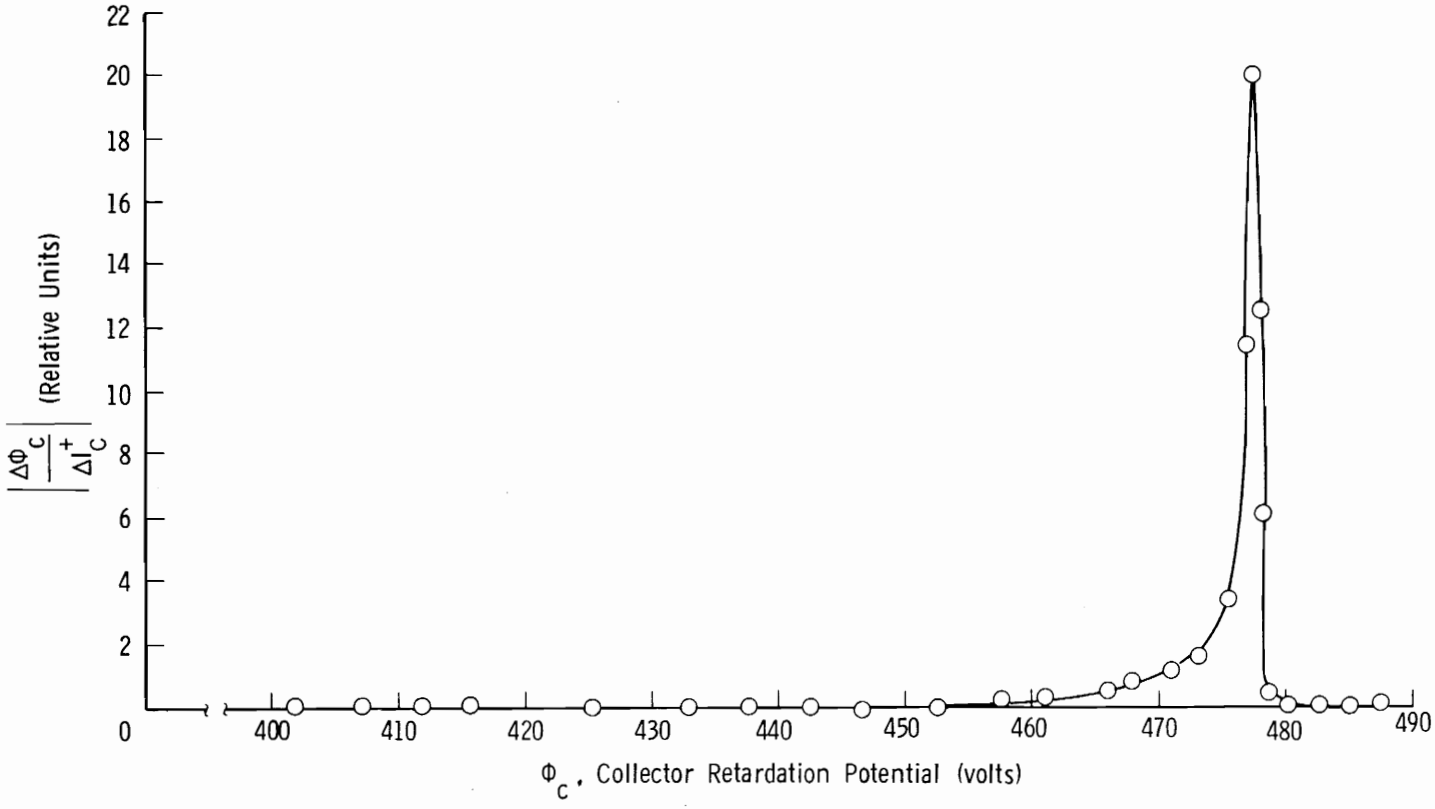

Figure 18.- $\left|\Delta\Phi_c/\Delta I_c\right|$ versus Φ_c.

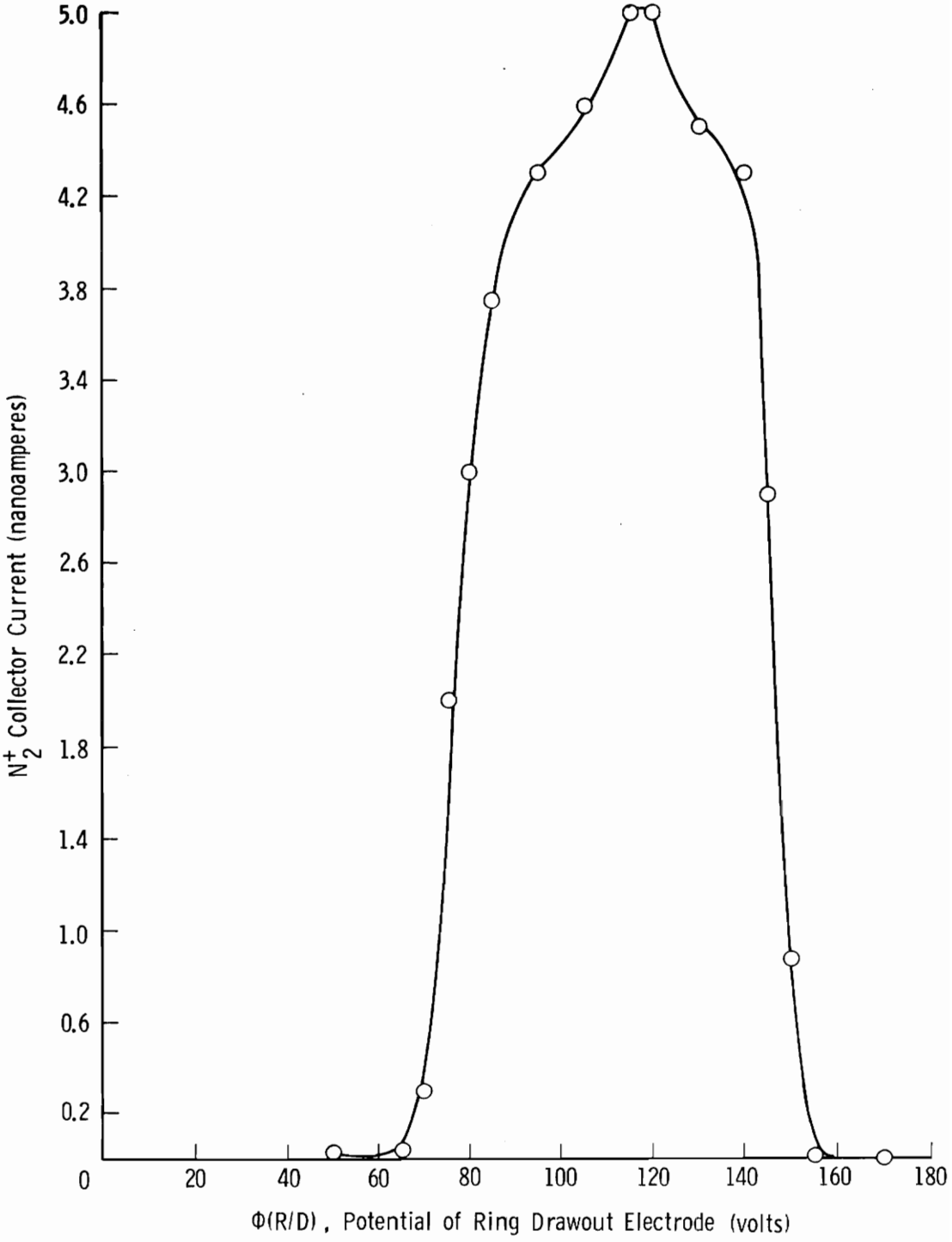

Figure 19.- N_2^+ Ion Beam Current versus Φ(R/D).

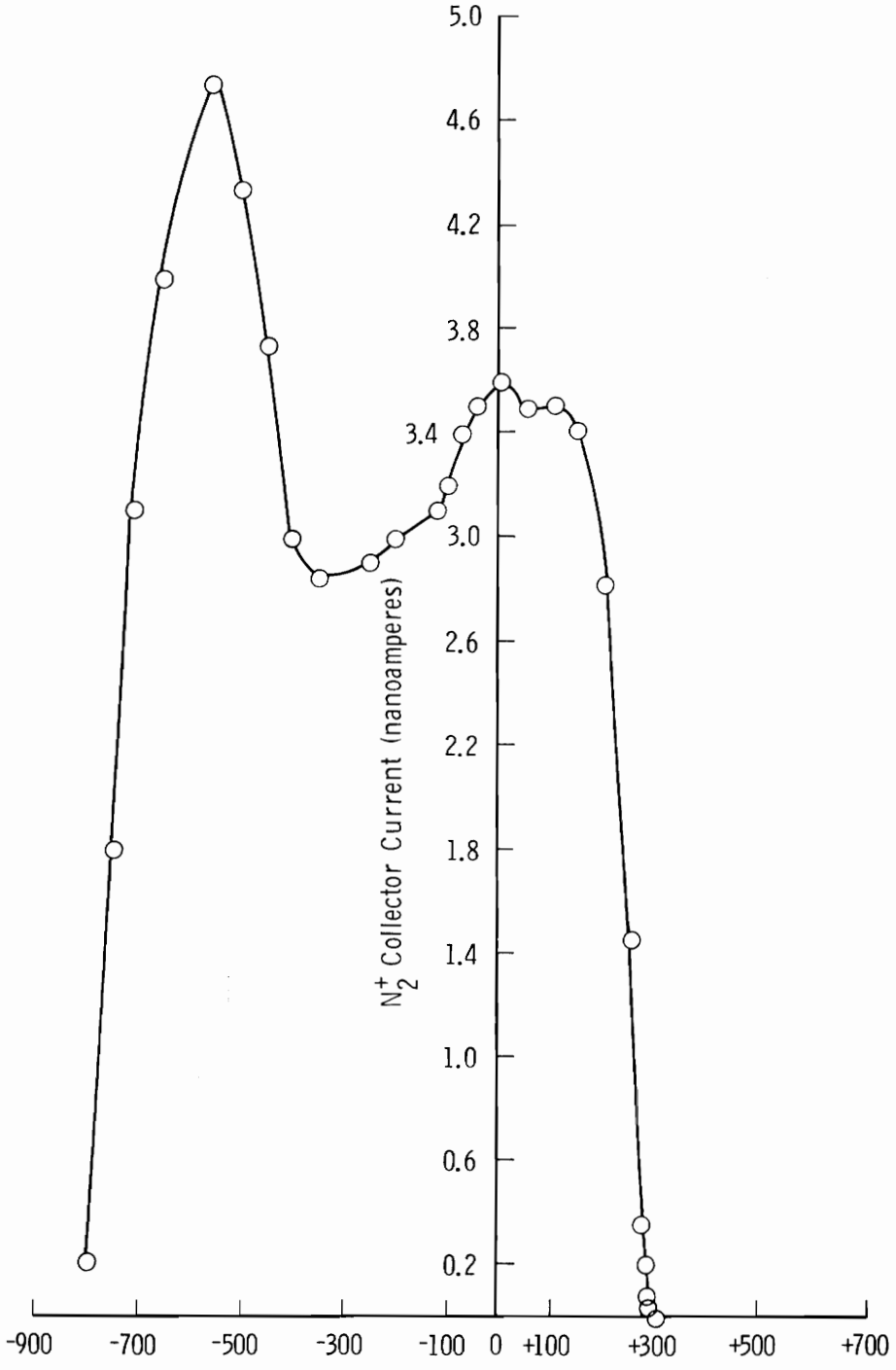

Figure 20.- N_2^+ Ion-Beam Current versus Φ(L1).

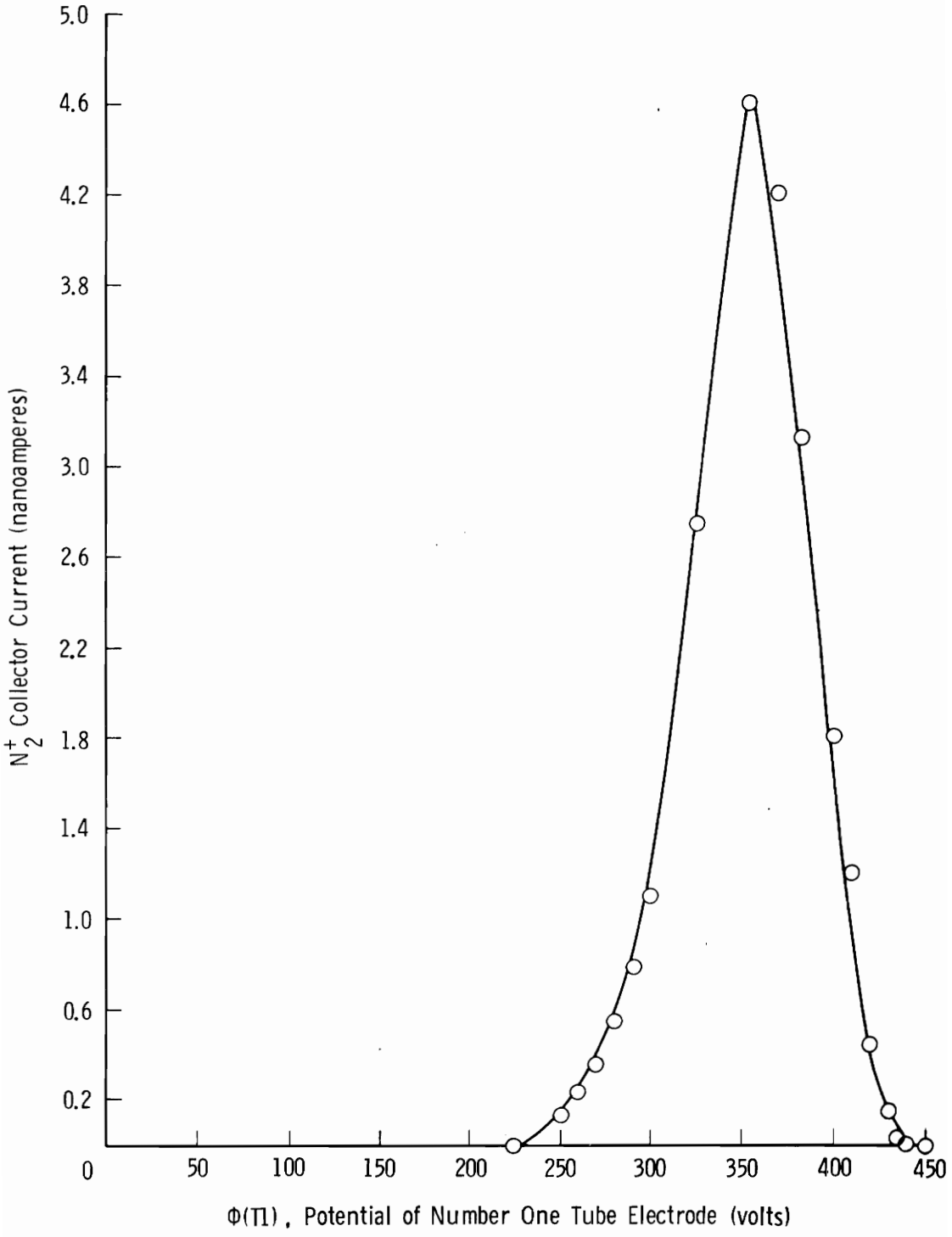

Figure 21.- N_2^+ Ion-Beam Current versus Φ(T1).

it is apparent that the beam has a spacial width. (Recall that element R/D has a deflection plate character.) From Figure 21 it is shown that the output of T1 is a focused beam. This data served as a reference for setting operational potentials for optics section 1 when detecting the ion beam at other positions.

IV.F: ION-OPTICS SECTION 2

The second section of the ion optics was used to transport and focus the ion beam into and through the charge-transfer cell. This section is composed of the 7 elements shown in Figure 22: Tube two (T2), lens two (L2), tube three (T3), and the focusing and deflection electrodes (FD1-FD4). Elements T2 and T3 are cylindrically shaped and have identical dimensions: 0.5 inch in length with entrance and exit aperture diameter of 0.375 inch. L2 is 0.125-inch thick with an aperture diameter of 0.375 inch.

The focusing characteristics of this section was improved by adding a 50 x 50 tungsten grid mesh, 0.001-inch-diameter wire (92% transparency). The grid was placed at L2 where it provides a plane of constant voltage between tubes two and three. The set of elements T2, L2, and T3 has the appearance of an Einzel lens, except in an Einzel lens operation, the potentials of T2 and T3 would have the same magnitude and polarity such that the ions would enter and exit at the same potential. The three elements are operated as a cylindrical lens where there is a convergent or divergent force field in the two halves of the lens.

Electrodes 10 through 13 provide a means of setting an average center line potential for the ion beam at this location and to provide a beam deflection capability in a horizontal and vertical plane to enhance beam alignment into the entrance aperture of CTC. In operation, a maximum beam current was obtained by adjusting two 30KΩ potentiometers (Figure 23). However, when the switches connecting FD1 to FD3 and FD2

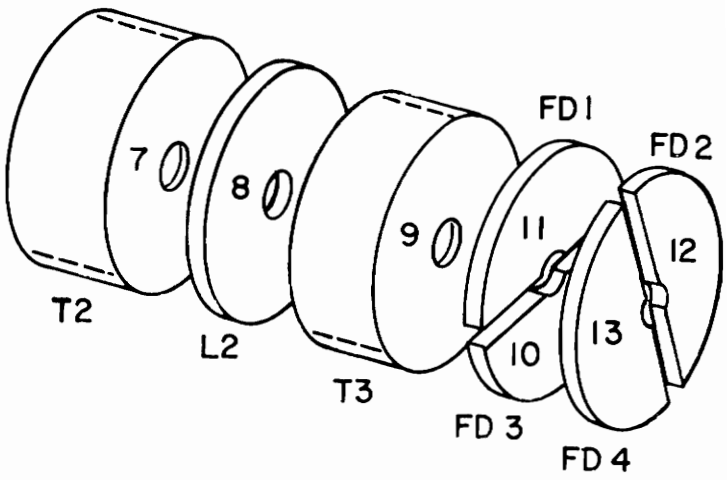

Figure 22.- Ion Optics Section 2.

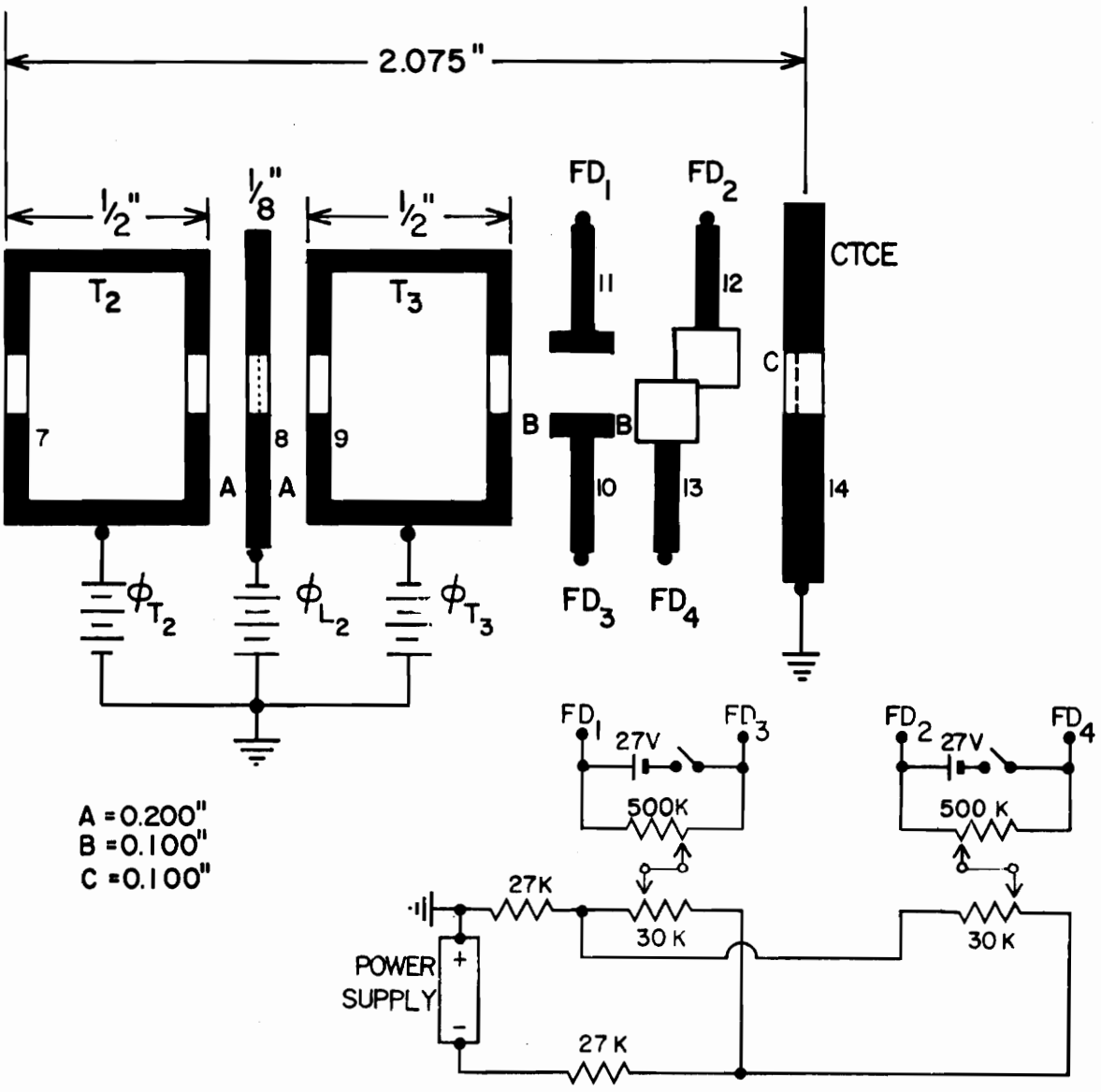

Figure 23.- Wiring of Optics Section 2.

to FD4 were closed, the beam current was always significantly reduced. Adjusting the 500KΩ potentiometer was ineffective and did not appear to have any influence on the beam current magnitude. Because of this, the electronics for the FD electrodes were operated with their switches in the open position.

In order to help support the second section of the ion optics, two 1/4-inch-thick cylindrically shaped teflon pieces were machined for a tight fit over T2 and T3. The teflon pieces have four equally spaced mounting holes drilled on a 1-inch bolt circle for a slip fit to the 0.125-inch-diameter ceramic rods. Similar holes were drilled in L2 and all four electrodes of the focus-deflection (FD) pieces. Each element was stacked on ceramic rods in sequence with ceramic spacers over the ceramic rods of the dimensions A, B, and C shown in Figure 23. The stacked elements are held together with a metal lock ring that locks over the ceramic rods. Elements 7 through 13 are supported from the charge-transfer-cell enclosure (CTCE) plate using three 4-40 nylon screws through clearance holes drilled through L2, the teflon material about T3, all four FD electrodes and into threaded holes in the CTCE plate. The only function of the CTCE plate was to serve as a mounting support for section two elements; it was maintained at ground potential with a center hole of 0.375-inch diameter, across which a piece of tungsten screen wire mesh was placed to maintain a ground plane. This plate was rigidly mounted to the metal enclosure of the charge transfer cell.

All of the elements of ion-optics section are wired to ceramic-to-metal feedthroughs on a 2-3/4-inch vacuum flange with copper wires covered with ceramic-bead insulation.

IV.G: THE CHARGE-TRANSFER CELL

The charge-transfer cell section is shown in Figure 24 and consists of four elements mounted within a charge-transfer-cell enclosure (CTCE). These are beam flag one (BF1), the charge-transfer cell (CTC), the charge-transfer-cell screen (CTCS), and beam flag two (BF2). Beam flag one is a movable element positioned at the entrance to the charge transfer cell; it helps collimate the ion beam into CTC. A thin-edged circular hole, 0.062-inch diameter in BF1 insures that all beam current passing through BF1 enters CTC. The entrance aperture of the CTC is also thin-edged and is 0.093 inch in diameter. For this application, it was important that the aperture diameter in BF1 be smaller than the entrance aperture diameter of CTC to insure that none of the incoming ion beam is collected on the entrance aperture of CTC. This constraint also requires that the spacing between BF1 and CTC be as small as possible (about 0.125") without making electrical contact. The entrance and exit aperture of CTC were machined from copper and are held between special knife-edged flanges by six 8-32 316 S.S. screws. The charge-transfer cell is supported with a tubulated ceramic-to-metal seal from CTCS. This tubulated seal serves to electrically isolate the cell and screen elements; it also serves as the charge-transfer gas inlet port. CTCS was made with 50 x 50 tungsten wire mesh, which was tack welded to circular end rings. The end rings were 0.2-inch thick, 0.455-inch diameter, and had a central through hole of 0.400-inch diameter. The circular end rings have three equally spaced holes drilled to a diameter

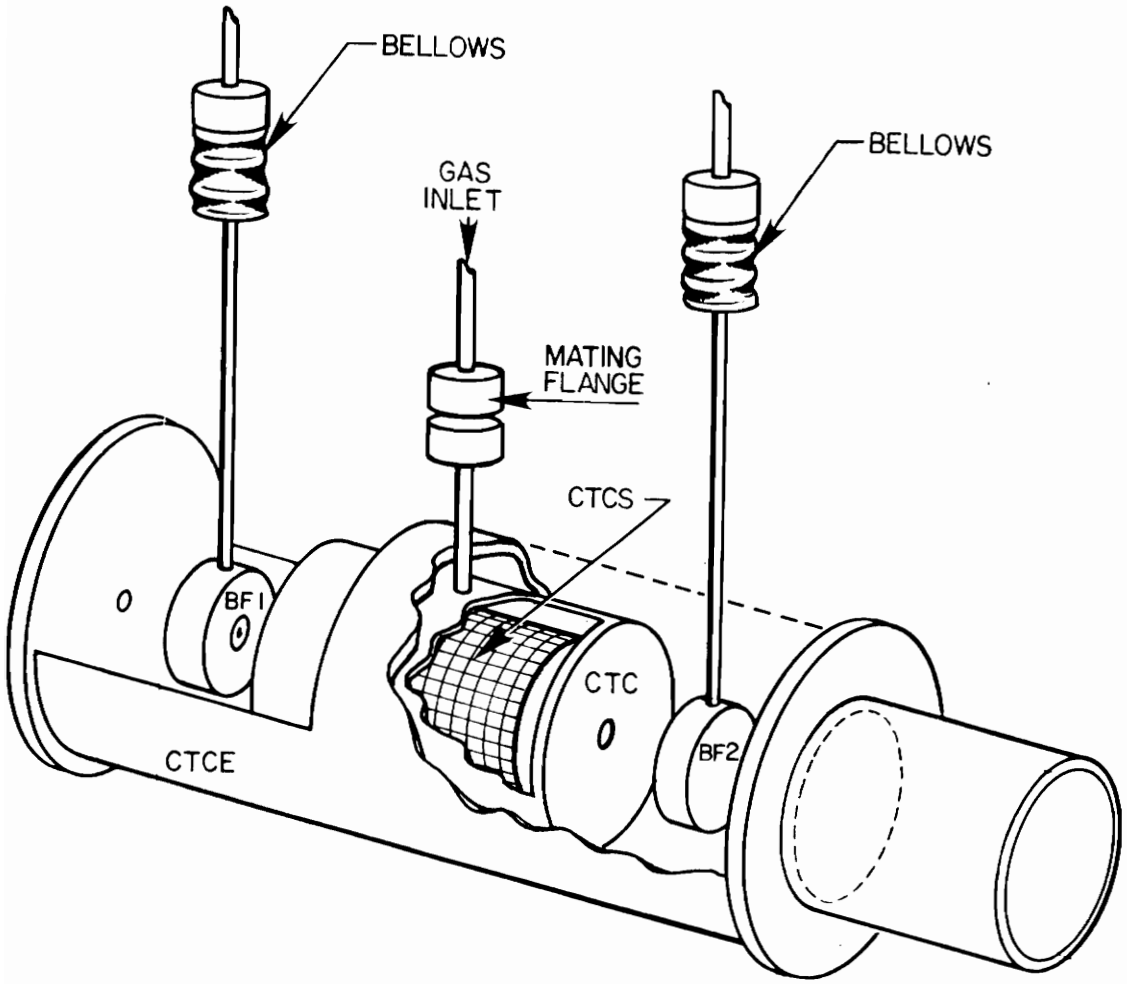

Figure 24.- The Charge-Transfer-Cell Section.

of 0.110 inch. These holes are used for mounting CTCS with 0.125 diameter sapphire balls placed in each hole to electrically insulate the CTCS from the charge-transfer cell while holding the CTCS symmetrically in place. The CTCS wire mesh is reinforced lengthwise with three thin pieces of stainless steel strips 0.05-inch wide, equally spaced and tack welded to the screen wire and end rings.

The charge-transfer-cell screen is used to collect the slow ions made by charge exchange. The charge transfer cell, itself, is used to collect those primary ions scattered through angles sufficiently large that they pass through the screen. It is known that charge exchange produces ions with low kinetic energies[87,88] directed essentially perpendicular to the primary beam.[89] Most of the primary ions that do not undergo charge transfer are scattered through small angles;[90,91] however, the ion beam could be sufficiently defocused at the entrance aperture so that part of the primary beam would be collected at the rear end ring of CTCS and at the exit aperture of CTC. Those primary ions not undergoing charge transfer, scattering or defocusing are collected on the movable beam flag two (BF2) which is also used for aligning the ion beam for maximum transmission through CTC. A poorly aligned ion beam would mean that all of the transmitted ion current would be collected at two places: The exit aperture of CTC and the end ring of CTCS. The potentials on all electrodes were adjusted until a maximum current was obtained on BF2 to insure the best beam transmission.

The ion current measured on CTC, CTCS, and BF2 are critical measurements since they are used to calculate the apparent cross sections.

Because of this, some care was taken in order to eliminate erroneous current readings due to secondary electron emission. Since CTCS is made from high-transparency tungsten grid mesh, most of the high-energy ions will pass through and not collide with it. The potential ($\Delta\phi$) of CTC was varied from +12 to zero volts with respect to CTCS such that any secondary electrons emitted from the surface will be forced to return by the local potential gradient. When the potential difference between CTC and CTCS is zero, the CTC surface area is so much greater than the surface area of CTCS that over 90 percent of any secondary emitted electrons from the surface of CTC would finally be recollected there. Secondary electrons emitted from CTCS by ion bombardment present a potential problem if of sufficient magnitude. When CTCS is negative with respect to CTC the potential fields are such that electrons will be collected on CTC. An electron leaving a surface gives the same current indication as an ion arriving at that surface. Therefore, this effect would tend to increase the magnitude of current measured in the CTC circuit. The electron yield is 0.04 electrons per ion for a 400-electron volt N_2^+ ion bombarding a molybdenum surface.[92] The materials of CTCS are tungsten and 316 stainless steel; secondary emission data does not appear to be available for these materials for bombardment with the N_2^+ ion. The average work functions[93] of molybdenum, tungsten, and iron are 4.27, 4.41, and 4.38 eV, respectively. Since these materials have about the same work function, it is expected that the magnitude of secondary electrons emitted from these surfaces would be about the same. Since the largest elemental

component of stainless steel is iron, this element was used as a reference. Errors due to the emission of secondary electrons would enter by way of the calculation of the current ratio:

$$\frac{I_{CTCS} + 0.04\ I_{CTCS}}{I(o) - 0.04\ I_{CTCS}}$$

For a 441 electron volt N_2^+ ion beam, the current ratio $I_{CTCS}/I(o)$ obtained from experimental data was 0.2. Therefore:

$$\left(\frac{I_{CTCS} + 0.04\ I_{CTCS}}{I_{(o)} - 0.04\ I_{CTCS}} - \frac{I_{CTCS}}{I(o)}\right) < 0.01$$

Secondary emission may introduce an error in the current ratio of less than 5 percent and is well within the margin of error expected for this type of experiment.

It has been reported that the intensity of the continuous portion of the secondary emission spectrum under ion bombardment is proportional to the atomic number Z of the target material.[94] Since the atomic number for carbon is small relative to the refractory metals, secondary emission could be significantly less for the graphite electrode used for BF2. For this reason, BF2 was made from POCO[95] graphite. After considering the problem of secondary electrons at BF2, it was decided that this was not a serious problem; they are either recollected on BF2 or collected on CTC. Since these currents are used in data calculation as a sum, the total current would not change.

In order to obtain data for charge transfer cross sections as a function of ion energy, it was necessary to operate the charge transfer apparatus above ground potential. By applying a potential ϕ_{CTC} (Figure 1) to the charge transfer apparatus, the incoming ion beam is retarded to a potential that is equal to the difference between the ion acceleration potential ϕ_{IAV} and ϕ_{CTC}. The ion energy potential ϕ_{IE} is thus given by:

$$\phi_{IE} = \phi_{IAV} - \phi_{CTC}$$

Leakage currents are usually a problem when measuring currents smaller than 10^{-9} A, as is expected for charge transfer experiments. Leakage-current problems were encountered, but were eliminated by connecting the ceramic bead insulated lead wires from CTCS and CTC to a coaxial glass-to-metal seal that was mounted to a 2-3/4-inch vacuum flange using vacuum epoxy. Currents to these circuits were measured using Keithly model 602 electrometers with an off-ground operating capability of 1500 volts. These electrometers have triaxial inputs: high, low, and ground. Operating with the high terminal connected to a charge collecting electrode, and the low terminal connected to some reference voltage above ground, and using coaxial feedthroughs, the problem of leakage current was eliminated. In this mode of operation the high and low terminal are at the same potential except for millivolts, across the input terminal. Leakage currents between the high and low terminal is less than 10^{-13} amperes. Currents to BF2 were also measured using a

floatable electrometer; however, leakage currents did not present a problem at this electrode because it was suspended inside the vacuum system without making contact with other insulators at high potentials.

IV.H: CHARGE-TRANSFER GAS PRESSURE

The pressure in CTC must be known very accurately because the calculation of the charge transfer cross section is inversely proportional to this pressure. Several pressure sensing devices have been used: Ionization gages, McLeod gages, and capacitance manometers. Each of these devices requires connection to CTC through a somewhat restricted tubulation. There is an inherent error associated with this method because of the conductance of the connecting tubing that is usually not considered. Uncertainty errors are also associated with pressure sensors operated in the CTC pressure range of 10^{-5}-10^{-4} torr. As an example, a connecting tube of 1/4-inch diameter and 6 inches long has a conductance of approximately 0.21 liters/sec for N_2. An indicated pressure of 10^{-4} torr at the pressure sensor would then correspond to a pressure of 0.3×10^{-4} torr in CTC, where the CTC aperture conductance has been taken to be the calculated values of 1.47 liters/sec. If the conductance of the connecting tubing was not taken into consideration, it would represent an error of 70 percent! This problem was eliminated by using a porous plug leak method similar to the method described in Section IV.D. above.

Figure 3 shows the connection of the porous metal leak to the CTC and the capacitance manometer used as a pressure sensor on the high pressure side of the leak. With this arrangement the capacitance manometer is operated at pressures of 10-100 torr where the accuracy is better than 0.03 percent. Figure 25 shows the calibration data for

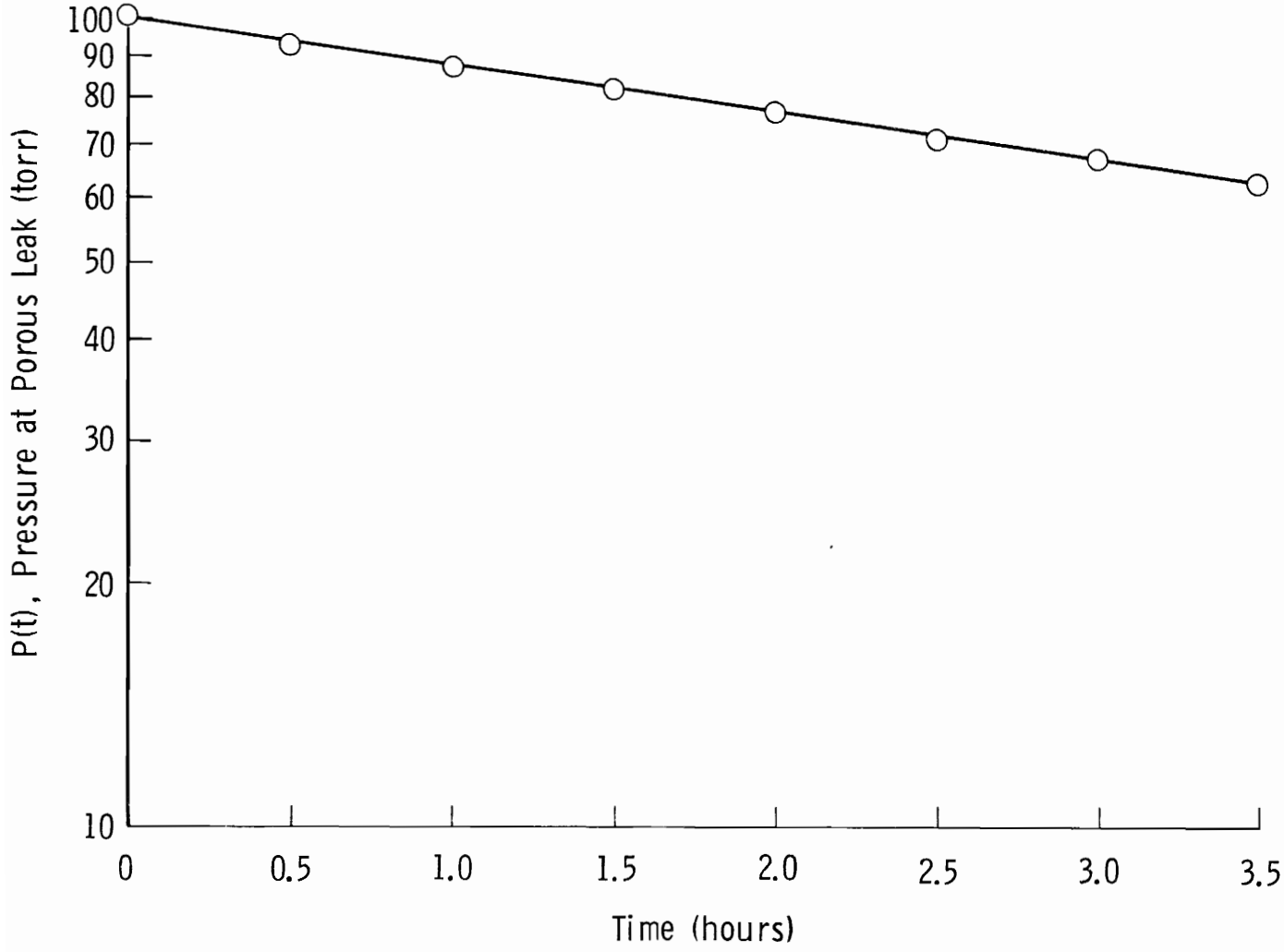

Figure 25.- Porous Plug Conductance Data.

the porous metal plug from which the conductance was determined to be 9.74×10^{-6} liters/sec, for N_2 at ambient temperature.

The test gas pressure can now be monitored through the porous metal leak gas inlet system of known conductance. The entrance and exit aperture of CTC are of the "sharp-edge" type, machined with precision from OFHC copper.[96] Since the apertures of CTC are the ideal sharp edge type, their conductance is readily calculable.

The CTC and the porous metal inlet are connected by a vacuum tight bellows and flange arrangement, such that the pressure in the CTC is known at any time from the following relation

$$P_{pp} C_{pp} = C_{CTC} P_{CTC} \tag{29}$$

P_{pp} is the pressure on the high pressure side of the metal leak and is monitored at all times. C_{pp} and C_{CTC} are the conductances of the porous metal leak and charge transfer cell apertures, respectively. P_{CTC} is the pressure inside CTC, its value is needed for making charge transfer cross section calculations obtained from equation (24).

V: RESULTS AND DISCUSSIONS

V.A: PRELIMINARY EXPERIMENTS

To determine overall system performance, a number of preliminary experiments were run and cross sections were determined. These preliminary studies were made on the following symmetric charge-exchange systems:

$$N_2^+ + N_2 \longrightarrow$$
$$O_2^+ + O_2 \longrightarrow$$
$$CO^+ + CO \longrightarrow$$

From the results of the preliminary experiments, it soon became evident that a number of experimental artifacts were affecting the results. The principal problems were:

1. The appearance of serious leakage currents at the major electrodes in the charge-transfer measurement.
2. Experimental cross sections showed a dependence on the magnitude of the potential $\Delta\phi$ between the charge transfer cell and the CTCS. See Figure 26.
3. An apparent dependence on the pressure of the neutral charge-transfer gas was observed in measured cross sections. See Figure 27.

The problem of leakage currents was solved by the use of coaxial feedthroughs, as was discussed in Section IV.G. The dependence of observed cross sections on $\Delta\phi$ and P_{CTC} were more serious and required

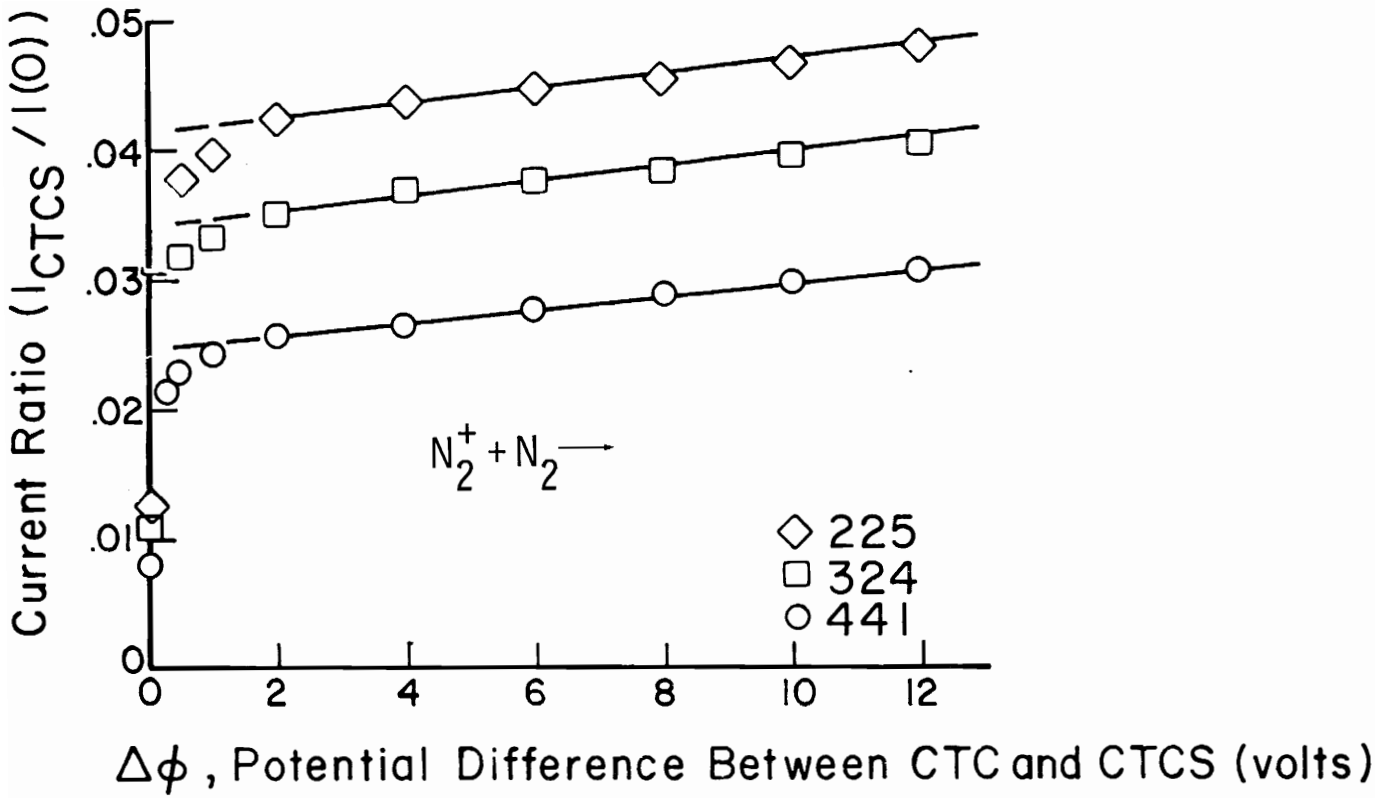

Figure 26.- Preliminary Data for $I_{CTCS}/I(0)$ versus $\Delta\Phi$.

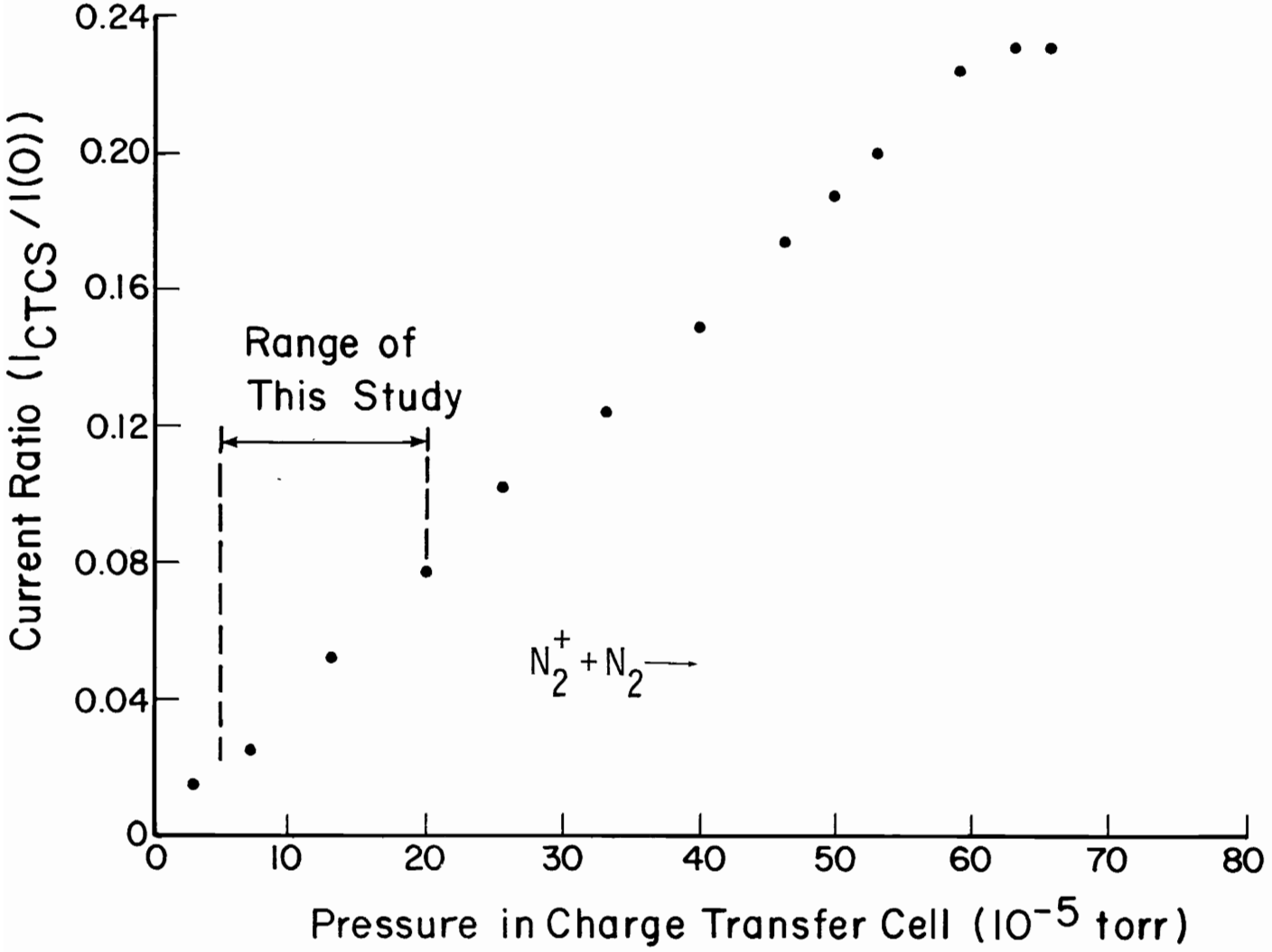

Figure 27.- Preliminary Data for $I_{CTCS}/I(0)$ versus P_{CTC}.

an in-depth study of our method for treating the data. This, in turn, led to changes in the experimental procedures used.

In effect, it is known that the charge transfer cross section is a function of the relative velocity of collision partners, and so of ϕ_{IE}; it is also a function of the internal state of the ion, and so is a function of ϕ_{EE}. Thus,

$$\sigma_{true} = \sigma\left(\phi_{EE}, \phi_{IE}\right) .$$

But in the preliminary experiments, it was found that

$$\sigma_{observed} = \sigma\left(\phi_{EE}, \phi_{IE}, P_{CTC}, \Delta\phi\right) .$$

The problem was, how does one extract σ_{true} from data for $\sigma_{observed}$? An approach to this problem is discussed in the next section.

V.B: EXTRAPOLATION TECHNIQUES

We have noted that experimental values of the current ratio $I_{CTCS}/I(o)$ show a dependence on the value of the voltage $\Delta\phi$. Since the current ratios are used in the calculations of charge-transfer cross sections, observed cross sections will also have a $\Delta\phi$ dependence. By plotting the current ratio $I_{CTCS}/I(o)$ as a function of $\Delta\phi$ from 0 to 12 volts, one obtains a curve that is essentially flat from 2 to 12 volts and increases in a nonlinear fashion from 0 to 2 volts. (Figure 28) The flat portion of the curve gives the finite current ratio which we will refer to as $\left.\frac{I_{CTCS}}{I(o)}\right|_{\infty}$. The corresponding measured value of the current ratio at $\Delta\phi = 0$ is referred to as $I_{CTCS}/I(o)\Big|_{o}$.

If we can interpret the quantities $\left.\frac{I_{CTCS}}{I(o)}\right|_{o}$ and $\left.\frac{I_{CTCS}}{I(o)}\right|_{\infty}$ on the plots of $\frac{I_{CTCS}}{I(o)}$ versus $\Delta\phi$, then we can extract the charge-transfer current ratio $I_{CT}/I(o)$. Focus our attention on feature $\left.\frac{I_{CTCS}}{I(o)}\right|_{o}$ (the experimental current ratio in the limit $\Delta\phi = 0$). When there are no electric fields within the charge-transfer cell, i.e., when $\Delta\phi = 0$, the currents collected on the CTC and the CTCS are determined by the relative areas of these elements, as seen by the ions. For the purposes of discussion, we can divide the ion currents to the CTC and CTCS into two components: Fast ions from the primary beam which impinge on both the CTC and CTCS, and slow ions which are the products of charge transfer. For the slow ions the areas of the CTCS and CTC are in the ratio of about 10:90 (based on the CTCS transparency).

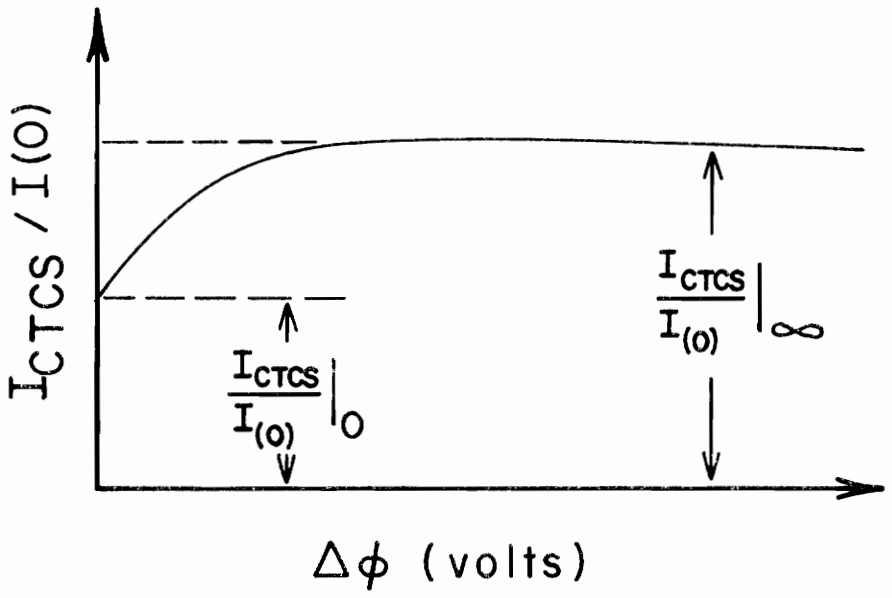

Figure 28.- Experimental Behavior of $I_{CTCS}/I(0)$ versus $\Delta\Phi$.

(For Actual Data, See Table III)

Therefore, about 11 percent of the slow ions will be collected at CTCS when $\Delta\phi = 0$.

Since the fast ions approach the CTCS at near grazing incidence, the effective transparency of the CTCS is much reduced for these ions. Simple geometry indicates that this transparency is less than 57 percent. Thus, when $\Delta\phi = 0$, 43 percent of the fast ions impinging on the CTCS will be collected. Since the magnitude of the slow ion current is much less than that of the fast ion current, and since at $\Delta\phi = 0$, this inequality is enhanced by the geometric character of the collection process, we can consider the current ratio $\left.\frac{I_{CTCS}}{I(o)}\right|_o$ to represent essentially only fast ions.

In the final data given below the ion current ratio $I_{CTCS}/I(o)$ varied with the value of $\Delta\phi$ as shown schematically in Figure 28. When $\Delta\phi$ is large, essentially all slow ions are collected as shown by the saturation in the growth of $I_{CTCS}/I(o)$ as a function of $\Delta\phi$. This is interpreted to mean that the collection of fast ions is not affected by the relatively small magnitudes of $\Delta\phi$ used in this study. Then, in the limit of large $\Delta\phi$ (about 12 volts), the current ratio $\left.I_{CTCS}/I(o)\right|_\infty$ is the sum of all the slow ions collected plus a fast ion contribution.

$$\left.\frac{I_{CTCS}}{I(o)}\right|_\infty = \frac{I_{CT}}{I(o)} + \frac{I_{fast}}{I(o)} \qquad (30)$$

But from the preceding discussion we note that

$$\frac{I_{fast}}{I(o)} = \frac{I_{CTCS}}{I(o)}\Bigg|_{o} \tag{31}$$

Therefore, from equations (30) and (31), we find:

$$\frac{I_{CT}}{I(o)} = \frac{I_{CTCS}}{I(o)}\Bigg|_{\infty} - \frac{I_{CTCS}}{I(o)}\Bigg|_{o} \tag{32}$$

We should note that it is appropriate to refer our current ratio measurements to the limit $\Delta\phi = 0$. From Figure 1, we see that

$$\phi_{IE} = \phi_{IAV} - \phi_{CTC} + \Delta\phi \tag{33}$$

where ϕ_{IAV} is the ion acceleration voltage (the potential of the mass spectrometer ion source above ground). In the data, the quantity $\phi_{IAV}-\phi_{CTC}$ was recorded as the nominal ion-energy potential.

All cross sections reported in this work were calculated with equation (33). With the above result, the expression for the cross section becomes

$$\sigma = -\frac{kT}{P_{CTC}x}\,\ell n\left(1 + \frac{I_{CTCS}}{I(o)}\Bigg|_{o} - \frac{I_{CTCS}}{I(o)}\Bigg|_{\infty}\right) \tag{34}$$

where T, x, and P_{CTC} are the absolute temperature, length, and neutral target gas pressure, respectively, and k is the Boltzmann constant.

The above discussion indicates how to eliminate the effects of

the $\Delta\phi$ dependence on observed cross sections. It remains to consider the effects of any apparent dependence of observed cross sections on P_{CTC}.

Our preliminary data exhibits an apparent weak pressure dependence in going from the lowest to highest pressures tested. There is a change in the slope of current ratio versus P_{CTC} plots as is seen in Figure 27. To eliminate those errors in the cross section due to scatter in data taken at different pressures or due to the complicating effects at high pressures, the following procedures were introduced. First we chose to run experiments in the low-pressure range where linearity of the current ratio $I_{CTCS}/I(o)$ with pressure can be accepted. Data was therefore taken in the range from 9.9 to 20 x 10^{-5} torr (which is only a small fraction of the pressure scale shown in Figure 27).

Second, an extrapolation technique was employed to remove the apparent pressure effects due to scatter. Equation (34) used for the calculation of charge-transfer cross sections was modified to the following form:

$$\sigma = -\frac{kT}{x} \lim_{P_{CTC} \to o} \left[\frac{d}{dP} \ell n \left(1 + \frac{I_{CTCS}}{I(o)}\bigg|_{o} - \frac{I_{CTCS}}{I(o)}\bigg|_{\infty} \right) \right] \qquad (35)$$

The derivative indicated in this equation can be evaluated from the slope of the graph $-\ell n\left(1 + \frac{I_{CTCS}}{I(o)}\Big|_{o} - \frac{I_{CTCS}}{I(o)}\Big|_{\infty}\right)$ vs. P_{CTC} in the vicinity of $P_{CTC} = 0$. All of the cross sections reported in Section V.D., below, were computed according to the prescription given in equation (35).

V.C: CALIBRATION OF THE ELECTRON ENERGY SCALE

In order to account for uncertainties in the applied electron ionization energy, a vanishing current measurement of the appearance potential for the N_2^+ ion was performed. This experiment was conducted at two locations in the ion beam: At the mass spectrometer's normal collector position, and at the charge-transfer-cell position. In both cases it was observed that applied electron energy at the threshold of ionization did not correspond to the known appearance potential [23] of 15.63 $\pm$ 0.02 eV. Since we planned to examine cross sections as a function of electron energy, it became important to get a calibration of the error between the normally applied electron energy and the true electron energy required to produce the ground state and first two excited states of N_2^+. The error in the electron energy scale was such that the applied voltage $\phi(App)_{EE}$ indicated a value less than the threshold for ionization. The analogy was made that

$$\phi(App)_{EE} + \Delta\phi(OS) = \phi(True)_{EE} \qquad (36)$$

where $\Delta\phi(OS)$ would be an offset error in the applied electron energy and $\phi(True)_{EE}$ represents the true electron energy. From our vanishing current measurements we saw what appeared to be threshold ionization to the ground state ion at about 7.5 electron volts. This implies then, that there is an off-set error in the applied electron energy of about 8.1 electron volts. The vanishing current plot for N_2^+ at the CTC position is shown in Figure 29. There are some phenomena

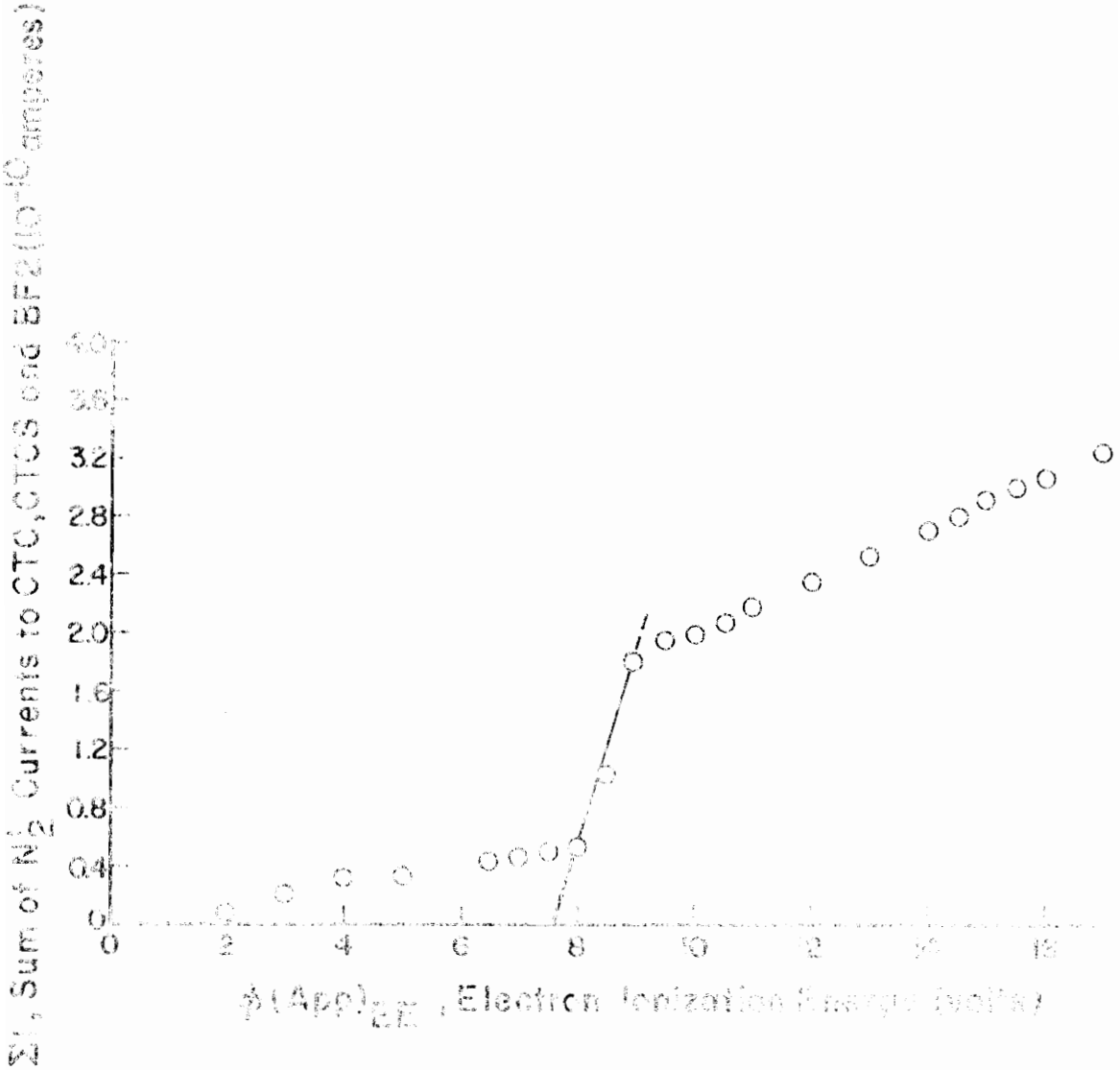

Figure 29. - Vanishing Current Measurement of N_2^+ Ion Current at Mass Spectrometer versus $\Phi(App)_{EE}$.

occurring such that the vanishing current data does not show a definite drop to zero ion current at a finite electron energy. There is a long tail as the applied electron energy is reduced to the vicinity of 2 eV. Since we were collecting current at the CTC for the data shown in Figure 29, other vanishing current data were needed to see if the ion optics focusing elements were causing this phenomena. We then performed a vanishing current experiment with the ion collector at its original position in the mass spectrometer. The results of this data are shown in Figure 30. We see from this data that the essential characteristics of this plot are very similar to those of Figure 29.

For example, there is an analogous long tail as the electron energy potential is decreased toward zero. This data implies then, that the pre-appearance potential structure of Figure 29 is an artifact of the mass spectrometer ion source and is not created by the ion optics elements.

In the data presented in Section V.D, the appearance potentials have been corrected for the observed 8.1 eV offset.

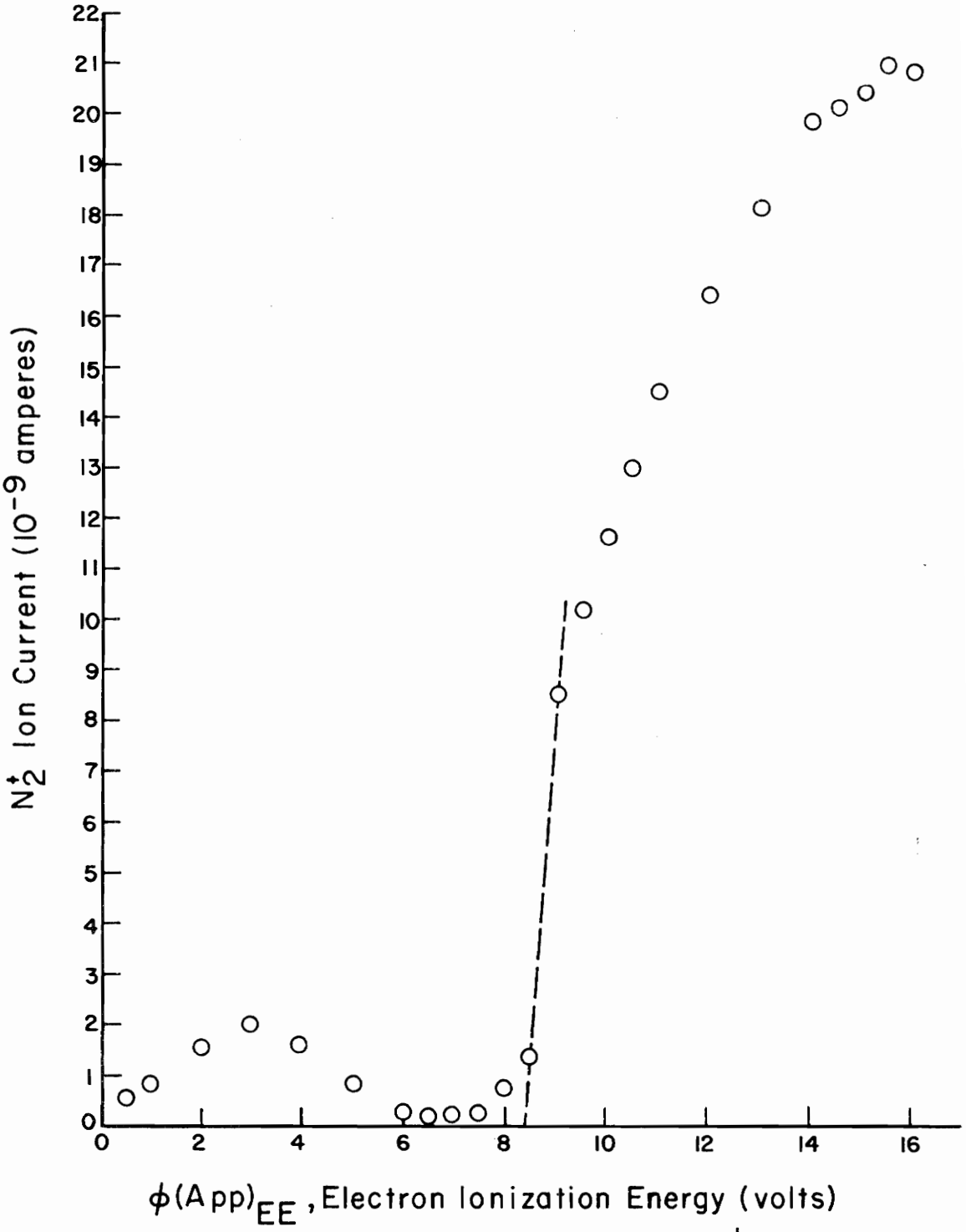

Figure 30.- Vanishing Current Measurement of N_2^+ Ion Current at Mass Spectrometer versus $\Phi(App)_{EE}$.

V.D: DATA AND RESULTS

Data were collected for eight values of electron energy, for seven values of ion energy, four values of charge-transfer gas pressure, and for 12 values of $\Delta\phi$. In the measurements the total ion beam current to the CTC, I(o), was calculated as a sum of three currents:

$$I(o) = I_{CTCS} + I_{CTC} + I_{BF2} \tag{37}$$

In Table III, the experimental results for $\frac{I_{CTCS}}{I(o)}$ are given for the ranges of corrected electron energy, ion energy and neutral charge transfer gas (N_2) pressure.

In Table IV, the experimental results are presented after the corrections for the $\Delta\phi$ dependence have been applied. The function $\ell n\left(1 - \frac{I_{CT}}{I(o)}\right)$ is tabulated for the ranges of corrected electron energy, ion energy, and neutral charge-transfer-gas (N_2) pressure.

In Table V, the final experimental results are tabulated which represents our determination of the charge transfer cross sections as a function of ion energy and electron energy. The cross section values were obtained by plotting the function $-\ell n(1 - 1_{CT}/I(o))$ versus P_{CTC}, for eight values of electron energy and seven values of ion energy. All the cross sections shown were obtained from the following relation:

$$\sigma = \frac{kT}{1330x} \cdot \text{Slope} \tag{38}$$

where k is Boltzmann's constant. The cross sections were calculated

TABLE III

EXPERIMENTAL DATA (UNEXTRAPOLATED)

TABLE III. EXPERIMENTAL DATA (UNEXTRAPOLATED)

Corrected Electron Energy (eV)	Ion Energy (eV)	P_{CTC} (10^{-5} torr)	$I_{CTCS}/I(o)$ For the Tabulated Values of $\Delta\phi$ in Volts								
			0	0.1	0.3	0.5	1	4	8	10	12
11.6	9	9.9	0.152	0.153	0.156	0.159	0.176	0.186	0.195	0.196	0.196
	36		0.162	0.164	0.166	0.169	0.184	0.192	0.195	9.195	0.196
	81		0.169	0.169	0.172	0.175	0.193	0.197	0.198	0.198	0.200
	144		0.164	0.164	0.164	0.169	0.191	0.198	0.198	0.198	0.198
	225		0.117	0.178	0.178	0.183	0.206	0.215	0.218	0.218	0.218
	324		0.222	0.224	0.227	0.230	0.257	0.269	0.275	0.276	0.278
	441		0.155	0.157	0.159	0.163	0.189	0.202	0.206	0.207	0.207
13.1	9		0.112	0.112	0.114	0.118	0.128	0.151	0.155	0.157	0.157
	36		0.084	0.084	0.086	0.095	0.112	0.117	0.117	0.117	0.117
	81		0.051	0.079	0.055	0.065	0.079	0.083	0.085	0.085	0.085
	144		0.083	0.084	0.086	0.094	0.114	0.121	0.123	0.125	0.125
	225		0.132	0.135	0.137	0.139	0.169	0.180	0.180	0.181	0.181
	324		0.099	0.101	0.105	0.113	0.139	0.152	0.155	0.155	0.155

TABLE III. Continued

Corrected Electron Energy (eV)	Ion Energy (eV)	P_{CTC} (10^{-5} torr)	$I_{CTS}/I(o)$ For the Tabulated Values of $\Delta\phi$ in Volts								
			0	0.1	0.3	0.5	1	4	8	10	12
13.1	441	9.9	0.084	0.086	0.092	0.103	0.129	0.141	0.142	0.143	0.143
15.1	9		0.120	0.121	0.123	0.126	0.140	0.149	0.158	0.160	0.161
	36		0.147	0.147	0.150	0.155	0.180	0.188	0.194	0.195	0.195
	81		0.145	0.155	0.165	0.170	0.175	0.181	0.185	0.188	0.190
	144		0.149	0.155	0.160	0.165	0.178	0.194	0.196	0.198	0.200
	225		0.154	0.160	0.165	0.175	0.185	0.200	0.203	0.205	0.207
	324		0.150	0.165	0.170	0.175	0.185	0.195	0.205	0.210	0.215
	441		0.154	0.175	0.180	0.185	0.190	0.205	0.215	0.220	0.225
11.6	9	13.3	0.107	0.125	0.133	0.140	0.150	0.166	0.171	0.173	0.175
	36		0.105	0.120	0.130	0.145	0.150	0.168	0.172	0.173	0.175
	81		0.125	0.135	0.145	0.160	0.170	0.183	0.189	0.192	9.195
	144		0.099	0.118	0.125	0.135	0.150	0.165	0.168	0.170	0.172
	225		0.158	0.167	0.175	0.185	0.205	0.224	0.230	0.235	0.238

TABLE III. Continued

Corrected Electron Energy (eV)	Ion Energy (eV)	P_{CTC} (10^{-5} torr)	$I_{CTCS}/I(o)$ For the Tabulated Values of $\Delta\phi$ in Volts								
			0	0.1	0.3	0.5	1	4	8	10	12
11.6	324	13.3	0.144	0.165	0.175	0.188	0.196	0.214	0.223	0.260	0.300
	441		0.148	0.165	0.175	0.185	0.198	0.209	0.212	0.213	0.215
13.1	9		0.165	0.175	0.180	0.194	0.208	0.221	0.224	0.225	0.226
	36		0.165	0.175	0.180	0.190	0.208	0.225	0.227	0.228	0.230
	81		0.150	0.167	0.175	0.185	0.200	0.208	0.210	0.213	0.216
	144		0.144	0.155	0.165	0.180	0.198	0.210	0.215	0.218	0.220
	225		0.150	0.165	0.170	0.180	0.200	0.213	0.215	0.216	0.217
	324		0.170	0.183	0.190	0.205	0.217	0.233	0.237	0.240	0.243
	441		0.163	0.175	0.185	0.205	0.215	0.227	0.230	0.232	0.234
15.1	9		0.160	0.172	0.180	0.188	0.205	0.215	0.218	0.219	0.220
	36		0.138	0.155	0.170	0.180	0.190	0.205	0.213	0.216	0.220
	81		0.137	0.165	0.170	0.178	0.188	0.197	0.198	0.199	0.200
	144		0.158	0.175	0.185	0.195	0.213	0.220	0.225	0.226	0.228

TABLE III. Continued

Corrected Electron Energy (eV)	Ion Energy (eV)	P_{CTC} (10^{-5} torr)	$I_{CTCS}/I(o)$ For the Tabulated Values of $\Delta\phi$ in Volts								
			0	0.1	0.3	0.5	1	4	8	10	12
15.1	225	13.3	0.151	0.170	0.185	0.193	0.207	0.222	0.228	0.230	0.233
	324		0.151	0.170	0.185	0.193	0.205	0.222	0.229	0.233	0.237
	441		0.156	0.173	0.185	0.195	0.213	0.226	0.232	0.235	0.238
11.6	9	16.6	0.094	0.120	0.130	0.137	0.145	0.163	0.167	0.168	0.170
	36		0.090	0.115	0.115	0.130	0.140	0.150	0.166	0.169	0.170
	81		0.092	0.115	0.125	0.135	0.150	0.163	0.168	0.170	0.173
	144		0.089	0.115	0.125	0.135	0.150	0.163	0.167	0.168	0.170
	225		0.120	0.145	0.160	0.170	0.180	0.191	0.195	0.196	0.198
	324		0.140	0.165	0.175	0.185	0.200	0.218	0.223	0.225	0.228
	441		0.149	0.175	0.185	0.200	0.215	0.234	0.240	0.244	0.246
13.1	9		0.127	0.155	0.160	0.180	0.187	0.200	0.205	0.207	0.210
	36		0.142	0.170	0.180	0.195	0.205	0.217	0.223	0.226	0.228
	81		0.145	0.160	0.175	0.190	0.210	0.220	0.223	0.225	0.227

TABLE III. Continued

Corrected Electron Energy (eV)	Ion Energy (eV)	P_{CTC} (10^{-5} torr)	$I_{CTCS}/I(o)$ For the Tabulated Values of $\Delta\phi$ in Volts								
			0	0.1	0.3	0.5	1	4	8	10	12
13.1	144	16.6	0.140	0.165	0.170	0.185	0.203	0.215	0.217	0.219	0.220
	225		0.139	0.165	0.180	0.185	0.200	0.214	0.217	0.218	0.220
	324		0.162	0.180	0.190	0.205	0.220	0.232	0.235	0.231	0.237
	441		0.140	0.165	0.175	0.190	0.205	0.218	0.225	0.227	0.230
15.1	9		0.124	0.130	0.140	0.150	0.175	0.195	0.203	0.206	0.209
	36		0.077	0.160	0.170	0.175	0.185	0.201	0.205	0.207	0.210
	81		0.104	0.140	0.145	0.150	0.164	0.180	0.185	0.187	0.190
	144		0.112	0.135	0.150	0.165	0.175	0.192	0.200	0.202	0.205
	225		0.142	0.160	0.175	0.190	0.200	0.217	0.225	0.227	0.230
	324		0.137	0.160	0.180	0.190	0.200	0.217	0.225	0.230	0.235
	441		0.114	0.140	0.160	0.170	0.180	0.196	0.200	0.202	0.205
11.6	9	19.9	0.075	0.078	0.085	0.105	0.132	0.144	0.145	0.144	0.144
	36		0.075	0.076	0.083	0.105	0.116	0.149	0.149	0.149	0.149

TABLE III. Continued

Corrected Electron Energy (eV)	Ion Energy (eV)	P_{CTC} (10^{-5} torr)	$I_{CTCS}/I(o)$ For the Tabulated Values of $\Delta\phi$ in Volts								
			0	0.1	0.3	0.5	1	4	8	10	12
11.6	81	19.9	0.092	0.092	0.100	0.119	0.155	0.169	0.173	0.173	0.173
	144		0.076	0.078	0.083	0.104	0.136	0.151	0.153	0.153	0.153
	225		0.237	0.237	0.239	0.247	0.303	0.326	0.329	0.331	0.331
	324		0.211	0.213	0.219	0.229	0.282	0.318	0.327	0.329	0.331
	441		0.118	0.120	0.130	0.152	0.202	0.218	0.224	0.225	0.223
13.1	9		0.139	0.142	0.146	0.161	0.199	0.224	0.224	0.224	0.225
	36		0.140	0.140	0.148	0.160	0.198	0.217	0.225	0.225	0.228
	81		0.133	0.134	0.139	0.153	0.204	0.215	0.219	0.219	0.217
	144		0.126	0.129	0.132	0.147	0.196	0.214	0.218	0.217	0.219
	225		0.125	0.127	0.132	0.148	0.203	0.221	0.224	0.224	0.224
	324		0.190	0.192	9.196	0.202	0.243	0.302	0.306	0.308	0.310
	441		0.141	0.145	0.153	0.164	0.207	0.254	0.260	0.261	0.262
15.1	9		0.128	0.129	0.132	0.136	0.173	0.198	0.204	0.204	0.207

TABLE III. Continued

Corrected Electron Energy (eV)	Ion Energy (eV)	P_{CTC} (10^{-5} torr)	$I_{CTCS}/I(o)$ For the Tabulated Values of $\Delta\phi$ in Volts								
			0	0.1	0.3	0.5	1	4	8	10	12
15.1	36	19.9	0.100	0.100	0.105	0.110	0.153	0.171	0.173	0.173	0.174
	81		0.097	0.097	0.099	0.105	0.150	0.172	0.172	0.174	0.174
	144		0.094	0.096	0.098	0.105	0.154	0.175	0.181	0.181	0.181
	225		0.146	0.147	0.149	0.154	0.181	0.243	0.248	0.251	0.252
	324		0.114	0.119	0.123	0.128	0.172	0.218	0.223	0.224	0.225
	441		0.098	0.099	0.105	0.117	0.163	0.206	0.210	0.212	0.213
24.1	9	9.9	0.170	0.174	0.178	0.184	0.198	0.215	0.220	0.220	0.219
	36		0.056	0.058	0.636	0.072	0.072	0.072	0.102	0.103	0.105
	81		0.065	0.065	0.071	0.080	0.093	0.115	0.114	0.115	0.113
	144		0.147	0.152	0.160	0.167	0.178	0.189	0.193	0.193	0.194
	225		0.167	0.173	0.181	0.194	0.204	0.196	0.198	0.193	0.193
	324		0.069	0.073	0.084	0.097	0.108	0.115	0.117	0.117	0.117
	441		0.067	0.075	0.088	0.102	0.113	0.118	0.120	0.120	0.122

TABLE III. Continued

Corrected Electron Energy (eV)	Ion Energy (eV)	P_{CTC} (10^{-5} torr)	$I_{CTCS}/I(o)$ For the Tabulated Values of $\Delta\phi$ in Volts								
			0	0.1	0.3	0.5	1	4	8	10	12
26.1	9	9.9	0.211	0.212	0.215	0.224	0.245	0.275	0.306	0.316	0.321
	36		0.162	0.165	0.174	0.182	0.194	0.203	0.207	0.208	0.212
	81		0.153	0.156	0.165	0.176	0.189	0.201	0.209	0.208	0.212
	144		0.154	0.154	0.161	0.174	0.190	0.200	0.205	0.205	0.207
	225		0.151	0.155	0.163	0.174	0.192	0.203	0.204	0.206	0.208
	324		0.135	0.136	0.143	0.155	0.176	0.186	0.187	0.187	0.187
	441		0.098	0.103	0.113	0.124	0.143	0.153	0.156	0.154	0.153
28.1	9		0.151	0.156	0.159	0.159	0.170	0.218	0.242	0.244	0.244
	36		0.166	0.169	0.176	0.184	0.191	0.194	0.199	0.212	0.214
	81		0.157	0.160	0.169	0.179	0.190	0.199	0.205	0.207	0.208
	144		0.156	0.158	0.169	0.183	0.198	0.205	0.201	0.197	0.198
	235		0.158	0.160	0.171	0.184	0.200	0.209	0.211	0.210	0.210
	324		0.116	0.119	0.131	0.146	0.161	0.169	0.170	0.171	0.170

TABLE III. Continued

Corrected Electron Energy (eV)	Ion Energy (eV)	P_{CTC} (10^{-5} torr)	$I_{CTCS}/I(o)$ For the Tabulated Values of $\Delta\phi$ in Volts								
			0	0.1	0.3	0.5	1	4	8	10	12
28.1	441	9.9	0.125	0.132	0.145	0.158	0.169	0.181	0.182	0.183	0.183
30.1	9		0.151	0.157	0.161	0.168	0.180	0.188	0.191	0.199	0.201
	36		0.080	0.088	0.093	0.101	0.115	0.126	0.128	0.126	0.127
	81		0.039	0.043	0.048	0.058	0.074	0.085	0.087	0.086	0.087
	144		0.036	0.038	0.045	0.055	0.072	0.082	0.083	0.084	0.084
	225		0.046	0.047	0.054	0.069	0.082	0.090	0.091	0.091	0.091
	324		0.049	0.052	0.063	0.075	0.087	0.094	0.095	0.095	0.095
	441		0.042	0.043	0.058	0.074	0.089	0.094	0.095	0.098	0.098
32.1	9		0.125	0.126	0.128	0.138	0.159	0.172	0.180	0.180	0.180
	36		0.135	0.135	0.136	0.141	0.162	0.167	0.163	0.163	0.162
	81		0.031	0.031	0.033	0.040	0.058	0.067	0.068	0.069	0.069
	144		0.079	0.080	0.083	0.091	0.109	0.117	0.120	0.118	0.118
	225		0.052	0.054	0.067	0.081	0.096	0.104	0.105	0.105	0.106

TABLE III. Continued

Corrected Electron Energy (eV)	Ion Energy (eV)	P_{CTC} (10^{-5} torr)	$I_{CTCS}/I(o)$ For the Tabulated Values of $\Delta\phi$ in Volts								
			0	0.1	0.3	0.5	1	4	8	10	12
32.1	324	9.9	0.045	0.049	0.052	0.076	0.090	0.097	0.098	0.099	0.099
	441		0.079	0.079	0.094	0.110	0.123	0.128	0.128	0.128	0.128
24.1	9	13.3	0.238	0.242	0.247	0.257	0.257	0.378	0.410	0.426	0.432
	36		0.110	0.135	0.141	0.152	0.161	0.171	0.188	0.199	0.205
	81		0.236	0.245	0.257	0.278	0.290	0.299	0.298	0.298	0.300
	144		0.172	0.180	0.197	0.208	0.222	0.227	0.235	0.235	0.238
	225		0.199	0.202	0.218	0.235	0.254	0.263	0.265	0.267	0.267
	324		0.146	0.148	0.173	0.194	0.207	0.215	0.215	0.215	0.219
	441		0.119	0.127	0.156	0.172	0.184	0.192	0.195	0.195	0.197
26.1	9		0.209	0.212	0.218	0.232	0.246	0.336	0.376	0.382	0.385
	36		0.274	0.284	0.303	0.315	0.327	0.338	0.354	0.365	0.373
	81		0.345	0.350	0.362	0.376	0.391	0.405	0.412	0.416	0.420
	144		0.174	0.180	0.197	0.209	0.224	0.234	0.237	0.238	0.239

TABLE III. Continued

Corrected Electron Energy (eV)	Ion Energy (eV)	P_{CTC} (10^{-5} torr)	$I_{CTCS}/I(o)$ For the Tabulated Values of $\Delta\phi$ in Volts								
			0	0.1	0.3	0.5	1	4	8	10	12
26.1	225	13.3	0.183	0.190	0.208	0.223	0.234	0.244	0.244	0.243	0.244
	324		0.143	0.152	0.174	0.189	0.199	0.210	0.212	0.213	0.214
	441		0.126	0.137	0.162	0.179	0.186	0.194	0.198	0.200	0.201
28.1	9		0.179	0.186	0.194	0.199	0.210	0.253	0.280	0.289	0.293
	36		0.083	0.088	0.099	0.102	0.109	0.114	0.125	0.129	0.135
	81		0.110	0.114	0.125	0.135	0.146	0.154	0.154	0.154	0.154
	144		0.119	0.126	0.138	0.148	0.158	0.166	0.168	0.170	0.173
	225		0.132	0.137	0.152	0.164	0.172	0.181	0.183	0.183	0.184
	324		0.125	0.131	0.149	0.161	0.170	0.177	0.180	0.181	0.183
	441		0.128	0.140	0.157	0.169	0.175	0.181	0.183	0.183	0.183
30.1	9		0.277	0.282	0.291	0.304	0.318	0.396	0.425	0.429	0.428
	36		0.095	0.099	0.109	0.117	0.123	0.133	0.137	0.141	0.143
	81		0.108	0.115	0.132	0.156	0.163	0.162	0.163	0.165	0.165

TABLE III. Continued

Corrected Electron Energy (eV)	Ion Energy (eV)	P_{CTC} (10^{-5} torr)	$I_{CTCS}/I(o)$ For the Tabulated Values of $\Delta\phi$ in Volts								
			0	0.1	0.3	0.5	1	4	8	10	12
30.1	144	13.3	0.123	0.214	0.136	0.153	0.174	0.183	0.188	0.186	0.187
	225		0.114	0.124	0.144	0.155	0.161	0.168	0.170	0.170	0.171
	324		0.102	0.112	0.134	0.146	0.153	0.161	0.161	0.164	0.164
	441		0.097	0.110	0.135	0.147	0.155	0.154	0.152	0.152	0.153
32.1	9		0.271	0.275	0.279	0.288	0.312	0.396	0.429	0.439	0.442
	36		0.276	0.277	0.280	0.293	0.317	0.333	0.350	0.357	0.369
	81		0.154	0.157	0.167	0.179	0.197	0.212	0.224	0.233	0.239
	144		0.155	0.159	0.171	0.186	0.205	0.213	0.215	0.219	0.219
	225		0.134	0.139	0.150	0.168	0.185	0.196	0.203	0.199	0.203
	324		0.091	0.098	0.109	0.127	0.150	0.160	0.163	0.163	0.165
	441		0.079	0.085	0.105	0.122	0.140	0.149	0.153	0.154	0.155
24.1	9	16.6	0.237	0.238	0.252	0.262	0.271	0.351	0.381	0.391	0.401
	36		0.106	0.135	0.141	0.145	0.151	0.185	0.195	0.200	0.210

TABLE III. Continued

Corrected Electron Energy (eV)	Ion Energy (eV)	P_{CTC} (10^{-5} torr)	$I_{CTCS}/I(o)$ For the Tabulated Values of $\Delta\phi$ in Volts								
			0	0.1	0.3	0.5	1	4	8	10	12
24.1	81	16.6	0.214	0.220	0.230	0.240	0.250	0.285	0.300	0.313	0.320
	144		0.152	0.160	0.175	0.190	0.210	0.227	0.234	0.237	0.240
	225		0.139	0.155	0.165	0.180	0.197	0.215	0.227	0.232	0.237
	324		0.122	0.160	0.167	0.173	0.187	0.200	0.217	0.220	0.225
	441		0.104	0.120	0.145	0.160	0.175	0.185	0.200	0.207	0.215
26.1	9		0.220	0.240	0.255	0.260	0.280	0.355	0.390	0.410	0.430
	36		0.271	0.282	0.290	0.295	0.320	0.350	0.370	0.384	0.391
	81		0.239	0.265	0.295	0.320	0.350	0.380	0.395	0.405	0.415
	144		0.147	0.170	0.190	0.205	0.210	0.227	0.240	0.245	0.250
	225		0.152	0.185	0.200	0.210	0.220	0.228	0.235	0.240	0.245
	324		0.119	0.145	0.165	0.175	0.183	0.194	0.200	0.205	0.210
	441		0.107	0.140	0.160	0.165	0.170	0.185	0.195	0.200	0.205
28.1	9		0.152	0.180	0.190	0.210	0.240	0.280	0.300	0.310	0.320

TABLE III. Continued

Corrected Electron Energy (eV)	Ion Energy (eV)	P_{CTC} (10^{-5} torr)	$I_{CTCS}/I(o)$ For the Tabulated Values of $\Delta\phi$ in Volts								
			0	0.1	0.3	0.5	1	4	8	10	12
28.1	36	16.6	0.045	0.065	0.085	0.090	0.100	0.117	0.122	0.125	0.130
	81		0.087	0.100	0.110	0.118	0.130	0.155	0.165	0.167	0.170
	144		0.097	0.115	0.130	0.134	0.144	0.172	0.178	0.183	0.187
	225		0.106	0.120	0.133	0.145	0.155	0.170	0.178	0.182	0.185
	324		0.109	0.130	0.135	0.145	0.150	0.182	0.188	0.192	0.195
	441		0.107	0.120	0.130	0.150	0.165	0.178	0.182	0.185	0.187
30.1	9		0.275	0.290	0.300	0.315	0.335	0.385	0.405	0.415	0.422
	36		0.079	0.105	0.115	0.123	0.140	0.150	0.152	0.155	0.157
	81		0.092	0.110	0.120	0.135	0.145	0.165	0.171	0.175	0.177
	144		0.104	0.117	0.125	0.140	0.155	0.173	0.180	0.184	0.187
	225		0.105	0.120	0.130	0.145	0.157	0.173	0.177	0.180	0.183
	324		0.084	0.100	0.113	0.125	0.140	0.160	0.168	0.172	0.177
	441		0.095	0.115	0.125	0.140	0.148	0.167	0.172	0.175	0.178

TABLE III. Continued

Corrected Electron Energy (eV)	Ion Energy (eV)	P_{CTC} (10^{-5} torr)	$I_{CTCS}/I(o)$ For the Tabulated Values of $\Delta\phi$ in Volts								
			0	0.1	0.3	0.5	1	4	8	10	12
32.1	9	16.6	0.227	0.245	0.250	0.260	0.280	0.360	0.381	0.395	0.402
	36		0.272	0.290	0.300	0.315	0.330	0.358	0.375	0.382	0.392
	81		0.124	0.135	0.140	0.150	0.167	0.198	0.203	0.212	0.125
	144		0.125	0.135	0.140	0.150	0.165	0.188	0.204	0.206	0.208
	225		0.120	0.140	0.150	0.165	0.180	0.197	0.207	0.212	0.215
	324		0.095	0.115	0.125	0.135	0.155	0.171	0.180	0.185	0.190
	441		0.080	0.110	0.115	0.125	0.140	0.160	0.168	0.171	0.175
24.1	9	19.9	0.164	0.165	0.178	0.195	0.215	0.259	0.256	0.260	0.258
	36		0.107	0.108	0.110	0.125	0.155	0.175	0.178	0.181	0.185
	81		0.131	0.132	0.142	0.158	0.193	0.213	0.216	0.216	0.216
	144		0.224	0.228	0.242	0.263	0.296	0.316	0.321	0.323	0.328
	225		0.104	0.105	0.127	0.150	0.170	0.183	0.187	0.186	0.186
	324		0.096	0.102	0.129	0.155	0.174	0.184	0.187	0.188	0.188

TABLE III. Continued

Corrected Electron Energy (eV)	Ion Energy (eV)	P_{CTC} (10^{-5} torr)	$I_{CTCS}/I(o)$ For the Tabulated Values of $\Delta\phi$ in Volts								
			0	0.1	0.3	0.5	1	4	8	10	12
24.1	441	19.9	0.084	0.093	0.125	0.154	0.167	0.178	0.178	0.179	0.179
26.1	9		0.263	0.268	0.282	0.300	0.326	0.404	0.438	0.449	0.453
	36		0.159	0.162	0.175	0.186	0.213	0.234	0.242	0.246	0.247
	81		0.133	0.138	0.151	0.167	0.193	0.210	0.213	0.215	0.216
	144		0.154	0.160	0.177	0.190	0.224	0.242	0.238	0.239	0.241
	225		0.108	0.113	0.136	0.158	0.175	0.185	0.189	0.189	0.189
	324		0.112	0.118	0.146	0.171	0.189	0.201	0.204	0.204	0.203
	441		0.095	0.106	0.139	0.166	0.181	0.189	0.192	0.193	0.193
28.1	9		0.199	0.201	0.213	0.228	0.250	0.272	0.289	0.296	0.297
	36		0.107	0.113	0.130	0.145	0.167	0.183	0.185	0.187	0.186
	81		0.103	0.109	0.117	0.131	0.172	0.186	0.190	0.191	0.191
	144		0.085	0.091	0.096	0.101	0.155	0.166	0.176	0.177	0.177
	225		0.216	0.225	0.246	0.271	0.281	0.290	0.292	0.292	0.293

TABLE III. Continued

Corrected Electron Energy (eV)	Ion Energy (eV)	P_{CTC} (10^{-5} torr)	$I_{CTCS}/I(o)$ For the Tabulated Values of $\Delta\phi$ in Volts								
			0	0.1	0.3	0.5	1	4	8	10	12
28.1	324	1919	0.247	0.262	0.295	0.318	0.331	0.345	0.355	0.350	0.355
	441		0.230	0.250	0.282	0.302	0.312	0.324	0.331	0.334	0.336
30.1	9		0.196	0.206	0.226	0.244	0.257	0.284	0.311	0.320	0.322
	36		0.105	0.115	0.133	0.148	0.165	0.181	0.183	0.184	0.187
	81		0.084	0.086	0.097	0.118	0.140	0.156	0.158	0.158	0.158
	144		0.052	0.069	0.080	0.096	0.116	0.126	0.129	0.131	0.130
	225		0.081	0.094	0.121	0.138	0.150	0.158	0.161	0.160	0.163
	324		0.099	0.107	0.136	0.159	0.176	0.178	0.180	0.184	0.189
	441		0.109	0.122	0.153	0.178	0.190	0.198	0.202	0.203	0.202
32.1	9		0.157	0.158	0.175	0.194	0.217	0.234	0.247	0.249	0.249
	36		0.096	0.101	0.121	0.142	0.166	0.183	0.188	0.189	0.189
	81		0.118	0.124	0.145	0.168	0.191	0.206	0.209	0.209	0.209
	144		0.069	0.075	0.075	0.083	0.134	0.160	0.162	0.164	0.165

TABLE III. Continued

Corrected Electron Energy (eV)	Ion Energy (eV)	P_{CTC} (10^{-5} torr)	$I_{CTCS}/I(o)$ For the Tabulated Values of $\Delta\phi$ in Volts								
			0	0.1	0.3	0.5	1	4	8	10	12
32.1	225	19.9	0.117	0.118	0.126	0.141	0.186	0.207	0.217	0.219	0.221
	324		0.114	0.116	0.125	0.146	0.187	0.203	0.203	0.201	0.201
	441		0.133	0.135	0.152	0.171	0.212	0.224	0.222	0.226	0.227

TABLE IV

EXPERIMENTAL DATA (CORRECTED FOR $\Delta\phi$ DEPENDENCE)

TABLE IV. EXPERIMENTAL DATA (CORRECTED FOR $\Delta\phi$ DEPENDENCE)

Corrected Electron Energy (eV)	Ion Energy (eV)	P_{CTC} (10^{-5} torr)	$\ln(1 - \frac{I_{CT}}{I(o)})$
11.6	9	9.9	-0.0449
	36		-0.0459
	81		-0.0314
	144		-0.0471
	225		-0.0387
	324		-0.0439
	441		-0.0408
13.1	9		-0.0387
	36		-0.0315
	81		-0.0325
	144		-0.0356
	225		-0.0439
	324		-0.0466
	441		-0.0471
15.1	9		-0.0336
	36		-0.0437
	81		-0.0408
	144		-0.0419
	225		-0.0419
	324		-0.0408*

TABLE IV. Continued

Corrected Electron Energy (eV)	Ion Energy (eV)	P_{CTC} (10^{-5} torr)	$\ln(1 - \frac{I_{CT}}{I(o)})$
15.1	441		-0.0419
11.6	9	13.3	-0.0544
	36		-0.0587
	81		-0.0566
	144		-0.0629
	225		-0.0619
	324		-0.0629
	441		-0.0608
13.1	9		-0.0566
	36		-0.0608
	81		-0.0587
	144		-0.0629
	225		-0.0619
	324		-0.0619
	441		-0.0640
15.1	9	13.3	-0.0544
	36		-0.0587
	81		-0.0619
	144		-0.0641
	225		-0.0661

TABLE IV. Continued

Corrected Electron Energy (eV)	Ion Energy (eV)	P_{CTC} (10^{-5} torr)	$\ln(1 - \frac{I_{CT}}{I(o)})$
15.1	324	13.3	-0.0640
	441		-0.0661
11.6	9	16.6	-0.0651
	36		-0.0758
	81		-0.0704
	144		-0.0736
	225		-0.0704
	324		-0.0758
	441		-0.0790
13.1	9		-0.0704
	36		-0.0736
	81		-0.0747
	144		-0.0758
	225		-0.0736
	324		-0.0704
	441		-0.0758
15.1	9	16.6	-0.0650
	36		-0.0704
	81		-0.0683
	144		-0.0578

TABLE IV. Continued

Corrected Electron Energy (eV)	Ion Energy (eV)	P_{CTC} (10^{-5} torr)	$\ln(1 - \frac{I_{CT}}{I(o)})$
15.1	225	16.6	-0.0736
	324		-0.0758
	441		-0.0790
11.6	9	19.9	-0.0704
	36		-0.0726*
	81		-0.0758
	144		-0.0715*
	225		-0.0812
	324		-0.0932
	441		-0.0965
13.1	9		-0.0888
	36		-0.0779
	81		-0.0779
	144		-0.0877
	225		-0.0943
	324		-0.1111
	441		-0.1154
15.1	9	19.9	-0.0693
	36		-0.0672*
	81		-0.0758

TABLE IV. Continued

Corrected Electron Energy (eV)	Ion Energy (eV)	P_{CTC} (10^{-5} torr)	$\ell n(1 - \frac{I_{CT}}{I(o)})$
15.1	144	19.9	-0.0758
	225		-0.0932
	324		-0.1009
	441		-0.1020
24.1	9	9.9	-0.0513
	36		-0.0424
	81		-0.0437
	144		-0.0336
	225		-0.0294
	324		-0.0434
	441		-0.0437
26.1	9		-0.0619*
	36		-0.0439
	81		-0.0429
	144		-0.0419
	225		-0.0449
	324		-0.0460
	441		-0.0513
28.1	9		-0.0619*
	36		-0.0356

TABLE IV. Continued

Corrected Electron Energy (eV)	Ion Energy (eV)	P_{CTC} (10^{-5} torr)	$\ell n(1 - \frac{I_{CT}}{I(o)})$
28.1	81		-0.0439
	144		-0.0449
	225		-0.0429
	324		-0.0449
	441		-0.0460
30.1	9		-0.0513
	36		-0.0408
	81		-0.0439
	144		-0.0447
	225		-0.0429
	324		-0.0439
	441		-0.0449
32.1	9		-0.0566
	36		-0.0439
	81		-0.0387
	144		-0.0402
	225		-0.0471
	324		-0.0419
	441		-0.0460
24.1	9	13.3	-0.0943*

TABLE IV. Continued

Corrected Electron Energy (eV)	Ion Energy (eV)	P_{CTC} (10^{-5} torr)	$\ell n(1 - \frac{I_{CT}}{I(o)})$
24.1	36	13.3	-0.0566
	81		-0.0566
	144		-0.0555
	225		-0.0576
	324		-0.0555
	441		-0.0576
26.1	9		-0.0954
	36		-0.0576
	81		-0.0566
	144		-0.576
	225		-0.0555
	324		-0.0534
	441		-0.0551
28.1	9		-0.0959
	36		-0.0429
	81		-0.0513
	114		-0.0566
	225		-0.0555
	324		-0.0566
	441		-0.0534

TABLE IV. Continued

Corrected Electron Energy (eV)	Ion Energy (eV)	P_{CTC} (10^{-5} torr)	$\ell n(1 - \frac{I_{CT}}{I(o)})$
30.1	9		-0.0998
	36		-0.0513
	81		-0.0513
	144		-0.0534
	225		-0.0523
	324		-0.0545
	441		-0.0539
32.1	9	13.3	-0.1043
	36		-0.0569
	81		-0.0576
	144		-0.0569
	225		-0.0576
	324		-0.0499
	441		-0.0627
24.1	9	16.6	-0.1087
	36		-0.0715
	81		-0.0715
	144		-0.0704
	225		-0.0736
	324		-0.0704

TABLE IV. Continued

Corrected Electron Energy (eV)	Ion Energy (eV)	P_{CTC} (10^{-5} torr)	$\ln(1 - \frac{I_{CT}}{I(o)})$
24.1	441	16.6	-0.0736
26.1	9		-0.1165
	36		-0.0715
	81		-0.0715
	144		-0.0736
	225		-0.0704
	324		-0.0736
	441		-0.0704
28.1	9		-0.1143
	36		-0.0683
	81		-0.0651
	144		-0.0704
	225		-0.0715
	324		-0.0683
	441		-0.0704
30.1	9	16.6	-0.1109
	36		-0.0683
	81		-0.0704
	144		-0.0683
	225		-0.0704

TABLE IV. Continued

Corrected Electron Energy (eV)	Ion Energy (eV)	P_{CTC} (10^{-5} torr)	$\ell n(1 - \frac{I_{CT}}{I(o)})$
30.1	324	16.6	-0.0683
	441		-0.0704
32.1	9		-0.1199*
	36		-0.0704
	81		-0.0683
	144		-0.0715
	225		-0.0726
	324		-0.0704
	441		-0.726
24.1	9	19.9	-0.1054
	36		-0.0651*
	81		-0.0694*
	144		-0.0683
	225		-0.0683
	324		-0.0827
	441		-0.0893
26.1	9		-0.1076
	36		-0.0683
	81		-0.0694

TABLE IV. Continued

Corrected Electron Energy (eV)	Ion Energy (eV)	P_{CTC} (10^{-5} torr)	$\ell n(1 - \frac{I_{CT}}{I(o)})$
26.1	144	19.9	-0.0672
	225		-0.0672
	324		-0.0888
	441		-0.0884
28.1	9		-0.1065
	36		-0.0866
	81		-0.0910
	144		-0.0834
	225		-0.0866
	324		-0.0921
	441		-0.0834
30.1	9		-0.1098
	36		-0.0834
	81		-0.0796
	144		-0.0812
	225		-0.0823
	324		-0.0844
	441		-0.0889
32.1	9		-0.1054

TABLE IV. Continued

Corrected Electron Energy (eV)	Ion Energy (eV)	P_{CTC} (10^{-5} torr)	$\ell n(1 - \frac{I_{CT}}{I(o)})$
32.1	36	19.9	-0.0134
	81		-0.0856
	144		-0.0834
	225		-0.0815
	324		-0.0823
	441		-0.0856

*Data is suspect

TABLE V

CHARGE-TRANSFER CROSS SECTIONS FOR THE N_2^+-N_2 SYSTEM

TABLE V. CHARGE-TRANSFER CROSS SECTIONS FOR THE N_2^+-N_2 SYSTEM

Ion Energy (eV)	Corrected Electron Energy (eV)	σ (10^{-16} cm^2)
9	11.6	24.0
	13.1	24.9
	15.1	22.6
	24.1	33.9
	26.1	38.6
	28.1	40.3
	30.1	36.3
	32.1	39.5
36	11.6	26.5
	13.1	24.5
	15.1	24.3
	24.1	26.4
	26.1	26.0
	28.1	24.1
	30.1	24.5
	32.1	26.0
81	11.6	23.7
	13.1	24.5
	15.1	25.2
	24.1	26.0
	26.1	26.0

TABLE V. Continued

Ion Energy (eV)	Corrected Electron Energy (eV)	σ (10^{-16} cm^2)
81	28.1	25.6
	30.1	24.9
	32.1	25.4
144	11.6	27.4
	13.1	25.6
	15.1	26.0
	24.1	25.4
	26.1	26.4
	28.1	25.6
	30.1	25.0
	32.1	25.4
225	11.6	25.6
	13.1	27.7
	15.1	27.9
	24.1	23.3
	26.1	25.8
	28.1	25.8
	30.1	25.0
	32.1	26.0
324	11.6	27.5
	13.1	27.1

TABLE V. Continued

Ion Energy (eV)	Corrected Electron Energy (eV)	σ (10^{-16} cm^2)
324	15.1	27.3
	24.1	25.4
	26.1	27.0
	28.1	26.2
	30.1	25.0
	32.1	25.0
441	11.6	27.5
	13.1	28.1
	15.1	28.1
	24.1	27.0
	26.1	27.7
	28.1	25.8
	30.1	26.0
	32.1	26.7

for an absolute temperature (ambient) of 295 K and for a charge transfer cell length x of 5.08 cm. The slopes were obtained from plots as shown in Figure 31. A technique of extrapolating to zero pressure was utilized to determine a best fit through the four pressure data points and the origin. This extrapolation technique is implied in the limiting process as given by equation (35). The number 1330 is included in the denominator of equation (38) to convert from torr pressure units to cgs pressure units.

From the data in Table V we see that there is a considerable difference between the average magnitude of cross sections for the 9 eV ion energy and average cross sections obtained for the other ion energies. The behavior of the cross sections at low ion energy (9 eV) show the typical resonant charge transfer structure where the cross sections appear to increase with a decrease in ion energy. Typically this structure has been reported in the literature, where specific control of ion state excitation was not studied. In this work we are reasonably certain that only ground state ions ($X^2\Sigma_g^+$) could have been involved in the charge transfer process at the lower ϕ_{EE} values; because the threshold for the ground state ion is about 15.63 ev.[23,73] We note also that our data show ϕ_{EE} values below the apparent threshold for the N_2^+ ground state ion. From Figure 29 we see an offset error associated with the characteristic operation of the electron impact type ion source. This offset error was taken to be 8.1 eV where the steep slope of the graph is extrapolated to a $\phi(App)_{EE}$ value of 7.5 eV. The assumed relation between $\phi(App)_{EE}$ and $\Delta\phi(OS)$ is given

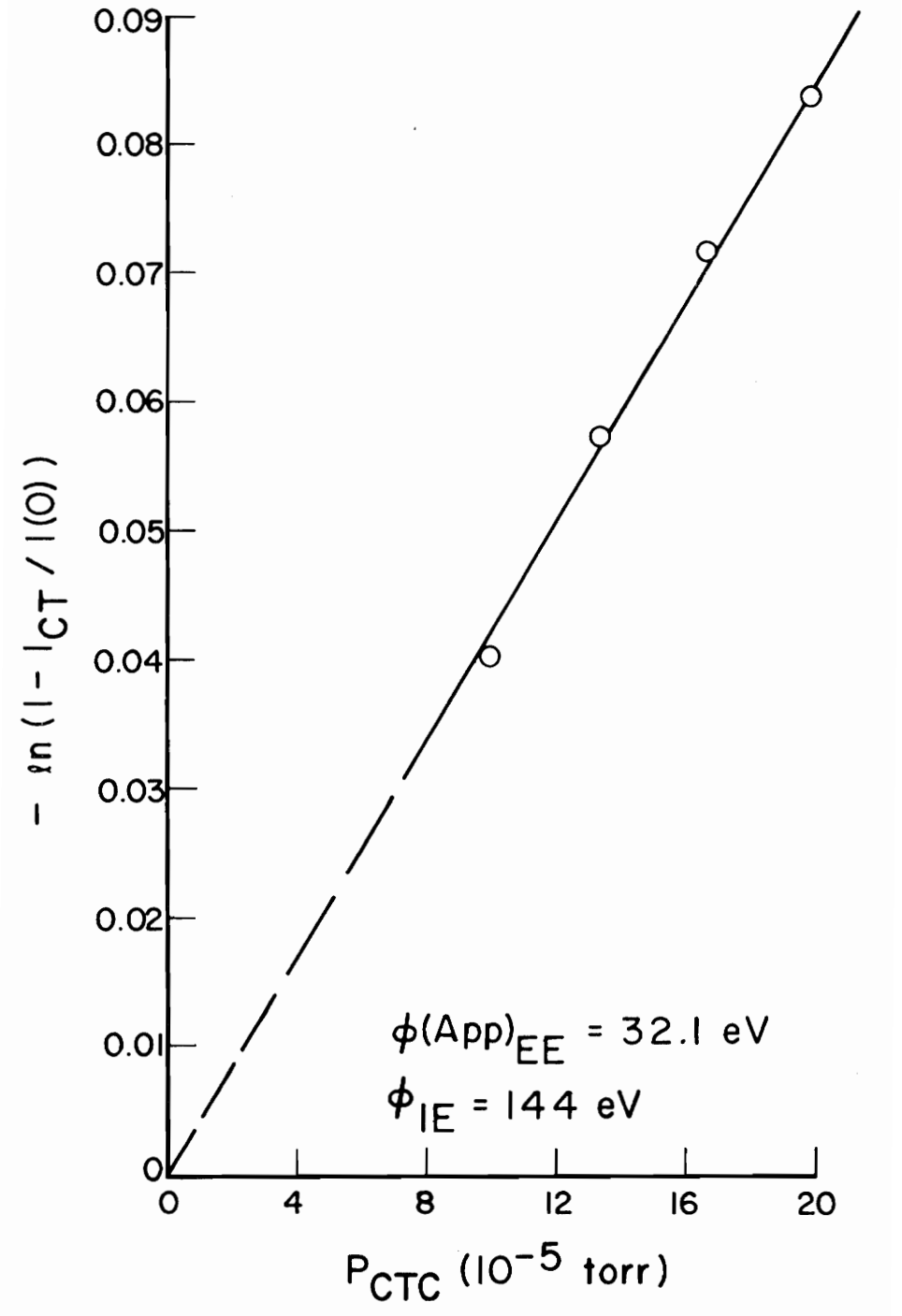

Figure 31.- Plot of - ℓn (1 - $I_{CT}/I(0)$) versus P_{CTC}.

in equation (36). The characteristic long tail[97] shown in the vanishing current measurement of Figure 29 is attributed to nonmonoenergetic electrons being emitted from the hot filament and illustrates the fact that the electrons come off the filament with a distribution of energies.

From the above discussion it is apparent that there is some uncertainty in the assumed values of ϕ_{EE}; however, the low ϕ_{EE} values are separated from the high ϕ_{EE} values by an energy spread of 9 eV. Thus all data reported at low ϕ_{EE} values involve only ground state ions and the data at high ϕ_{EE} values involve some excited state ions ($A^2\pi_4$) whose lifetime is on the order of 12 microseconds; long enough to be involved in the charge transfer process. In this work we have particularly looked for any differences in the structure of the charge transfer curves that could be attributed to ion beam state excitation. A study of our data for both low and high ϕ_{EE}, does not give any supporting evidence that contributions of excited state ions make any significant difference. If there were differences, we did not detect any in this work.

An exact comparison of this work with others could not be made, because in most cases, ϕ_{EE} was not reported. Where ϕ_{EE} has been reported only one value was given. Tabulated results of other investigators are given in Table VI along with the cross sections determined in this work. In Figure 32 we have plotted our data for comparison with the experimental results given in Table VI along with some additional experimental cross sections. Ghosh and Sheridan[98]

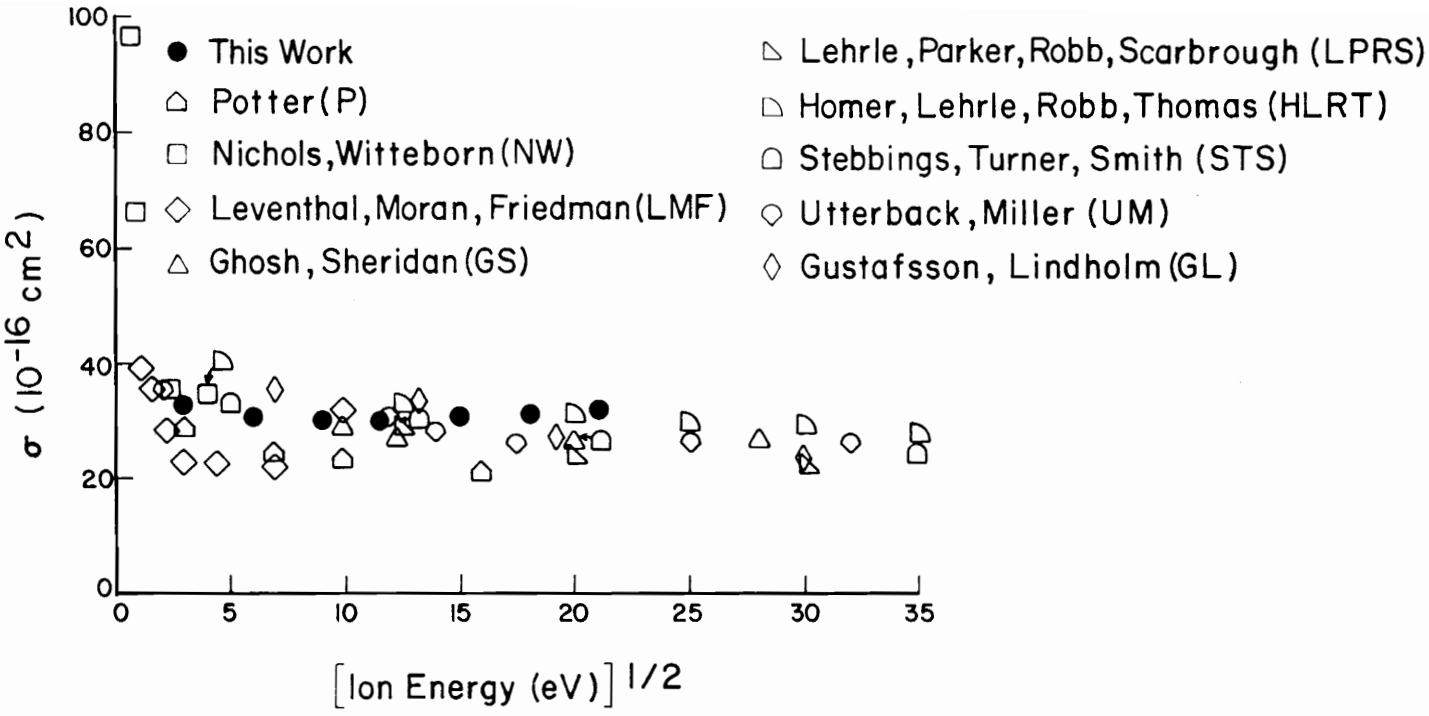

Figure 32.- Comparison σ This Work with Experimental Results of Others.

TABLE VI

COMPARISON OF CHARGE TRANSFER CROSS SECTIONS FOR THE N_2^+-N_2 SYSTEM FROM SEVERAL SOURCES

TABLE VI. COMPARISON OF CHARGE-TRANSFER CROSS SECTIONS FOR THE N_2^+-N_2 SYSTEM FROM SEVERAL SOURCES

Ion Energy (eV)	σ (10^{-16} cm^2) Calculated	σ (10^{-16} cm^2) Experimental	Electron Energy (eV)	Ref.
0.5	-	96.7	95	10
1	39.0	39.1	-	48
6	-	36.9	95	10
9	-	36	75	100
9	-	34.7	95	10
9	-	32.5*	11.1-32.1	This work
10	-	23.1	-	48
17	-	34.8	95	10
20	31.0	22.7	-	48
32	45.4	-	-	49
36	-	25.3*	11.1-32.1	This work
50	26.4	21.7	-	48
81	-	25.2*	11.1-32.1	This work
100	-	26.8	22	1
144	-	25.8*	11.1-32.1	This work
150	-	27	-	98
150	-	30	-	99
150	-	28	200	3
150	-	24	-	4
150	-	28	25	2

TABLE VI. Continued

Ion Energy (eV)	σ (10^{-16} cm^2) Calculated	Experimental	Electron Energy (eV)	Ref.
150	-	33	70	6
156	36.73	-	-	49
225	-	25.9*	11.1-32.1	This work
250	-	21	75	100
324	-	26.3*	11.1-32.1	This work
400	38.7	-	-	49
400	-	26	-	98
400	-	29	50	2
400	-	19	-	4
400	-	24	25	2
400	-	27	-	99
400	-	26	200	3
441	-	27.1*	11.1-32.1	This work
625	-	26	22	1
733	31.38	-	-	49
900	-	26	-	98
900	-	23	-	99
900	-	23	200	3
900	-	29	75	6
900	-	22	25	2
1000	-	26	22	1

TABLE VI. Continued

Ion Energy (eV)	σ (10^{-16} cm^2) Calculated	Experimental	Electron Energy (eV)	Ref.
1175	24.21	-	-	49
1225	-	28	70	6

*Average values

(GS) stated that their data included N_2^+ ions in the ground state when leaving their Heil-type ion source. The pressure in their collision chamber was measured by a Knudsen gage to be 17 x 10^{-5} torr. The electron energy in the ion source of Stebbing, Turner, and Smith[3] (STS) was 200 eV. Nichols and Witeborn[10] (NW) measured cross sections at very low ion energies of less than 17 eV. The electron energy in their ion source was 95 eV, and their reaction chamber was varied between 0.1 to 80 x 10^{-5} torr. Lehrle et.al.[2] (LPRS) studied charge transfer cross sections for a ϕ_{EE} values of 25 eV and collision pressure of 2 x 10 torr, measured by a Bendix gage. Homer, et.al.[6] (HLRT) obtained their data using 70 eV of electron energy and collision pressures not quoted. Gustafsson and Lindholm[99] (GL) data was taken for a collision pressure of 17 x 10^{-5} torr but ϕ_{EE} was not given. Utterback and Miller[1] (UM) used 22 eV electrons in their ion source and the pressure in their collision region was 20 x 10^{-5} torr. Potter[10] (P) claims to have only ground state ions in his incident beam, although this might be doubtful since their ion source was operated at 75 eV. In the experimental results of Levelthal et.al.[48] (LMF) no information was given about ϕ_{EE} or collision chamber pressure.

In Figure 33 a comparison of the present results is made with theoretical calculations of Flannery et.al.[49] and Leventhal et.al.[48] The full multistate treatment and low velocity approximation were calculated by Flannery et.al. using the distribution of vibration levels in the incident ion beam corresponding to an electron excitation energy of 22 eV. Additional calculated cross section data made by

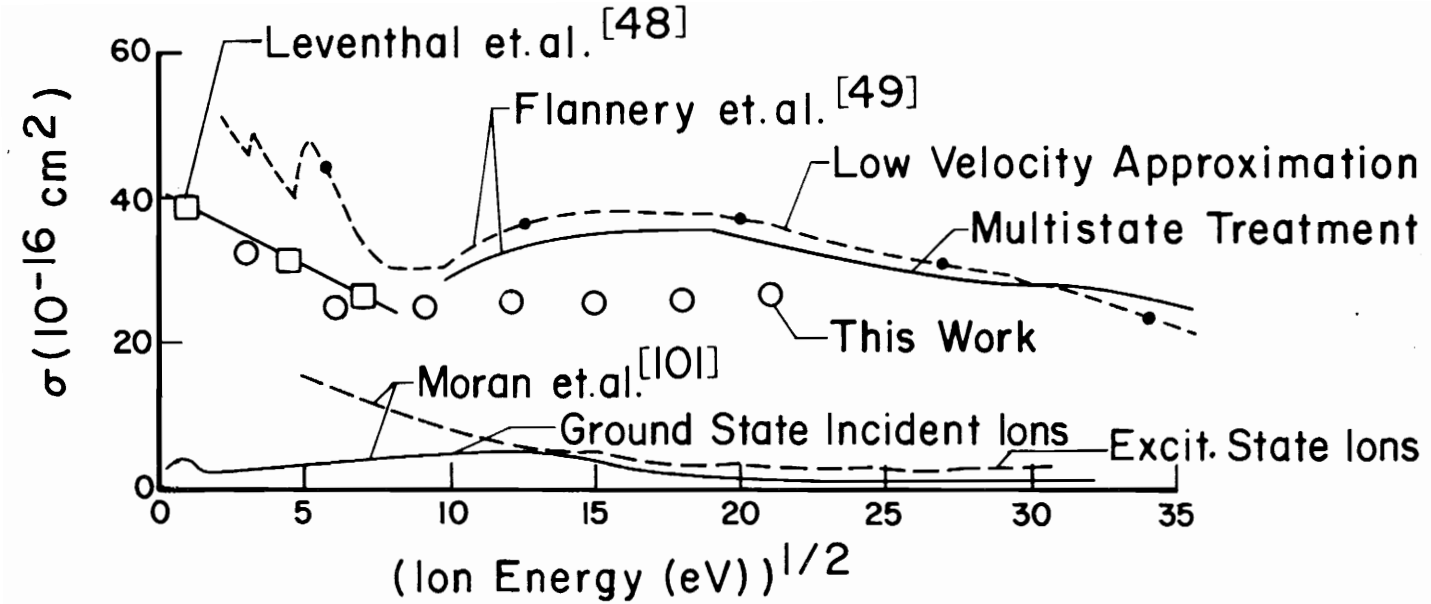

Figure 33.- Comparison σ This Work with Theoretical Calculations of Others.

Leventhal et.al. [48] using the impact parameter method is also shown in Figure 33. The results of Moran et.al. [101] are shown, where they obtained much lower values of cross sections using the multistate impact parameter method [49] to obtain data for individual channels and integral cross sections summed over all product channels. Theoretical cross sections were obtained as a function of the square root of incident ion kinetic energy for nitrogen when both incident ion and target neutrals were in the ground electronic and vibrational state and the resultant product neutrals and ion in vibrational states (ν, ν') equal to (0, 1), (1, 0), and (0, 2) for the total excitation products. Moran et.al. also obtained theoretical cross sections for total vibration excitation with the incident ion in the ground electronic state $N_2^+(X^2\Sigma_g^+)$ and vibrational state 0, 1, 2, 3, with the target neutral in the ground electronic and vibrational state $N_2(X^1\Sigma_g^+, \nu = 0)$ as a function of incident ion kinetic energy. The cross sections obtained were less than 10×10^{-16} cm^2 for incident ion energies larger than about 75 eV.

The cross section data obtained from this work compares favorably with the results of other investigators for the $N_2^+ - N_2$ system. There is reason to believe that a higher level of confidence can be placed in our results since special emphasis were placed on details such as the pressure measuring technique in CTC and calibration of the ϕ_{EE} energy scale to determine when ground state and excited state ions were involved in the charge transfer process. An extrapolation technique was utilized to remove the $\Delta\phi$ dependence of the slow ion collection

scheme. Finally, an extrapolation technique was used to remove any pressure dependence in our results.

VI: CONCLUSIONS

1. Charge-transfer cross sections for the $N_2^+ - N_2$ system did not show any significant dependence on relative ion energy.
2. A systematic study was made to determine the functional dependence of charge transfer on ion beam state excitation. The apparatus was operated in exactly the same mode for the low (11.6 - 15.1 eV) and high (24.1 - 32.1 eV) electron energy data. No observed difference (See Table V) in the cross section structure could be attributed to the ion beam excitation composition. At the higher electron energy a significant portion, 17 percent [80] of the ions could have been in the excited state $A^2\pi_u$ with lifetimes long enough to be involved in the collision process.
3. It is sometimes stated [7] that excited ions in a charge transfer process appear to transfer in a less efficient way. Charge transfer cross sections for excited ions were believed to charge transfer differently, [67] but this has not been confirmed in this work. From our studies we found nothing to claim any differences in the efficiency of charge transfer. There was essentially no difference in the low and high electron energy data.
4. Our final average cross section for the $N_2^+ - N_2$ system compares favorably with the experimental results of other investigators in Table VI and Figure 32. Favorable comparison is also shown with the theoretical calculations of Flannery et.al. and Leventhal et.al. of Figure 33.

VII: LITERATURE CITED

1. Utterback, N. G.; and Miller, G. W.: Rev. Sci. Instr., 32, 1101 (1961).

2. Lehrle, R. S.; Parker, J. R.; Robb, J. C.; and Scarborough, J.: Int. J. Mass Spectrom. Ion Phys., 1, 455 (1968).

3. Stebbings, R. F.; Turner, B. R.; and Smith, A. C. H.: J. Chem. Phys., 38, 2277 (1963).

4. Dillon, J. A.; Sheridan, W. F.; and Edwards, H. D.: J. Chem. Phys., 23, 776 (1955).

5. Stebbings, R. F.; Turner, B. R.; and Rutherford, J.A.: J. Geophys. Res., 71, 771 (1966).

6. Homer, J. B.; Lehrle, R. S.; Robb, J. C.; and Thomas, D. W.: Trans. Faraday Soc., 62, 619 (1966).

7. McDowell, M. R. C., ed.: Atomic Collision Process, pp. 847-853, North-Holland Publishing Company, Amsterdam, 1964.

8. McDowell, M. R. C., ed.: Op. Cit., pp. 854-861.

9. Stebbings, R. F.; Smith, A. C. H.; and Gilbody, H. B.: J. Chem. Phys., 38, 2280 (1963).

10. Nichols, B. J.; and Witteborn, F. C.: NASA Technical Note, D-3265 (1965).

11. Potter, R. F.: J. Chem. Phys., 22, 974 (1954).

12. Flannery, M. R.; Cosby, P. C.; and Moran, T. F.: J. Chem. Phys., 59, 5494 (1973).

13. Leventhal, J. J.; Moran, T. F.; and Friedman, L.: J. Chem. Phys., 46, 4666 (1967).

14. Moran, T. F.; McCann, K. J.; and Flannery, M. R.: J. Chem. Phys., 63, 3857 (1975).

15. Rapp, D.; and Francis, W. E.: J. Chem. Phys., 37, 2631 (1962).

16. Gurnee, E. F.; and Magee, J. L.: J. Chem. Phys., 26, 1237 (1957).

17. Smith, D. L.; and Futrell, J. H.: J. Chem. Phys., 59, 463 (1973).

18. Leventhal, J. J.; and Friedman, L.: J. Chem. Phys., 46, 997 (1967).

19. Dalgarno, A.: Rev. Mod. Phys., 39, 858 (1967).

20. Neimann, H. B.: Rev. Sci. Instrum., 43, 1151 (1972).

21. Turner, B. R.; Rutherford, J. A.; and Stebbings, R. F.: J. Geophys. Res., 71, 4521 (1966).

22. Stebbings, R. F.; Turner, B. R.; and Rutherford, J. A.: J. Geophys. Res., 771 (1966).

23. Kaneko, Y.: J. Phy. Soc. Japan, 16, 1587 (1960).

24. Langevin, P.: Ann. Chim. Phys., 28, 317 (1903).

25. Langevin, P.: Ann. Chim. Phys., 5, 245 (1905).

26. Hasse, H. R.: Phil. Mag., 1, 139 (1926).

27. Loeb, L. B.: Basic Processes of Gaseous Electronics, 2nd Ed., cp. 1, University of California Press, Berkeley, 1960.

28. Hasse, H. R.; and Cook, W. R.: Phil. Mag., 12, 554 (1931).

29. McDaniel, E. W.: Collision Phenomena in Ionized Gases, pp. 65-76, John Wiley and Sons, Inc., New York, N.Y., 1964.

30. Hirschfelder, J. O.; Curtis, C. F.; and Bird, R. B.: Molecular Theory of Gases and Liquids, pp. 22-35, John Wiley and Sons, Inc., New York, N.Y., 1964.

31. Margenau, H.; and Kestner, N. R.: Theory of Intermolecular Forces, Pergamon, New York, N.Y., 1969.

32. Kolker, H. J.; and Karplus, M.: J. Chem. Phys., 29, 2011 (1963).

33. Hirschfelder, J. O.; Curtis, C. F.; and Bird, R. B.: Op. Cit., p. 950.

34. Victor, G. A.; and Dalgarno, A.: J. Chem. Phys., 50, 2535 (1969).

35. Maryott, A. A.; and Buckley, F.: U.S. National Bureau of Standards, Circular 537 (1973).

36. Langhoff, P. W.; Gordon, R. G.; and Karplus, M.: J. Chem. Phys., 55, 2126 (1971)

37. Tyndall, A. M.: Mobility of Positive Ions in Gases, Cambridge at the University Press, Great Britain, 1939.

38. Massey, H. S. W.: Rep. Prog. Phys., 12, 248 (1949).

39. Hasted, J. B.: Proc. Roy. Soc., A205, 421 (1951).

40. Gioumousis, G.; and Stevenson, D. P.: J. Chem. Phys., 29, 294 (1958).

41. McDaniel, E. W.; Cermak, V.; Dalgarno, A.; Ferguson, E. E.; and Friedman, L.: Ion Molecule Reactions, pp. 7-22, John Wiley and Sons, Inc., New York, N.Y., 1970.

42. Theard, L. P.; and Hamill, W. H.: J. Am. Chem. Soc., 84, 1134 (1962).

43. Moran, T. F.; and Hamill, W. H.: J. Chem. Phys., 39, 1413 (1963).

44. Su, T.; and Bowers, M. T.: J. Chem. Phys., 58, 3027 (1973).

45. Su, T.; and Bowers, M. T. Bowers: Int. J. Mass Spectrom. Ion Phys., 17, 309 (1975).

46. McDaniel, E. W.: Op. Cit., pp. 240-244.

47. Gurnee, E. F.; and Magee, J. L.: J. Chem. Phys., 26, 1237 (1957).

48. Leventhal, J. J.; Moran, T. F.; and L. Friedman, J. Chem. Phys., 46, 4666 (1967).

49. Flannery, M. R.; Cosby, P. C.; and Moran, T. F.: J. Chem. Phys., 59, 5494 (1973).

50. Sena, L.: Collisions of Electrons and Ions with Atoms of Gases, in Russian, GTTI, 1948.

51. Firsov, O.: J. Exptl. and Theoret. Phys. (USSR), 21, 1001 (1951).

52. Demkov, I.: Doklady Leningrad Univ., 146, 74 (1952).

53. Dalgarno, A.: Phil. Trans. Roy. Soc., A250, 411 (1958).

54. Iovitsu, I. Popeso; and Ionescu-Pallas, N.: Sov. Phys.-Tech. Phys., 4, 781 (1960).

55. Goldman, F.: Ann. Physik, 10, 460 (1931).

56. Rostagni, A.: Nuovo Cimento, 12, 134 (1935).

57. Wolf, F.: Ann. Phys., 23, 285 (1936).

58. Keene, J. P.: Phil. Mag., 40, 369 (1949).

59. Hasted, J. B.: Proc. Roy. Soc. (London), A205, 421 (1951).

60. Dillon, J. A.: J. Chem. Phys., 23, 776 (1955).

61. Kistemaker, J.: J. Appl. Sci. Res., B5, 337 (1955).

62. Utterback, N. G.; and Miller, G. H.: Rev. Sci. Instr., 32, 1101 (1961).

63. Lehrle, R. S.; Parker, J. E.; Robb, J. C.; and Scarborough, J.: Int. J. Mass Spectrom. Ion Phys., 1, 455 (1968).

64. McDaniel, E. W.: Op. Cit., p. 340.

65. Benderson, B.; and Fite, W. L., eds: Methods of Experimental Physics, Vol. 7, Part A, p. 143, Academic Press, New York, N.Y., 1968.

66. McDaniels, E. W.: Op. Cit., pp. 244-248.

67. Turner, B. R.; Rutherford, J. A.; and Compton, D. M. J.: J. Chem. Phys., 48, 1602 (1968).

68. McGowan, J. W.; and Kerwin, L.: Can. J. Phys., 42, 2086 (1964).

69. McDowell, M. R. C., ed.: Atomic Collision Processes, pp. 847-853, North-Holland Publishing Company, Amsterdam, 1964.

70. Gould, R. F., ed.: Ion-Molecule Reactions in the Gas Phase, pp. 1-19, American Chemical Society, Washington, D.C., 1966.

71. McGowan, J. W.; Clarke, E. M.; Hanson, H. P.; and Stebbings, R. F.: Phys. Rev. Letters, 13, 620 (1964).

72. Schoen, R. L.: J. Chem. Phys., 40, 1830 (1964).

73. Gilmore, F. R.: J. Quant. Spectrosc. Radiat. Transfer, 5, 369 (1965).

74. Desequelles, J.; Dufay, M.; and Poulizac, D. C.: Phys. Letters, 27A, 96 (1968).

75. Hesser, J. E.: J. Chem. Phys., 48, 2518 (1968).

76. Fowler, R. G.; and Holzberlein, T. M.: J. Chem. Phys., 45, 1124 (1966).

77. Jeunehomme, M.: J. Chem. Phys., 44, 267 (1966).

78. Bennet, R. G.; and Dalby, E. W.: J. Chem. Phys., 31, 434 (1959).

79. Anton, A.: Ann der Phys., 18, 178 (1966).

80. Holland, R. F.; and Mair, W. B. II: J. Chem. Phys., 56, 5229 (1972).

81. Hollstein, M.; Lorents, D. C.; Peterson, J. R.; and Sheridan, J. R.: Can. J. Chem., 47, 1858 (1969).

82. Shemansky, D. E.; and Broadfoot, A. L.: J. Quant. Spectrosc. Radiat. Transfer, 11, 1385 (1971).

83. O'Neil, R.; and Davidson, G.: AFCRL-67-0277, ASE-1602, American Science and Engineering, Inc., Cambridge, Mass., 1968.

84. Peterson, J. R.; and Moseley, J. T.: J. Chem. Phys., 58, 172 (1973).

85. Gray, D. D.: Roberts, T. D.; and Morack, J. L.: J. Chem. Phys., 57, 4190 (1972).

86. Zinchenko, G. N.: Sov. Phys.-Tech. Phys., 13, 937 (1969).

87. McDaniel, E. W.: Op. Cit., p. 244.

88. Benderson, B.; and Fite, W. L., eds.: Op. Cit., pp. 410-449.

89. Massey, H. S. W.; and Burhop, E. H. S.: Electronic and Ionic Impact Phenomena, pp. 478-480, Oxford at the Claredon Press, 1952.

90. Benderson, B.; and Fite, W. L., eds.: Opt. Cit., p. 417.

91. Massey, H. S. W.; and Burhop, E. H. S.: Opt. Cit., p. 479.

92. Mahadevan, P.; Magnuson, G. D.; Layton, J. K., and Carlston, C. E.: Phys. Rev., 140, A1407 (1965).

93. Weast, R. C., ed.: Handbook of Chemistry and Physics, 47th Ed., Chemical Rubber Publishing Company, Cleveland, Ohio, 1966.

94. Evans, R. D.: American Institute of Physics Handbook, pp. 8-90, McGraw Hill Book Company, Inc., New York, N.Y., 1963.

95. Kohl, W. H.: Handbook of Materials and Techniques for Vacuum Devices, pp. 142-145, Reinhold Publishing Corporation, New York, N.Y., 1967.

96. Kohl, W. H.: Op. Cit., pp. 181-183.

97. Field, F. H.; and Franklin, J. L.: Electron Impact Phenomena, pp. 26-37, Academic Press, New York, N.Y., 1970.

98. Gosh, S. N.; and Sheridan, W. F.: J. Chem. Phys., 26, 480 (1957).

99. Gustafsson, E.; and Lindholm, E.: Ark. Fysik., 18, 219 (1960).

100. Potter, R. F.: J. Chem. Phys., 22, 974 (1954).

101. Moran, T. F.; McCann, K. J.; and Flannery, M. R.: J. Chem. Phys., 3857 (1975).

102. Konopinski, E. J.: Classical Description of Motion, pp. 102-135, W. H. Freeman, and Company, San Francisco, California, 1968.

103. Eisberg, R. M.: Fundamentals of Modern Physics, pp. 518-524, John Wiley and Sons, Inc., New York, N.Y., 1961.

104. Marion, J. B.: Classical Dynamics, 2nd Ed., pp. 299-302, Academic Press, New York, N.Y., 1970.

105. Doverspike, L. D.; Champion, R. L.; and Baily, T. L.: J. Chem. Phys., 45, 4385 (1966).

106. Champion, R. L.; and Doverspike, L. D.: J. Chem. Phys., 49, 4321 (1968).

107. Bates, D. R.; and Reid, R. G. H.: Proc. Roy. Soc., A310, 1 (1969).

108. Bates, Dr. R.; and Lynn, N.: Proc. Phys. Soc., A253, 141 (1959).

109. Herzberg, G.: Molecular Spectra and Molecular Structure, D. Van Nostrand Company, Inc., Princeton, N.J., 1950.

110. Mason, E. A.; and Schamp, H. W., Jr.: Ann. Phys., 4, 233 (1958).

111. Mason, E. A.; and Vanderslice, J. T.: J. Chem. Phys., 31, 594 (1959).

112. Hirschfelder, J. O.; Curtis, C. F.; and Bird, R. B.: Op. Cit., pp. 950-1110.

113. Sato, S.: J. Chem. Phys., 23, 529 (1955).

114. Nicholls, R. W.: J. Res. Natl. Bur. Stand. (U.S.), A65, 451 (1961).

115. Moran, T. F.; and Friedman, L.: J. Chem. Phys., 42, 2391 (1965).

116. Lofthus, A.: "The Molecular Spectrum of Nitrogen," Spectroy. Rept. No. 2, Department of Physics, University of Oslo, Blinden, Norway, 1960.

117. Krupenie, P. H.; and Weissman, S.: J. Chem. Phys., 43, 1529 (1965).

118. Henrici, P.: Elements of Numerical Analysis, p. 280, John Wiley and Sons, Inc., New York, N.Y., 1964.

VIII: APPENDICES

A.1: KINEMATIC CONSIDERATIONS IN TWO-PARTICLE COLLISIONS

The description of a system of two particles is usually discussed using two different coordinate systems, the laboratory (Lab) and Center-of-Mass (C.M.). The Lab system is the frame of reference of a laboratory observer; the C.M. system moves with respect to the Lab system. Experimental measurements are made in the Lab system, but the mathematical calculations are simpler in the C.M. frame. Consider a description for a system of two particles as given in Figure A1-1. Since translational motion of the system is not important from the standpoint of the particle orbits with respect to one another, the origin is chosen for the system to be the C.M. where R is equal to zero. From the definition of center of mass, it is recalled that

$$\vec{R} = \frac{1}{M} \sum_i m_i \vec{r}_i \qquad \text{(A1-1)}$$

For a system of two particles this becomes

$$\vec{R} = \frac{1}{M} (m_1 \vec{r}_1 + m_2 \vec{r}_2) \qquad \text{A1-2)}$$

Differentiating equation (A1-2) with respect to time, we obtain

$$M\vec{V} = m_1 \vec{v}_1 + m_2 \vec{v}_2 \qquad \text{(A1-3)}$$

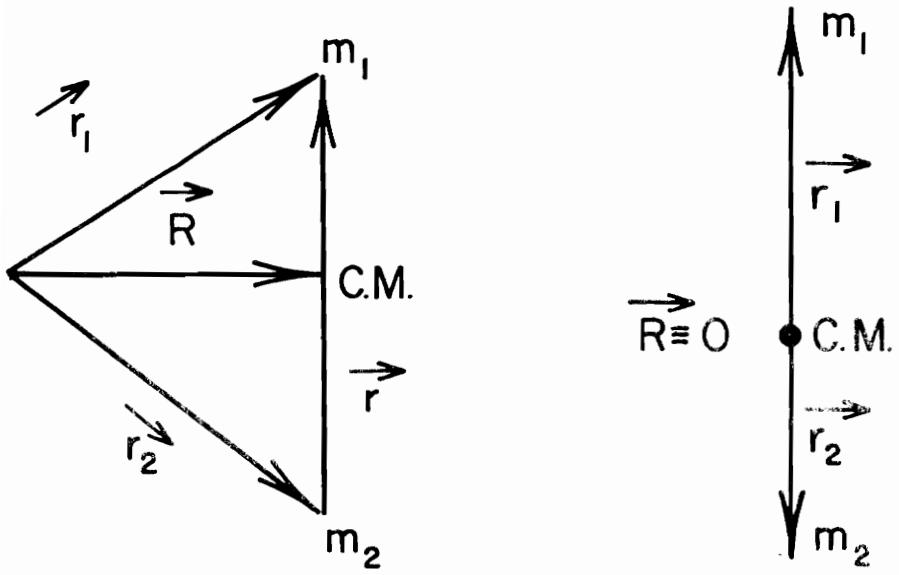

Figure A1-1.- Two Particle Center-of-Mass System.

where $M = m_1 + m_2$ and $\vec{V}$ is the velocity of the C.M. in the laboratory system.

In a charge transfer collision of interest in this research $v_2 \approx 0$, therefore

$$V = \frac{m_1 v_1}{m_1 + m_2} \tag{A1-4}$$

The C.M. velocities v_1' and v_2' are given as $v_1' = v_1 - V$, $v_2' = v_2 + V$, then;

$$v_1' = \frac{m_2 v_1}{m_1 + m_2} \tag{A1-5}$$

and

$$v_2' = \frac{m_1 v_1}{m_1 + m_2} \tag{A1-6}$$

We see that the C.M. for a collision of this type must be moving in the Lab system[102,103] toward m_2 with velocity of magnitude V (Figure A1-2). The velocity of the C.M. is constant in magnitude before, during, and after a collision, and the total linear momentum of the system in the C.M. frame is zero at all times. We see that before the collision the particles move directly toward each other and after colliding they move in exactly opposite directions (Figure A1-2). Charge transfer collisions are described by inelastic collisions in which the momentum is conserved but the total kinetic energy of the system decreases (or increase) as a result of excitation

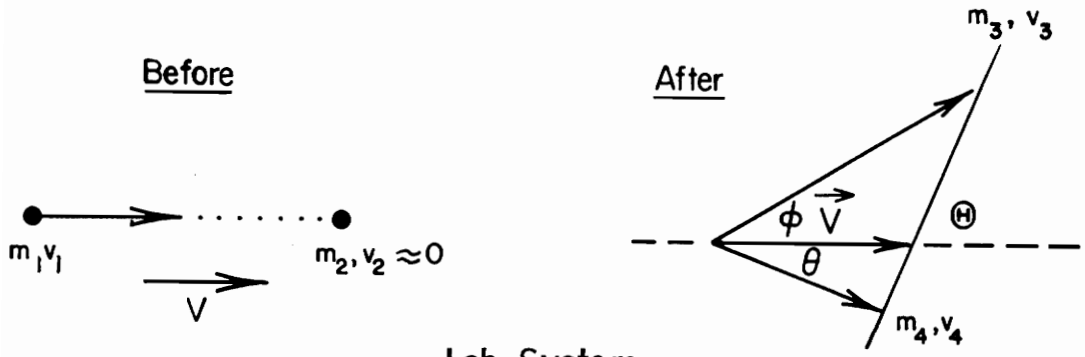

Lab System

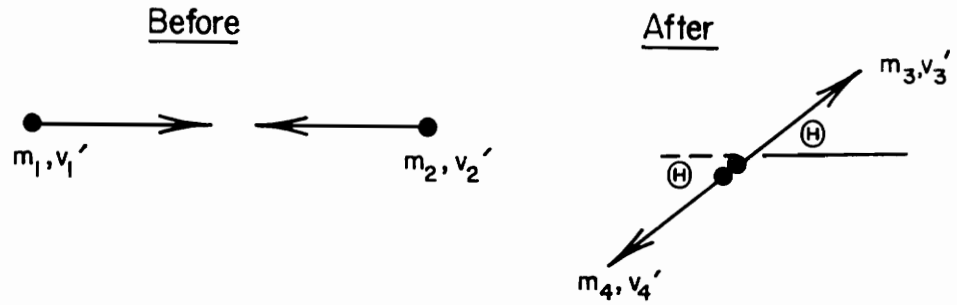

C.M. System

Figure A1-2.- Two Particle Collision System.

(or deexcitation) of one or both of the particles. Consider a general binary collision of the form

$$\underset{m_1,v_1}{A} + \underset{m_2,v_2}{B} \longrightarrow \underset{m_3,v_3}{C} + \underset{m_4,v_4}{D} \quad .$$

Several useful relationships among the energies and scattering angles may be derived. From the law of conservation of total energy we may write

$$T_C + U_C + T_D + U_D = T_A + U_A + T_B + U_B$$

where U and T are referred to as internal and kinetic energy of the colliding particle system. We define the energy defect for the system as

$$\Delta E \equiv (U_C + U_D) - (U_A + U_B)$$

$$\equiv (T_A + T_B) - (T_C + T_D)$$

If $\Delta E<0$ internal energy has been converted to kinetic energy in the collision process and the process is referred to as an exoergic reaction. If $\Delta E>0$ the opposite condition has occurred and the process is said to be endoergic.

From the definition of ΔE we find in the center-of-mass system;

$$\Delta E = \frac{m_1(v_1')^2}{2} + \frac{m_2(v_2')^2}{2} - \left(\frac{m_3(v_3')^2}{2} + \frac{m_4(v_4')^2}{2}\right) \qquad \text{(A1-7)}$$

Since the total linear momentum is equal to zero, it follows that $m_1 v_1' = m_2 v_2'$ and $m_3 v_3' = m_4 v_4'$, therefore

$$m_4 (v_4')^2 = m_3 (v_3') \left(\frac{m_3 v_3'}{m_4} \right)$$

$$= \frac{(m_3 v_3')^2}{m_4}$$

The relative kinetic energy of the collision process is defined as

$$E = \frac{m_1 (v_1')^2}{2} + \frac{m_2 (v_2')^2}{2} \qquad \text{and}$$

$$\Delta E = E - \left[\frac{1}{2} m_3 (v_3')^2 + \frac{1}{2} \frac{(m_3 v_3')^2}{m_4} \right]$$

or

$$E - \Delta E = \frac{1}{2} m_3 (v_3')^2 \left[\frac{m_3 + m_4}{m_4} \right] .$$

Using the relation $m_1 v_1' = m_2 v_2'$, the relative kinetic energy of the collision process can be written as

$$E = \frac{1}{2} m_1 (v_1')^2 \left(1 + \frac{m_1}{m_2} \right) .$$

Substituting the equations $v_1' = v_1 - V$ and $v_1 = \frac{V(m_1 + m_2)}{m_1}$ we find that

$$E = \frac{1}{2}\frac{m_2}{m_1}(m_1 + m_2)V^2 \ .$$

Then,
$$\frac{E - \Delta E}{E} = \frac{\frac{1}{2} m_3(v_3')^2\left(\frac{m_3 + m_4}{m_4}\right)}{\frac{1}{2} m_2/m_1 \ (m_1 + m_2)V^2} \ .$$

Since matter is conserved $m_1 + m_2 = m_3 + m_4$ and

$$\frac{E - \Delta E}{E} = \frac{m_1 m_3}{m_2 m_4}\left(\frac{v_3'}{V}\right)^2$$

A parameter γ is defined as $\gamma \equiv V/v_3'$ then

$$\frac{E - \Delta E}{E} = \frac{m_1 m_3}{m_2 m_4}\left(\frac{1}{\gamma}\right)^2 \qquad \text{(A1-8)}$$

In the laboratory system it is recalled from the conservation of momentum, Figure A1-2;

$$m_3 v_3 \sin \phi = m_4 v_4 \sin \theta$$

$$m_3 v_3 \cos \phi - m_1 v_1 = m_4 v_4 \cos \theta \ ,$$

Squaring these equations and adding we obtain:

$$E_4 = \frac{m_3}{m_4} E_3 + \frac{m_1 E_1}{m_4} - \frac{2}{m_4}(m_1 m_3 E_1 E_3)^{1/2} \cos \phi \qquad \text{(A1-9)}$$

Several important observations can be made by relating the scattering

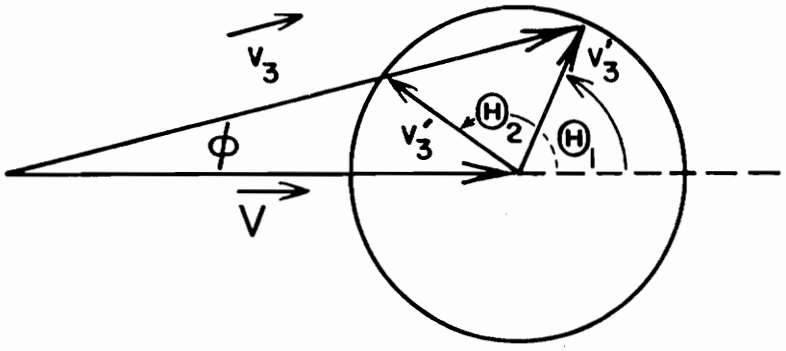

Figure A1-3.- Newton's Velocity Diagram.

angle of the observed particle C, in the Lab system, to the corresponding angle in the C.M. system. The transformation between ϕ and Θ of Figure A1-2 is obtained by the Newton diagram, as shown in Figure A1-3. From this figure we see that vector addition gives

$$\overrightarrow{v_3} = \vec{V} + \overrightarrow{v_3'}$$

for the observed particle C after the collision. It is required that the magnitude of velocity for the C particle be a constant if total energy is to be conserved. The trace of $\overrightarrow{v_3'}$ will then be a circle as shown in Figure A1-3. If $|\vec{V}| > |\overrightarrow{v_3'}|$ there are two values of the C.M. angle, Θ_1, and Θ_2 and two values of $\vec{v}_3$ for each laboratory observation angle ϕ. From geometrical consideration we may write the following equations:

$$v_3' \cos\Theta + V = v_3 \cos\phi \qquad \text{(A1-10)}$$

$$v_3' \sin\Theta = v_3 \sin\phi \qquad \text{(A1-11)}$$

and

$$\tan\phi = \frac{v_3' \sin\Theta}{v_3' \cos\Theta + V} \quad . \qquad \text{(A1-12)}$$

A parameter γ was defined as the ratio of C.M. velocity in the Lab frame to the velocity of the C particle in the C.M. system ($\gamma \equiv \frac{V}{v_3'}$). It follows that:

$$\tan \phi = \frac{\sin \Theta}{\gamma + \cos \Theta} \qquad \text{(A1-13)}$$

The parameter γ can now be calculated from equation (A1-8). From Figure A1-3 for $\gamma > 1$, v_3 and Θ are shown to be double-valued functions of the laboratory scattering angle ϕ. There also appears to be a maximum laboratory scattering angle ϕ_m (Figure A1-4). The maximum scattering angle is obtained from a geometric relation as

$$\sin \phi_m = \frac{v_3'}{V} = \frac{v_3'}{\gamma v_3'} = \frac{1}{\gamma} \quad .$$

Therefore;

$$\phi_m = \sin^{-1}\left(\frac{1}{\gamma}\right) \qquad \text{(A1-14)}$$

When $\gamma < 1$ the scattering phenomena is depicted as shown in Figure A1-5. For this case there is no maximum scattering angle; the range of ϕ is $0 < \phi < \pi$. The geometric relation between v_3 and Θ can now be seen to be a single valued function of the laboratory scattering angle ϕ. Finally, there are three very useful relations between ϕ and Θ for special values of the ratio V/v_3'. If $V \ll v_3'$; $\gamma \approx 0$, then $\phi \approx \Theta$ from equation (A1-12). The Lab and C.M. systems are almost identical for this case, ϕ increases monotonically from 0 to π as Θ increases from 0 to π. If $\gamma = 1$, ϕ varies from 0 to $\pi/2$ as ϕ varies from 0 to π. This implies that no particles are backscattered in the Lab system. Head-on scattering corresponds to $\Theta = \pi$, $\phi = \pi/2$, and $\theta = 0$. If

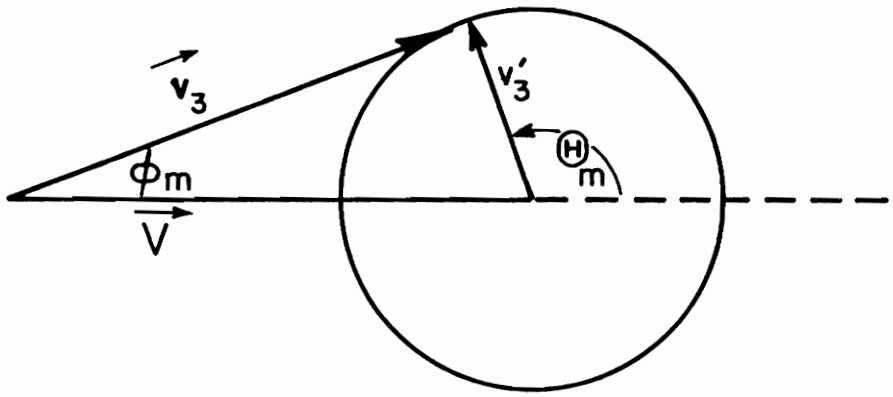

Figure A1-4.- Maximum Laboratory Scattering Angle.

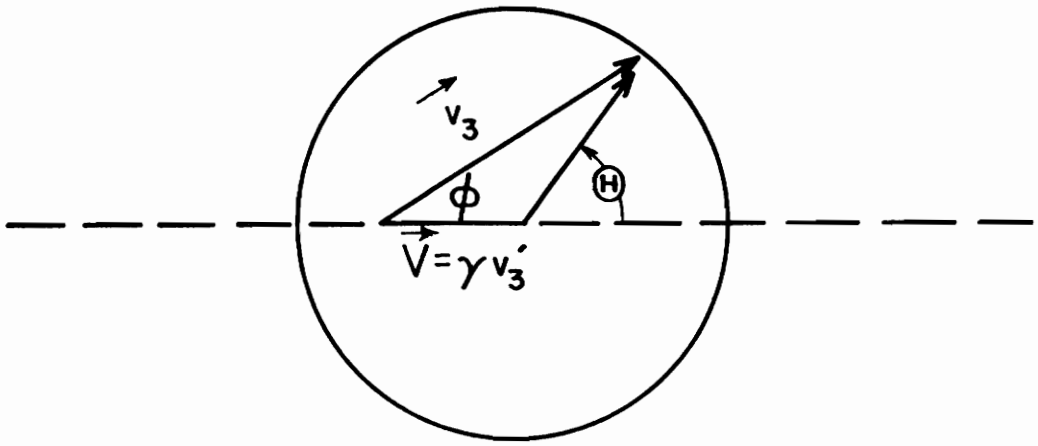

Figure A1-5.- Scattering Angles for $\gamma < 1$.

$V << v_3'$; $\gamma >> 1$ and $\phi \approx \frac{\sin\Theta}{\gamma}$; ϕ then increases from zero to a maximum value which is less than $\pi/2$.

In a typical charge transfer experiment $v_2 \approx 0$ (B is the target particle, which is essentially motionless in the Lab system). E_1 and E_3 can be measured as well as the laboratory observation angle ϕ for the C particle. E_4 can then be eliminated using equation (A1-9) and recalling that

$$\Delta E = E_3 + E_4 - (E_1 + E_2) \qquad \text{(A1-15)}$$

Substituting $E_2 \approx 0$, the final results obtained are

$$\Delta E = E_3\left(1 + \frac{m_3}{m_4}\right) - E_1\left(1 - \frac{m_1}{m_4}\right) - \frac{2}{m_4}(m_1 m_3 E_1 E_3)^{1/2} \cos\phi \qquad \text{(A1-16)}$$

where ϕ = detector observation angle

E_1 = kinetic energy of primary particle

E_3 = kinetic energy of product ion that is observed.

In nonreactive symmetric charge transfer reactions the masses of all particles are approximately the same. Any difference in mass will be due to the mass of an electron which is insignificant when compared with the remaining mass of the interacting particles. Therefore, equation (A1-16) reduces to

$$\Delta E = 2E_3 - 2(E_1 E_3)^{1/2} \cos\phi \qquad \text{(A1-17)}$$

From equation (A1-16) the following observation can be made. In a

general binary collision one can expect ΔE to have a multiplicity of values.[104] If experimental conditions assures that reactants A and B are in known internal states, the products may be in a number of excited states, leading to a number of ΔE values. When E_1 is fixed and if E_3 is measured at a given observation angle ϕ it is expected that a spectrum of E_3 values can be observed. Furthermore if symmetric charge transfer reactions are studied at an observation angle of 90 degrees from the incident beam, only endothermic reaction channels are observed as shown by equation (A1-16). This type of measurement is the basic technique used to study translational spectroscopy. In addition it can be used to infer information about excited states of products in reactive collisions and to learn about collision dynamics or mechanisms. Doverspike, Champion, and Bailey[105] have used equation (A1-16) to deduce the energy defect of the following reactions:

$$A_r^+ + D_2 \longrightarrow A_rD^+ + D$$

$$N_2^+ + D_2 \longrightarrow N_2D^+ + D$$

The energy defects observed by these investigators were positive in each case and the reactions would necessarily be endothermic. Also, Champion and Doverspike[106] used the resulting equation to study energy defects for the charge transfer reactions of the rare gas ions with molecular nitrogen. In this study exothermic processes were observed only for singly charged helium ions with molecular

nitrogen. The kinetic energies of the product ions were studied at angles in the range $0^{o} \leq \phi \leq 60^{o}$. From equation (A1-16) it can be seen that at these angles the energy defect is a complicated function of both the primary and product ions kinetic energies.

A.2: THEORY OF CHARGE EXCHANGE

Comparatively little detailed, theoretical work has been done on the collision of a molecular ion with its neutral parent. The treatment is more complicated than the atomic case because vibrational excitation may result from the nuclear potential energy changes which occur with charge transfer. Bates and Reid [107] formulated and applied a theoretical treatment of molecular charge transfer in which specific account is taken of the important coupling not acknowledged by the usual two-state treatment of Gurnee and Magee. [16] The most recent treatment of molecular charge transfer is given by the full multistate impact parameter treatment of Flannery, Cosby, and Moran. [12]

In the theoretical studies of charge transfer, as in theoretical studies of other types of collision between atomic systems, there are two main approximations: a high velocity approximation in which the pertubation causing transition is taken to be the interaction potential and a low velocity approximation in which the pertubation is taken to be the relative motion. Since the present work was accomplished in the low velocity range, the pertubation was taken to be the relative velocity. The present discussion will outline the multistate impact parameter treatment of reference 12. This method attempts to take into account the vibrational states of the incident ions and of the products, while the target neutral molecules are assumed to be in the ground state.

When the charge-transfer process for diatomic nitrogen is resonant and symmetric, the wave function $\Psi(t)$ for internal motion may be expanded in terms of the gerade and ungerade eigenfunctions $\chi_{g,u}(\vec{r}, \vec{R})$ for each electronic state of the quasimolecular complex formed. The atomic separation in the molecule is $\vec{r}$ and the distance between the two centers of mass is $\vec{R}$. The relative phase η changes with $\vec{R}$ because of differences in eigenenergies $E_{g,u}(\vec{R})$. Bates and Lynn [108] point out that charge transfer does not occur because of an electronic transition but because of a phase change. The impact parameter model was used to calculate the charge-transfer cross sections shown in Figure A2-1. In this model, the initial state of the molecule is at the point a, located at a distance $\vec{\rho}$ from the X axis, and the ion is at the point b, which is located at $Z = -\infty$. The point b moves along the X axis with the constant velocity $\vec{v}$. In the final state the ion is at point a and the molecule at the point b, where b is now located at $Z = +\infty$. A straight line trajectory is assumed where $\vec{\rho}$ is the impact parameter and v is the incident speed along the Z-axis, and $\vec{R} = \vec{\rho} + \vec{v}t$. The probability for symmetrical resonance charge transfer as determined from a two-state (g,u) molecule M treatment (in which the coupled equation can be solved exactly) is given as: [107]

$$P_M^+(\rho) = \sin^2\eta(\rho) \qquad \text{(A2-1)}$$

where

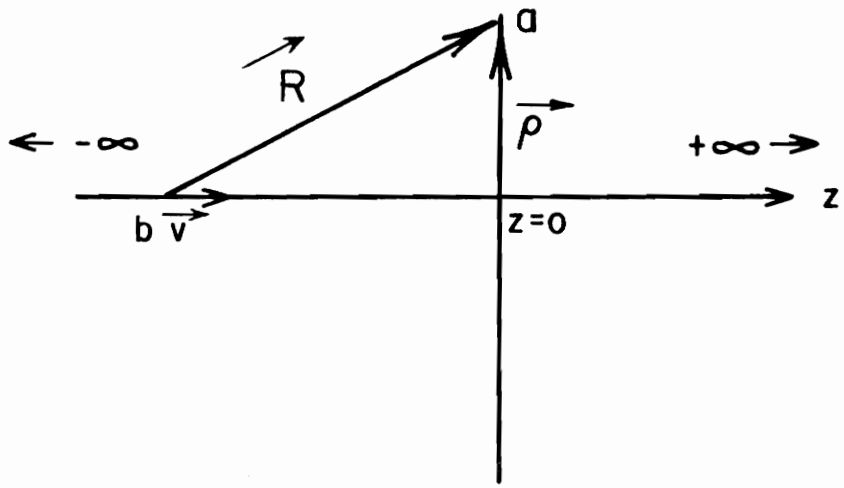

Figure A2-1.- Impact Parameter Collision Model.

$$\eta(\rho) = \frac{1}{\hbar v}\int_{o}^{+\infty} \left[\varepsilon_g(R) - \varepsilon_u(R)\right]dZ \qquad \text{(A2-2)}$$

The charge-transfer cross section is then given as

$$\sigma = 2\pi \int_{o}^{+\infty} \rho \sin^2\eta(\rho)d\rho \qquad \text{(A2-3)}$$

In order to include nonresonant channels, the wave function is expanded [107] in terms of $\phi_n^\alpha(\vec{r})$, the molecular eigenfunctions of the unperturbed Hamiltonian for the isolated molecular system. The $\phi_n^\alpha(\vec{r})$ have electronic vibrational and rotational parts. The eigenenergies at infinite center-of-mass separation are E_n^α, and

$$\Psi(t) = \sum_{\alpha=D,X} \sum_{n} a_n^\alpha \phi_n^\alpha(\vec{r}) \exp(-iE_n^\alpha t/\hbar) \qquad \text{(A2-4)}$$

The index α refers to either the direct D (no charge transfer) or to the exchange channels X. Bates and Reid [107] used the expanded form of equation (A2-4) and substituted it into the time-dependent Schrodinger equation for internal coordinates and derived the following relation for charge-transfer cross section:

$$\sigma = 2\pi \int_{o}^{+\infty} \left|C_f^X(\rho,\infty)\right|^2 \rho d\rho \qquad \text{(A2-5)}$$

The transition amplitude $C_f^X(\rho,t)$ are the solutions to the set of

first order coupled differential equations

$$i\frac{\partial C_{\ell}^{\alpha}}{\partial t} = V(R)\sum_{m=1}^{N} P_{\ell m} C_{m}^{\bar{\alpha}}(\rho,t)\exp i(E_{\ell} - E_{m})t/\hbar,\quad \ell = 1, 2, \cdots N \qquad (A2\text{-}6)$$

where $\bar{\alpha} = X$ when $\alpha = D$ and vise versa. Only the direct channel i is occupied initially, therefore:

$$C_{m}^{D}(\rho,-\infty) = \delta_{mi}$$
$$C_{m}^{X}(\rho,-\infty) = 0 \qquad (A2\text{-}7)$$

The matrix elements $P_{\ell m}$ are

$$P_{\ell m} = F(\upsilon_{\ell}', \upsilon_{m}'')\, F(\upsilon_{m}', \upsilon_{\ell}'') \qquad (A2\text{-}8)$$

where $F(\upsilon_{i}' \upsilon_{n}'')$ is the vibrational overlap of the incident ion in the υ_{i}' vibrational state and the target neutral in the υ_{n}'' vibrational state. The rotational motion is neglected since the rotational times are much greater than the collision times.[12] The interaction potential is assumed to be spherically symmetric and can be obtained from the gerade-ungerade splitting of the vibrational motion[12] as

$$V(R) = \frac{1}{2}\left[\varepsilon_{g}(R) - \varepsilon_{u}(R)\right] \qquad (A2\text{-}9)$$

Then the exchange cross section becomes

$$\sigma = 2\pi \int_0^{+\infty} \rho \sin^2 \left[\frac{2}{\hbar V} \int_0^{+\infty} V(R)\, dZ \right] \qquad \text{(A2-10)}$$

The gerade potential is given by the Morse function[109] as

$$\varepsilon_g(R) = D_e\left[\exp(-2\beta(R - R_e)) - 2\exp(-\beta(R - R_e))\right] \qquad \text{(A2-11)}$$

where R_e is the internuclear distance corresponding to the potential minimum of depth D_e, and β describes the shape of the potential. The modified Lennard-Jones potential,[110,111]

$$V_{LJ4} = 4\varepsilon\left[\left(\frac{d}{R}\right)^{12} - \left(\frac{d}{R}\right)^{6} - \frac{\alpha e^2}{2R^4}\right] \qquad \text{(A2-12)}$$

where α is the polarizability and ε and d are Lennard-Jones parameters which are known for the nitrogen potential,[112] gives the interaction energy for the gerade state for this reaction. Fitting the Morse curve to the modified Lennard-Jones potential allows determination of the parameter $R_e = 3.5262 \times 10^{-8}$ cm, $D_e = 0.06917$ eV and $\beta = 1.5903 \times 10^{-8}$ cm^{-11} for nitrogen.[12]

Sato[113] proposed that the ungerade potential may be written as

$$\varepsilon_u(R) = \tfrac{1}{2}D_e\left[\exp(-2\beta(R - R_e)) + 2\exp(-\beta(R - R_e))\right] \qquad \text{(A2-13)}$$

The interaction potential V(R) for equation (A2-9) is therefore found to be

$$V(R) = \begin{cases} \frac{1}{4}D_e \exp(-2\beta(R - R_e)) - \frac{3}{2}D_e \exp(-\beta(R - R_e)) & R > R^* \\ 0 & R < R^* \end{cases} \qquad \text{(A2-14)}$$

$V(R)$ is set equal to zero for small $R < R^*$, where $R^* \equiv R_e - \ell n\ 6/\beta$ for N_4^+, since negative values of the interaction potential are unphysical. Since D_e, R_e, and β have been determined, the interaction potential is not known.

Vibrational overlaps are needed in order to obtain the transition amplitude C_f^x for the charge-transfer cross section in equation (A2-5). Overlaps for diatomic ions and neutral molecules in the ground state are given by Nicholls.[114] Flannery et.al.[12] computed overlaps for excited states of the neutral using Frank-Condon factors[114] with a Morse anharmonic oscillator wavefunction.[114,115] The excitation defects of various reaction channels were computed from spectroscopic energy levels[109,116,117] of the ionic and neutral species. They found[12] that the excitation defects occurred in groups or "bands" separated by approximately one vibrational quantum of energy, about 0.25 eV.[73] Therefore the channels could be considered to be degenerate within a given band, greatly simplifying the calculations involved. The transition probabilities $P_{\ell m} = |C_f^x|^2$ were obtained as a function of impact parameter ρ by solving the multistate equation (A2-6) numerically by the Adams-Moulton method.[118] The charge transfer cross sections σ were obtained from equation (A2-5)

using these transition probabilities by numerical integration over impact parameter using Simpson's rule with a built-in accuracy parameter.

The low velocity approximation [107] can be used for collisions in which the incident velocity is small enough so that the excitation defect $E_\ell - E_m$ is approximately zero. Then equation (A2-6) for the transition probability becomes

$$\frac{i\partial C_\ell^\alpha}{\partial t} = V(R) \sum_{m=1}^{B} P_{\ell m} \bar{C}_m^\alpha(\rho,t), \quad \ell = 1,2,3\cdots B \tag{A2-15}$$

where B is the number of degenerate final states which have zero energy defect with the incident energies. The exchange cross section then becomes

$$\sigma = 2\pi \sum_{n=1}^{B} X_{in} \int_0^{+\infty} \rho \sin^2 \left[\frac{\pi_n}{\hbar v} \int_{-\infty}^{+\infty} V(R)\, dZ \right] d\rho \tag{A2-16}$$

where the π_n are the eigenvalues and X_{in} the associated eigenfunctions of the matrix which diagonalizes the matrix P formed from the $P_{\ell m}$; that is

$$\pi = X^{-1} PX = X\, PX \tag{A2-17}$$

A.3: IMPORTANT MATERIALS AND SOURCES OF SUPPLY

Item	Use	Supplier
Ceramic Parts (Al_2O_3 Lock Rings)	Mounting Ion Optic Elements	Kimball Physics, Inc. Milton, New Hampshire
Screen Wire Mesh	Charge Transfer Cell Screen and Ion Optics	Unique Wire & Weaving Company, Inc. Hillside, New Jersey
POCO Graphite	Beam Flag Two (BF2)	POCO Graphite, Inc. Decatur, Texas
Bellows	Feedthru for BF1 and BF2	Metal Bellows Company Sharon, Massachusetts
Ceramic Beads	Feedthru Insulation for All Wire Leads to Optical Elements CTC and CTCS	Minnesota Mining and Manufacturing Company Chattanooga, Tennessee
Ceramic-to-Metal Seals	Gas Inlet Support for CTC Feedthru. Connections for Optical Elements, BF1 and BF2	Ceramaseal, Inc. New Lebanon Center, New York
Coaxial Glass-Metal Seals	Feedthru Connection for Current Measurement to CTC and CTCS	Greenfield Components, Corp. Greenfield, Massachusetts
Teflon	Mounting Lens Two Section. Support for T_2 and T_3	Instrument Development Shop NASA Langley
Nylon Screws	Mounting, R/D, FD_3 and FD_4. Holding Lens Two Section Together	Mil-Spec Fastener Corp. Hampstead, Maryland
OFHC Copper	CTC Apertures	Utility Brass & Copper Co. Moonachie, New Jersey
Synthetic Sapphire Balls	Insulations Between CTC and CTCS. Ion Source	Pageant Miller Industry Chinchilla, Pennsylvania
Copper Wire	Lead Wire for Optical Elements, CTC and CTCS	Utility Brass & Copper Co. Moonachie, New Jersey

Item	Use	Supplier
Torr Seal	CTC at Gas Inlet Port and Feedthru for CTCS. Flange Header on Vacuum Wall for Connecting CTC and CTCS to Coaxial Feedthrus	Varian Associates Palo Alto, California

A.4: ERROR ANALYSIS

Several parameter measurements are required to utilize the charge transfer equation given in section V.B. as:

$$\sigma = - \frac{kT}{P_{CTC} x} \ell n(1 - I_{CT}/I(o)) \qquad A4\text{-}1)$$

In order to get the effect of uncertainty in all parameters, sutsti-tution must be made in equation (A4-1). For example, P_{CTC} is obtained by the procedure described in section IV.H. as:

$$P_{CTC} = \frac{P_{pp} \; C_{pp}}{C_{CTC}} \qquad (A4\text{-}2)$$

C_{pp} was obtained in a manner described in section IV.D. where:

$$C_{pp} = \frac{V}{t} \ell n \; P_i/P_t \qquad (A4\text{-}3)$$

C_{CTC} is calculable from the following relation:

$$C_{CTC} = \frac{\pi}{4} \bar{v}(R_1^2 + R_2^2) \qquad (A4\text{-}4)$$

where $\bar{v}$ is the test gas molecular speed given by the Maxwell-Boltzmann distribution law for an equilibrium gas at temperature T. R_1 and R_2 are the radii of the inlet and exit apertures of CTC. The molecular speed $\bar{v}$ is known to be given as:

$$\bar{v} = \left(\frac{8kT}{\pi m}\right)^{1/2} \qquad \text{(A4-5)}$$

where k = Boltzmann's constant (ergs/^{o}Kelvin)

T = absolute temperature (^{o}Kelvin)

m = mass per molecule (grams/molecule)

π = 3.1416

To determine the magnitude of the probable errors involved in the charge transfer calculations, it was necessary to evaluate the effects of uncertainties in each parameter measurement. This was done by choosing typical operating parameters and representative error data specifications for instruments and machined parts. Numerical values of the following parameters are needed for a charge transfer measurement.

(1) T - temperature of CTC

(2) R_1 - radius of CTC inlet aperture

(3) R_2 - radius of CTC exit aperture

(4) t - time of porous plug conductance measurement

(5) V - volume of test apparatus used for porous plug conductance measurement

(6) X - length of CTC

(7) P_{pp} - pressure at porous plug during charge-transfer measurements

(8) P_i - initial pressure at porous plug during conductance calibration

(9) P_t - final pressure at porous plug after conductance calibration time (t)

(10) I_{CT} - slow ion current to CTCS

(11) I(o) - total primary ion current into CTC

When equations (A4-2) through (A4-5) are substituted into equation (A4-1) the following equation is obtained:

$$\sigma = -\left[\left(\frac{\pi}{2m}\right)^{1/3} k\right]^{3/2} \frac{T^{3/2}(R_1^2 + R_2^2)t}{X\ P_{pp}\ V} \frac{\ell n(1 - I_{CT}/I(o))}{\ell n\ P_i/P_t} \qquad (A4\text{-}6)$$

Calculations of the fractional errors in a measurement are obtained by knowing the uncertainty in individual parameters. The fractional error in σ is:

$$\frac{\Delta\sigma}{\sigma} = \left\{ \sum_{j=1} \left[\frac{1}{\sigma} \frac{\partial\sigma}{\partial x_j} \Delta x_j\right]^2 \right\}^{1/2} \qquad (A4\text{-}7)$$

where Δx_j is a measurement uncertainty in the x_j parameter. The values of m, π, and k are considered to be known with sufficient accuracy so that they are essentially constant for this treatment. Each partial differential factor and the measurement uncertainty for all parameters are listed in Table A4-1. The values used for measurement uncertainty represent typical measurement errors. Using the results in Table A4-1 equation (A4-7) becomes:

$$\frac{\Delta\sigma}{\sigma} = \left[\left(\frac{3\Delta T}{2T}\right)^2 + \left(\frac{2\Delta R_1}{R_1}\right)^2 + \left(\frac{2\Delta R_2}{R_2}\right)^2 + \left(\frac{\Delta t}{t}\right)^2 + \left(\frac{\Delta V}{V}\right)^2 + \left(\frac{\Delta x}{x}\right)^2 + \left(\frac{\Delta P_{pp}}{P_{pp}}\right)^2 + \right.$$

$$\left(\frac{\Delta P_i}{P_i \ell n P_i/P_t}\right)^2 + \left(\frac{\Delta P_t}{P_t \ell n P_i/P_t}\right)^2 +$$

$$\left(\frac{\Delta I_{CT}}{I(o)(1 - I_{CT}/I(o))\ell n(1 - I_{CT}/I(o))}\right)^2 +$$

$$\left(\frac{I_{CT}\ \Delta I(o)}{I^2(o)(1 - I_{CT}/I(o))\ell n(1 - I_{CT}/I(o))}\right)^2\Bigg]^{1/2} \qquad \text{(A4-8)}$$

Substituting for each parameter and measurement uncertainty, the fractional error in σ is found to be 5.7 percent. There is an additional error that is not exhibited in equation (A4-8). This error enters in the current collection process as described in Section V.B. When $\Delta\phi = 0$, the current measured at CTCS is given by the following relation: $I_{CTCS} = 0.11\ I_{slow} + 0.43\ I(o)$. When $\Delta\phi = 12$ volts the current measured at CTCS is given by a different relation: $I_{CTCS} = I_{slow} + 0.43\ I(o)$. Therefore $\frac{I_{CT}}{I(o)}$ was defined such that,

$$\frac{I_{CT}}{I(o)} = \frac{I_{CTCS}}{I(o)}\bigg|_{\infty} - \frac{I_{CTCS}}{I(o)}\bigg|_{o}.$$

It follows that

$$I_{CT} = (I_{slow} + 0.43\ I(o)) - (0.11\ I_{slow} + 0.43\ I(o))$$

$$= 0.89\ I_{slow}.$$

TABLE A4-1. Measurement Uncertainty Data

Parameter (x_j)	Differential Factor $\left(\frac{1}{\sigma}\frac{\partial\sigma}{\partial x_j}\right)$	Measurement Uncertainty (Δx_j)
T = 295 K	3/2T	2 K
R_1 = 0.119 cm	$2/R_1$	0.0015 cm
R_2 = 0.159 cm	$2/R_2$	0.0015 cm
t = 1.26 x 10^4 sec	1/t	5 sec
V = 241 cm^3	-1/V	2 cm^3
X = 5.08 cm	-1/X	0.18 cm

TABLE A4-1. Continued

Parameter (x_j)	Differential Factor $\left(\frac{1}{\sigma}\frac{\partial\sigma}{\partial x_j}\right)$	Measurement Uncertainty (Δx_j)
P_{pp} = 30 torr	$-1/P_{pp}$	0.02 torr
P_i = 100 torr	$-\frac{1}{P_i \ \ell n \ P_i/P_t}$	0.06 torr
P_t = 60 torr	$\frac{1}{P_t \ \ell n \ P_i/P_t}$	0.036 torr
$I_{CT} = 1.5 \times 10^{-10}$ amps	$\frac{-1}{I(0)(1 - I_{CT}/I(0))\ell n(1 - I_{CT}/I(0))}$	3×10^{-12} amps
$I(0) = 17.3 \times 10^{-10}$ amps	$\frac{I_{CT}}{I(0)^2(1 - I_{CT}/I(0))\ell n(1 - I_{CT}/I(0))}$	3.46×10^{-11} amps

We see that the actual measured value of the slow ion current is 89 percent of the true value of slow ion current. When this error is considered in the cross section equation, we find that $\frac{\sigma_T - \sigma_M}{\sigma T} = 8.5$ percent. σ_T is considered to be the true value and σ_M the measured value. Adding this error due to current collection to the systematic errors given by equation (A4-8) the total fractional error is found to be in the range $-0.142 < \frac{\Delta\sigma}{\sigma} < 0.05$.

VITA

Alphonsa Smith was born to Ellis and Mary Smith on January 23, 1937, in Wetumpka, Alabama. He attended primary and secondary schools in the city of his birth and was graduated from Elmore County High School in May of 1955. Honorably served his country in the U. S. Air Force from June 1955 to June 1958. Enrolled in Tuskegee Institute Department of Electrical Engineering in the fall of 1958 and graduated in May of 1962 with a Bachelor of Science Degree in Electrical Engineering. After graduating from Tuskegee Institute, the author accepted a research position with the National Aeronautics and Space Administration at Langley Research Center. While at Langley, he has performed research in a variety of areas related to instrumentation development and evaluation with applications to environmental measurement. During this time, he received a Master of Science Degree in Physics from the College of William and Mary, in May of 1970. In 1972, he enrolled in the doctorate interdisciplinary program in Materials Engineering Science at Virginia Polytechnic Institute and State University, and since that time has been performing research related to this dissertation.

STUDIES OF CHARGE TRANSFER IN THE $N_2^+ - N_2$ SYSTEM

By

Alphonsa Smith

(ABSTRACT)

Total charge-transfer cross sections have been obtained in the $N_2^+ - N_2$ system with relative ion energies at seven different values between 9 and 441 eV. Data is obtained to examine the curvature and structural relation between total cross section versus ion energy.

The effect of ion beam excitation on the cross sections was studied by varying the electron ionization energy in the mass spectrometer ion source over electron energies at eight different values, between 11.6 and 32.1 eV.

The dependence of total cross section on the neutralization chamber gas pressure was examined by obtaining data at four different pressure values from 9.9 to 19.9 x 10^{-5} torr.

Subsequent data treatment provided 56 different cross section values that are compared with experimental and theoretical results of other investigators.